DIGITAL IMPULSE RADAR FOR GLACIOLOGY: INSTRUMENTATION, MODELLING, AND FIELD STUDIES

by

FRANCIS HUGH MELVILL JONES

B.Eng.(Electrical), McGill University, 1981

A THESIS SUBMITTED IN PARTIAL FULFILLMENT OF

THE REQUIREMENTS FOR THE DEGREE OF

MASTER OF SCIENCE

in

THE FACULTY OF GRADUATE STUDIES

Department of Geophysics and Astronomy

We accept this thesis as conforming

to the required standard

THE UNIVERSITY OF BRITISH COLUMBIA

November 1987

In presenting this thesis in partial fulfilment of the requirements for an advanced degree at the University of British Columbia, I agree that the Library shall make it freely available for reference and study. I further agree that permission for extensive copying of this thesis for scholarly purposes may be granted by the head of my department or by his or her representatives. It is understood that copying or publication of this thesis for financial gain shall not be allowed without my written permission.

Department of GEOPHYSICS & ASTRONOMY

The University of British Columbia
1956 Main Mall
Vancouver, Canada
V6T 1Y3

Date JUNE 20 1987

ABSTRACT

Several aspects of impulse radar echo sounding of small glaciers are investigated. First, the ranges of values expected for conductivity and relative dielectric permittivity of glacier ice, glacier bed materials and mixtures of ice and rock are established. These parameters, and the fundamentals of electromagnetic wave propagation, are employed in a modelling scheme that examines the reflection of pulses from planar reflectors within the glacier. The glacier bed can be modelled as solid rock or unconsolidated debris and as either frozen or wet. A layer of mixed ice and rock between the glacier ice and bed can also be included. Signal enhancement, especially using multi-channel principal component analysis, is discussed.

Discussion of practical application of the technique begins with the description of a portable microprocessor-controlled instrument capable of recording digitized echograms. Then results from experiments on Trapridge Glacier, Yukon Territory are presented. Surveys up to half a kilometer long with soundings at 1 to 20 m intervals were conducted. Bed topography is presented and locally anomalous sections are examined. Smaller-scale parameters such as the attenuation constant of ice and reflector properties are also extracted from the data. Subglacial and englacial temporal variations were studied by automatically recording echoes at one location every 20 minutes over a three-day period. Such experiments are to be used in the future in conjunction with other, concurrent, geophysical and hydrological investigations.

TABLE OF CONTENTS

LIST OF TABLES

LIST OF FIGURES

ACKNOWLEDGEMENTS

The successful completion of this project would not have been possible without the guidance and encouragement of my supervisor, Dr. G.K.C. Clarke, and the enthusiastic support and advice from Dr. B.B. Narod. My thanks also to M.J. Yedlin for providing insight into diffraction processes. Valuable field assistance from Guy Cross, Patricia Birch, and Andrew Lawrence was much appreciated, and Erik Blake provided the surveying information. I also thank Patricia Birch for proofreading final drafts of this thesis. Thanks are due to the superintendents and staff of Kluane National Park, Jasper National Park and Garibaldi Provincial Park for permission to work in their parks. This work has been supported by grants from the Natural Sciences and Engineering Research Council of Canada and Northern Scientific Training Grants from the Department of Indian and Northern Affairs.

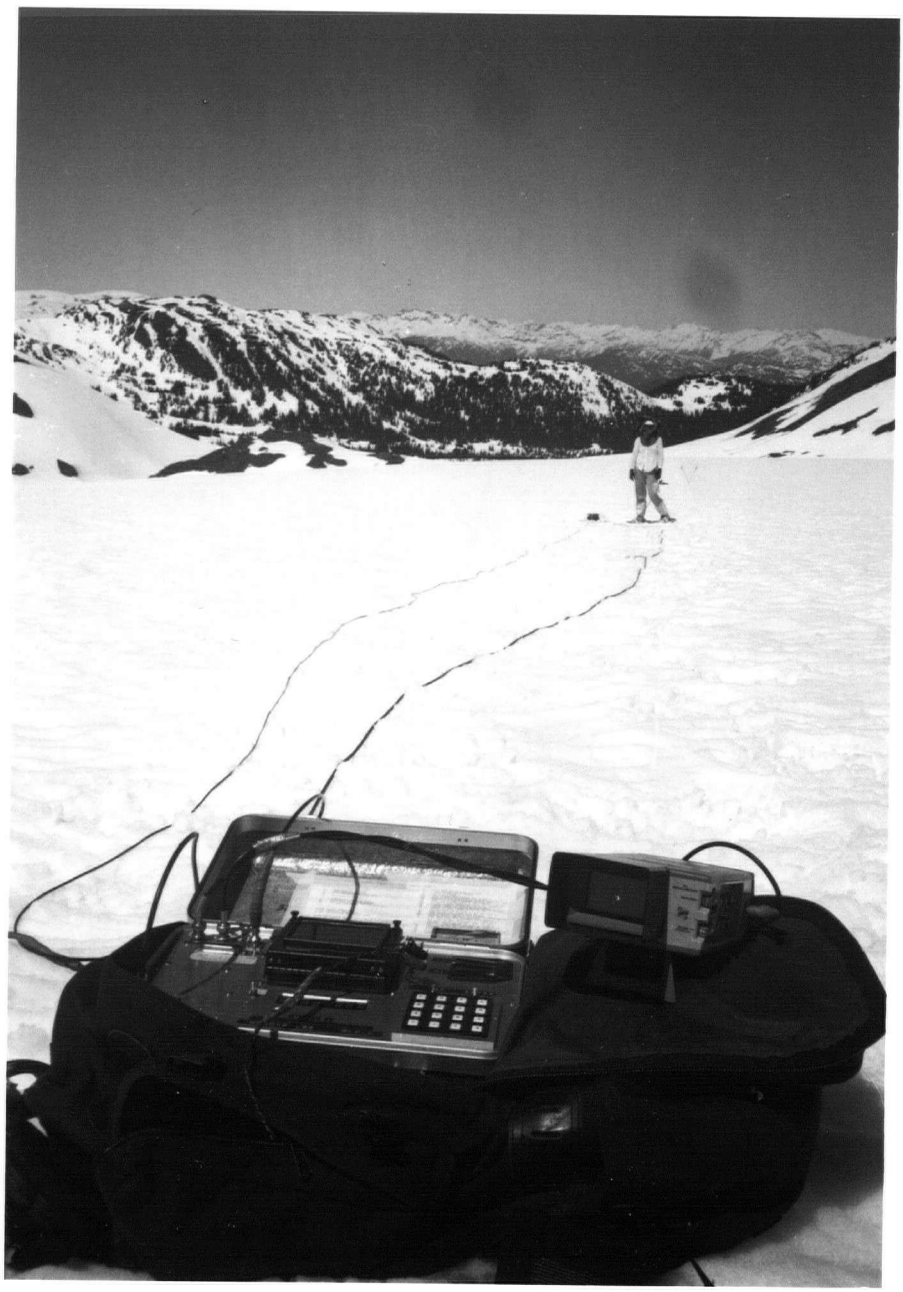

FRONTISPIECE: Operating the UBC portable digital impulse radar echo-sounding equipment on Helm Glacier, Garibaldi Provincial Park, May, 1986.

CHAPTER I

INTRODUCTION

Radio echo sounding has been established for many years as a useful technique for studying polar ice sheets (Bogorodsky and others, 1986), but application of similar methods to the investigation of small mountain glaciers has had mixed success. Various problems have contributed to this lack of consistency. The attenuation of electromagnetic energy at frequencies commonly used (over 30 MHz) was often too high to permit usable bottom echoes to be recorded. Also, resolution higher than that obtained in polar work is often required, navigation needs are more stringent, and logistical difficulties of working in mountain environments often preclude the use of large amounts of highly technical equipment.

Smith and Evans (1972) examined absorption and scattering of electromagnetic energy by ice and water inclusions, and Watts and England (1976) extended the theory to show that frequencies below 5 MHz would likely be required if reliable results were to be expected on temperate glaciers. They suggested the use of very short pulses to avoid the loss of resolution that would otherwise occur at such low frequencies. The resulting echograms would appear similar to seismic records, in which the travel times of echoes could be measured at specific points on the wavelet, rather than having to wait for several cycles of energy to arrive before recording a usable signal.

Impulse radar of this type was first used for ground probing (Cook, 1974) and in permafrost studies (Annan and Davis, 1976). Interest is still strong in these areas, and instruments working at frequencies in the UHF and VHF ranges are being used in civil engineering applications (Ulriksen, 1982) and in permafrost (Arcone and Delaney, 1984)

and sea ice studies (Fagan, 1987). Glaciological applications were first proposed by Cook (1960), and had become commonplace by the late 1970s (Sverrisson and others, 1980; Watts and Wright, 1981). At present, the method is most often used to make spot measurements of glacier depth. Application of modern digital techniques has been slow, perhaps because of the size and power requirements of high-speed digitizing oscilloscopes and other equipment. Though some groups are carrying out sophisticated experiments (Jacobel and Raymond, 1984; Walford and others, 1986), there is certainly room for improvement in this area of glaciology.

The project discussed in this thesis was begun in 1980 by B.B. Narod and G.K.C. Clarke, who designed a portable, microprocessor-controlled, digitizing instrument. The goal was to build a lightweight, self-contained instrument that stored echograms in digital form, and that would be capable of automatically gathering records at pre-set intervals for the purpose of studying changes in glacier dynamics over a period of time. The instrument was completed as part of this project, although the design now lags behind state-of-the-art technology by a few years. Potential improvements will become apparent in the course of this report.

Digital recordings are useful in facilitating the application of seismic data processing techniques. One such method, digital forward modelling, was used to assess how much detail concerning glacier bed properties might be revealed in field data. These theoretical experiments prompted the use of multi-channel principal component analysis to aid in separating gross echo features from more subtle characteristics.

Field testing of the instrument went through a series of phases culminating in the acquisition of a variety of data sets from Trapridge Glacier, Yukon Territory. Results can be analyzed most successfully if a reference signal from some known reflector can be simultaneously recorded. Signals that have propagated as surface waves along the ice/air interface do not make useful references because this type of propagation is complicated

and poorly understood. In this study, the use of echoes from a crevasse in the vicinity of the instrument, as well as the use of multiple reflections, allowed estimates to be made of the glacier bed's reflectivity. A similar analysis showed that apparent temporal variations in basal reflectivity over a three-day period were in fact not due to changes at the glacier bed.

In this thesis, I consider these aspects of impulse radar echo sounding as follows. Electrical properties and the propagation of electromagnetic pulses in glaciers are first discussed theoretically. These results are then applied in digital modelling exeriments that investigate how reflection from realistic glacier beds affects short electromagnetic pulses. Some digital processing techniques for emphasizing different aspects of the echograms are also presented. Then the instrument is described in some detail to explain how the records are generated. Field methods are then discussed, followed by the analysis of data obtained in July, 1986. Finally, I summarize the project and present some ideas for improvements and future experiments that were suggested in the course of the study.

CHAPTER II

ELECTROMAGNETIC PULSE PROPAGATION IN GLACIERS

2.1 INTRODUCTION

Many basic texts on electromagnetic waves discuss propagation in dielectric media (*e.g.* Jordan and Balmain, 1968) and there is now extensive coverage of monochromatic radio echo sounding theory in the glaciological literature (*e.g.* Bogorodsky and others, 1986; Robin and others, 1969). When discussing wideband signals, much of this theory must be applied cautiously, because scattering, attenuation and reflection can be frequency dependent. Some attention has been paid to these issues in the engineering, glaciology and permafrost literature but, in general, interpretation of impulse radar work has been qualitative. (Exceptions include Jacobel and Raymond (1984); Walford and others (1986); Arcone and Delaney (1982); Morey and Kovacs (1985).) Subsequent chapters of this thesis will attempt to be more rigorous in the consideration of current work on Trapridge Glacier and this chapter will discuss the prerequisite theory.

2.2 ELECTRICAL PARAMETERS OF GLACIER MATERIALS

Before introducing the equations describing electromagnetic pulse propagation in glaciers, the electrical properties of relevant materials must be considered. All these materials are non-magnetic, so the magnetic permeability μ will be taken as that of free space; *i.e.* $\mu = \mu_0$. Electrical conductivity will be shown to range over several orders of magnitude and to depend on the material, on the free or bound water content, and on the temperature. Relative dielectric permittivity, the other important property, varies

from 1 (in air) to 81 (in free water). These properties will be considered for the glacier bed, the glacier ice itself, and for mixtures of ice and rock.

2.2.1 Glacier Ice

In general the relative dielectric permittivity (ϵ_r) and conductivity (σ) of ice depend mainly on frequency, density, temperature, and concentration of impurities in the ice. (See review papers by Evans (1965), Smith and Evans (1972), Glen and Paren (1975).) In practice the frequency dependence can be ignored since the spectrum of energy used in radio echo sounding is well removed from the relaxation spectra of ice (around 100 kHz) and water (around 500 MHz) as well as the infrared absorption spectrum of ice (over a gigahertz). Density variations will also be ignored because all work on Trapridge Glacier was carried out below the firn line; hence only solid ice was encountered. In the accumulation zone or other areas where significant depths of firn occur, this aspect would have to be considered (see for example Robin and others (1969)). Concerning the dependence of ϵ_r on temperature, Paren (1970) notes that as long as the amount of free water in the ice is small, variations in ϵ_r at temperatures between $-10°$ C and $0°$ C are very small. According to Clarke and others (1984), temperatures in Trapridge Glacier are within this range so variations in ϵ_r due solely to temperature are also negligible. In the articles cited above, experimental and calculated values for ϵ_r of ice vary between 3.17 and 3.2, so $\epsilon_r = 3.18$ will be used, which implies a propagation velocity of $v = 168.2\,\mathrm{m\,s^{-1}}$.

Conductivity (σ) depends on the concentration of impurities and on temperature. Two relations are given by Smith and Evans (1972) for σ as a function of temperature, one for "pure" ice (that made from nearly distilled water) and one for ice containing an amount of solids at or beyond equilibrium solubility for solids in ice grains. Smith (1971) mentions that field measurements on temperate glaciers closely match the pure ice formula; he ascribes this to the flushing out of impurities. From Smith and Evans

(1972), this relation for conductivity of pure ice is:

$$\sigma = 4.6 \times 10^{-5} \exp\left[\frac{\mathrm{E}}{\mathrm{R}}(\mathrm{T}_0^{-1} - \mathrm{T}^{-1})\right] \mathrm{S\,m^{-1}} \tag{2.1}$$

where the activation energy $\mathrm{E} = 5.5 \times 10^4\ \mathrm{J\,mol^{-1}}$, the gas constant $\mathrm{R} = 8.314\ \mathrm{J/(mol\,^\circ K)}$ and $\mathrm{T}_0 = 273^\circ\mathrm{K}$.

Equation 2.1 can also be used for solubility limit ice at temperatures less than -10° C, but then $\mathrm{E} = 2.5 \times 10^4\ \mathrm{J\,mol^{-1}}$. Between -10° C and 0° C, excess impurities contribute to conductivity increasing it up to $6 \times 10^{-5}\ \mathrm{S\,m^{-1}}$ at 0° C.

2.2.2 Mixed Ice and Rock

Two methods for predicting relative dielectric permittivity of mixtures (ϵ_r) are listed by Glen and Paren (1975). Both methods assume that one material (with permittivity ϵ_2) is uniformly dispersed in a matrix which has permittivity ϵ_1. They use a so-called shape factor A, which describes the general form of the inclusions, and some third permittivity representing that of the material very near to and surrounding the inclusions. One formula is known as Böttcher's mixing equation:

$$\frac{\epsilon_r - \epsilon_1}{3\epsilon_r} = \frac{V_2(\epsilon_2 - \epsilon_1)}{\epsilon_2 + 2\epsilon_r} \tag{2.2}$$

in which V_2 is the volume fraction of material 2. The other equation is Looyenga's equation:

$$\epsilon_r^{1/3} = V_2\epsilon_2^{1/3} + (1 - V_2)\epsilon_1^{1/3}. \tag{2.3}$$

In both, the particles of material 2 are assumed to be spheres so that the factor $A = 1/3$. (These derivations do not make use of the "Formzahl" concept, *i.e.* the use of a single parameter to describe how one medium is dispersed in another, because this would require

that the geometry of the electric field be independent of the relative proportions of the two media. See Evans (1965) for a further discussion of this point.) Both equations given above have apparently agreed well with experiments even for high concentrations of included material. Also, comparisons of the two equations in the present case differed by less than 0.4% for $0.1 < V_2 < 0.9$. Looyenga's equation is the simplest, so it will be used in the modelling experiments discussed in chapter 3.

Conductivity of mixtures is more difficult to estimate because it depends mainly on how well interconnected the higher conductivity components are, rather than on relative volume concentrations. It is safe to say though, that the bulk conductivity of the rock/ice mixture will be less than that of ice alone since rock conductivities are several orders of magnitude less than that of ice.

2.2.3 Glacier Bed

Various types of glacier bed should be considered in the modelling since each will have different electrical parameters. Dielectric permittivity of a dry, solid rock glacier bed would be between 7 and 11; the values for solid limestone (Ulriksen, 1982) and solid basalt (St. Amant and Strangway, 1970). Corresponding conductivities would be on the order of $10^{-8}\,\mathrm{S\,m^{-1}}$. However, it is more likely that a hard glacier bed would be somewhat fractured and wet. This would raise ϵ_r by very little but σ would be raised by several orders of magnitude (Ulriksen, 1982).

For soft beds of unconsolidated debris, both frozen and unfrozen cases must be considered. Most measurements made in frozen ground indicate that $\sigma < 10^{-3}\,\mathrm{S\,m^{-1}}$ and that $4 < \epsilon_r < 7$ (*e.g.* Olhoeft, 1978; Wong and others, 1977). Ice-rich gravel is quoted by Arcone and Delaney (1981) as having $\epsilon_r = 5.1$, which agrees with the value equation 2.3 gives for a limestone gravel with about 40% porosity. This formula will therefore be used in the frozen bed model, although we should perhaps bias the values of ϵ_r upwards. This is because, as noted by Davis (1975), an increased content of very fine material

such as clay will tend to raise ϵ_r. The properties of the minerals themselves are partly responsible but a very small increase in unfrozen water will have the same effect. Anderson and others (1978, p.80) show that free water content can be more than 0.3 grams of H_2O per gram of material at between $-3°$ C and 0° C, if the soil is rich in clays or very fine-grained material. This will affect σ even more drastically since water is much more conductive than ice.

For frozen beds, equation 2.3 will again be used to find ϵ_r, this time using water as the matrix in which rock spheres are distributed. In this case, the following considerations imply that the values will only be estimates. Davis and others (1976) present experimental results giving a curve of ϵ_r versus water content that is steeper than that of the mixing formula. They also suggest, as do Hoekstra and Delaney (1974), that the relation between ϵ_r and water content is fairly independent of soil type. However, it should be noted that, unlike subglacial debris, the warm-climate surface soils used by these authors are probably rich in clay and organic material. The effect on ϵ_r of clay concent was mentioned above, and Arcone and Delaney (1982) note that increased organic matter tends to increase ϵ_r.

The difficulties of assessing σ in mixtures were noted above but more literature is available on conductivity of wet ground than that of frozen ground. Based on the review article by Keller (1967), bulk conductivity of subglacial debris was found using the Archie formula for weakly cemented detrital rocks in which porosity is between 25% and 45%. This formula is appropriate because till samples from areas that were once over-ridden by Trapridge Glacier are thought to have porosities of 20% to 40%. The relation is

$$\frac{1}{\sigma_T} = \frac{0.88}{\sigma_w}\phi^{-1.37}, \tag{2.4}$$

in which σ_T is bulk conductivity, σ_w is the conductivity of interstitial water and ϕ is porosity. In order to find the bed conductivity, σ_w is obviously required but it is difficult to obtain the true value of *in situ* water. Samples taken directly from the bed cannot be used because of contamination by drilling water, subglacial runoff is likely to be mixed with surface melt in the summer months, and in both cases, simply exposing a sample to air and measuring equipment can cause chemical changes which will alter the resistivity.

Reasonable estimates can be made, however, by referring to other work and by considering the local environment. An eleven-month study by Collins (1981) of water draining from the snout of Gornergletscher, Switzerland, revealed a maximum conductivity of $120\,\mu\mathrm{S\,cm^{-1}}$ in the winter when surface melt was at a minimum. Spot measurements made in July 1986 around Trapridge Glacier revealed conductivities of 20 to $80\,\mu\mathrm{S\,cm^{-1}}$ for surface melt and up to $650\,\mu\mathrm{S\,cm^{-1}}$ for ground water (C. Smart, pers. comm., 1986). Local geology also suggests that carbonate rocks constitute a large proportion of Trapridge Glacier's bed so that the solute concentration of subglacial water is likely to be high. In addition, Keller (1967) notes that *in situ* conductivity of interstitial water is increased by ionization of clay minerals and by surface conductance such that pore water conductivities are rarely less than $100\,\mu\mathrm{S\,cm^{-1}}$ in sandstone or $1000\,\mu\mathrm{S\,cm^{-1}}$ in siltstone. These do not necessarily apply in our case since the glacier bed is likely to be a poorly sorted mixture of the various clasts produced by subglacial geologic processes (Drewry, 1986: ch. 3-5), but similar effects on σ_w might be expected. All of these considerations suggest that a likely range of values would be $10^2\,\mu\mathrm{S\,cm^{-1}} < \sigma_w < 10^3\,\mu\mathrm{S\,cm^{-1}}$.

To summarize, I have introduced the basic physical parameters that will appear in the equations describing electromagnetic pulse propagation and reflection within glaciers, and discussed the physical features affecting them. Their values may be expected to be within the ranges listed in table 2.1. Although the uncertainties are quite large for some

Table 2.1: Electrical parameters

material	*parameter*	*min.*	*max.*	*comments**
ice	ϵ_i	3.17	3.2	a
	σ_i (S m^{-1})	6×10^{-1}	2×10^{-1}	a, b
mixed	ϵ_m	3.18	11.0	c
layer	σ_m (S m^{-1})	10^{-8}	6×10^{-5}	d
glacier	ϵ_t	7.0	81	c
bed (wet)	σ_t (S m^{-1})	10^{-3}	10^{-1}	e, f

* Comments: Parameters depend mainly upon (a) temperature; (b) concentration of impurities; (c) concentration of solids in matrix; (d) connectivity (or permeability); (e) conductivity of interstitial water (σ_w); (f) porosity.

parameters, one of the purposes of the modelling discussed later will be to determine how significantly these parameters affect the shape of echoes.

2.3 PROPAGATION

Having defined the "primary" constants (ϵ, σ, μ) of the media in which pulses will be propagating, we can find expressions for the electric field strength $E(r,t)$ by solving the general electromagnetic wave equation. This is done in many texts on electromagnetic wave theory (for example Jordan and Balmain (1968, section 5.05)) with the result

$$E(r,t) = \mathcal{E}\frac{1}{r}e^{-\gamma r}e^{j\omega t} \tag{2.5}$$

where: r is the distance from the source; ω is angular frequency; $\gamma = \sqrt{(j\omega\mu)(\sigma + j\omega\epsilon)} = \alpha + j\beta$ is the propagation constant; $\mathcal{E} = \sqrt{g_p W_t \eta / 4\pi}$ is a source term found using fundamental antenna relations discussed by Jordan and Balmain (1968: section 11.11); g_p is the antenna's power gain (a measure of efficiency and directionality); W_t is the total input power; and $\eta = \sqrt{j\omega\mu/(\sigma + j\omega\epsilon)}$ is the intrinsic impedance of the medium in which the antenna lies.

All the primary constants are some combination of those applicable in ice and air; recall that the antennas are resting at the interface of these two effectively infinite dielectric semiconductors.

Equation 2.5 shows that the electric field strength is inversely proportional to distance from the source, is further reduced according to the attenuation constant α, and may be phase shifted according to the phase constant β. Simplification of α and β is possible if the ratio $(\sigma/\omega\epsilon) \ll 1$ (valid in good dielectrics) or if $(\sigma/\omega\epsilon) \gg 1$ (valid in good conductors). For example, at 1 MHz typical ice has

$$\frac{\sigma}{\omega\epsilon} = \frac{3.0 \times 10^{-5}}{(2\pi \times 10^6 \times 8.854 \times 10^{-12} \times 3.18)} = 0.17 \ .$$

Since this is not conclusively much less than 1, figure 2.1 was constructed to demonstrate that propagation of signals between 400 kHz and 25 MHz is practically non-dispersive. Figure 2.1a shows the magnitude of α for both warm and cold ice. As a comparison, figure 2.1b shows that propagation in till will be highly attenuative as well as highly dispersive. Arcone (1981) discusses a similar problem by modelling the propagation of pulses centered around 85 MHz through a medium similar to frozen ground, but this will be unnecessary in our case.

A complete treatment of electromagnetic wave propagation in ice must also include scattering processes, especially when temperate glaciers are being considered. Smith and Evans (1972) consider scatterers as small (with respect to wavelength) dielectric spheres that re-radiate incident energy by becoming electric dipoles (Rayleigh scattering). Their formulae show that the power lost from the forward wave per unit length of path through the medium is

$$\delta = \frac{8\pi}{3} m b^6 \left(\frac{2\pi}{\lambda}\right)^4 \left[\frac{\epsilon_2(\epsilon_1 - \epsilon_2)}{\epsilon_1 + 2\epsilon_2}\right]^2 \qquad (2.6)$$

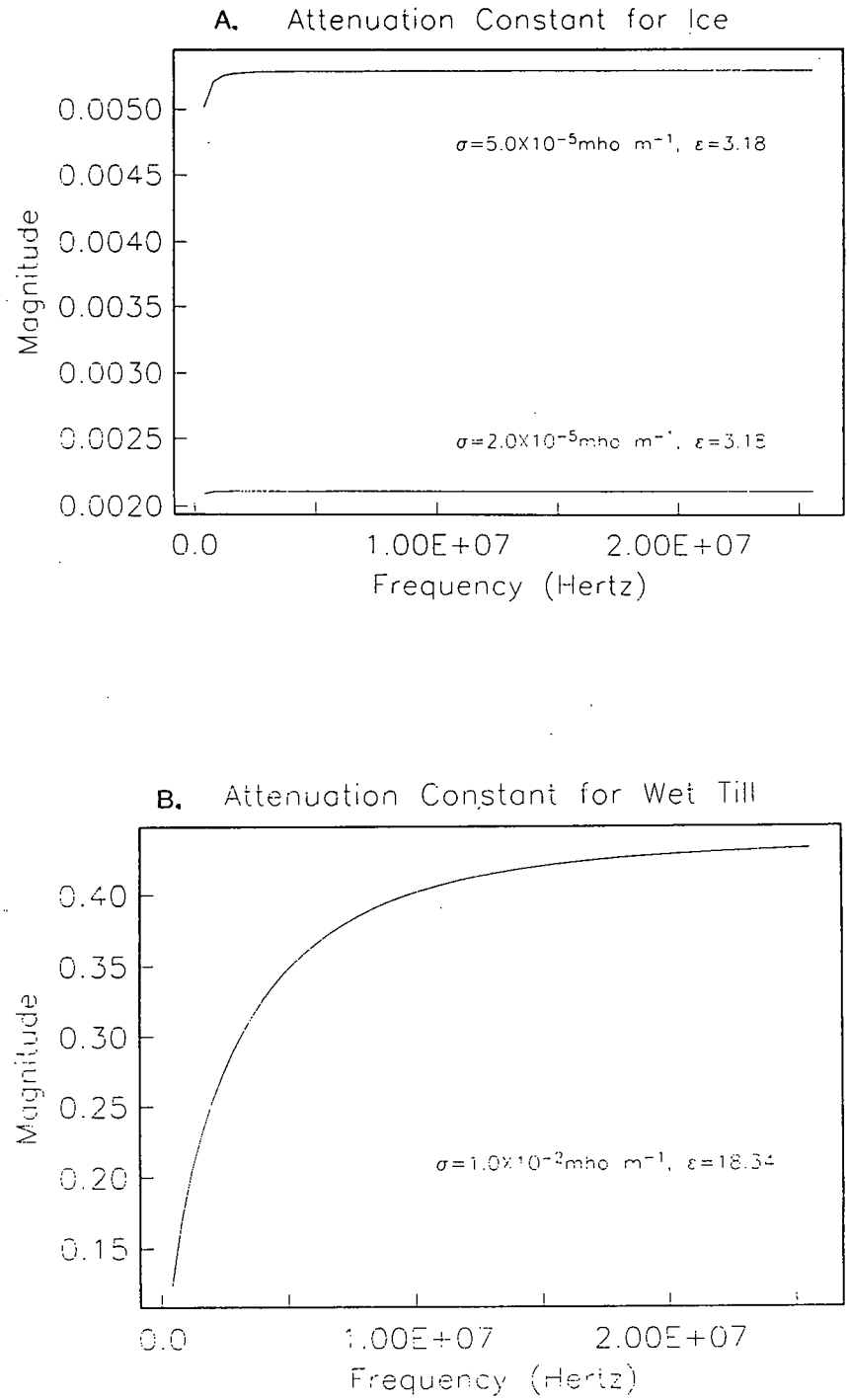

Figure 2.1. Attenuation constant α, determined from the propagation constant γ of equation 2.5. Conductivity and permittivity used in each case are noted inside the graphs, and the media in which propagation is occurring are noted as titles to the graphs. A) α for both warm and cold ice. Warm ice has $\sigma = 5 \times 10^{-5}$ S m^{-1}; cold ice has $\sigma = 2 \times 10^{-5}$ S m^{-1}. B) In wet till, attenuation is much more pronounced and dispersion occurs at all frequencies. Till porosity was 30%.

where m is the number of scatterers per unit volume, b is the radius of spherical scatterers, ϵ_1 and ϵ_2 are relative permittivities of the scatterers and medium, and λ is the wavelength in the medium. This proves to be negligible for frequencies less than 500 MHz if scatterers are reasonable configurations of air- or water-filled bubbles in ice or firn. Masking of target echoes by scattered energy is considerably more significant. Watts and England (1976) use a similar but more general theory to that presented by Smith and Evans (1972) to suggest that water-filled voids smaller than 1 m in diameter will not obscure target echoes as long as sounding frequencies are below 5 MHz. It will be seen in data presented later that results from Trapridge Glacier are virtually unaffected in this way, probably because most of the glacier is colder than the pressure melting point (Clarke and others, 1984). For the sake of completeness, however, it is worth noting that masking effectiveness can be described by a signal-to-noise ratio when the power (P_p) from the target is the signal and power scattered from an equivalent range (P_s) is noise. Equation 11 from Watts and England (1976) gives this ratio as

$$\frac{P_p}{P_s} = \frac{Rg_0^2}{2ml\kappa g_{bs}G} \tag{2.7}$$

in which: R is the reflection coefficient of the target; g_0^2/G is the ratio of squared antenna gain to antenna directionality; m is the number of scatterers per unit volume; l is the pulse length in ice; and κg_{bs} is the product of scattering cross-section and backscatter gain (which allows non-spherical scatterers to be considered).

2.4 REFLECTIONS

So far, only propagation in infinite media has been considered. If a change in primary characteristics is encountered, some energy will be transmitted through this boundary and some will be reflected back. For normal incidence on a plane, smooth boundary

(a specular reflector) the ratio of returned to incident energy is given by the amplitude reflection coefficient

$$\rho = \frac{\eta_2 - \eta_1}{\eta_2 + \eta_1} \tag{2.8}$$

where the incident energy is travelling in a medium with impedance η_1 and medium 2 is the other side of the boundary. Similarly the transmission coefficient τ is

$$\tau = \frac{2\eta_2}{\eta_2 + \eta_1} \, . \tag{2.9}$$

Clearly a boundary with greater impedance contrast will reflect more energy back and transmit less into the second medium. Also, if the impedances are frequency-dependent, the echoing process will be dispersive. Table 2.2 summarizes representative values of ρ for different reflectors. Note that throughout this thesis, complex reflectivities are expressed in phasor notation: $\rho = \mathrm{Re}(\rho) + \mathrm{j}\,\mathrm{Im}(\rho)$ is given as $\rho = |\rho| \angle \tan^{-1}\big(\mathrm{Im}(\rho)/\mathrm{Re}(\rho)\big)$.

Table 2.2: Reflection coefficients

i	j	σ_j (S m^{-1})	ϵ_j	ρ_{ij}	$\lvert\rho_{ij}\rvert$ (dB)
air	ice	5×10^{-5}	3.18	0.28∠180	-11.1
ice	air	0.0	1	0.28∠0	-11.1
ice	water	0.01	81	0.67∠179	-3.5
ice	limestone	10^{-8}	7	0.19∠176	-14.5
ice	till $\phi = 15$*	8.5×10^{-4}	11.8	0.32∠177	-9.9
ice	till $\phi = 15$†	5.1×10^{-3}	11.8	0.44∠164	-7.1
ice	till $\phi = 30$*	2.2×10^{-3}	18.3	0.42∠176	-7.5
ice	till $\phi = 30$†	1.3×10^{-2}	18.3	0.59∠167	-4.6

ρ_{ij}, calculated using equation 2.8, is given as magnitude and phase angle of the reflection coefficient for electromagnetic waves travelling in material "i" and incident on a smooth boundary with material "j". Note that a phase angle of 180° implies an effectively negative reflection coefficient. ϵ_j of mixtures was found using equation 2.3. σ_j was found using equation 2.4.

* using $\sigma_w = 0.01$ S m^{-1}

† using $\sigma_w = 0.06$ S m^{-1}

A more realistic reflector consists of a relatively thin layer of a third material separating two half spaces. This allows more accurate modelling of glacier beds which may include a thin film of water or a basal layer of mixed ice and debris. Drewry (1986: ch. 7) discusses various mechanisms that can create such a layer (called a glacier sole by Post and LaChapelle (1971)), and Maxwell (1986) considers in detail the observed basal layer under Trapridge Glacier. (An analogous situation in optics would be the reflection of light from thinly coated surfaces.) An expression for the appropriate reflection coefficient can be found by considering all the multiple reflections within the thin layer and summing their contributions to the output signal as an infinite series. The resulting frequency-dependent amplitude reflection coefficient is

$$R(\omega) = \rho_{im} + \frac{\tau_{im}\rho_{mt}\tau_{mi}e^{-2\gamma_m x}}{1 - \rho_{im}\rho_{mt}e^{-2\gamma_m x}} \tag{2.10}$$

which contains the following parameters: reflection coefficients of two boundaries ρ_{im} and ρ_{mt}; transmission coefficients at the first boundary τ_{im} and τ_{mi}; propagation constant of the middle layer γ_m; and the thickness of the layer x. In these, subscripts i, m, and t denote ice, middle layer, and till or bedrock respectively. Reflections from this boundary are even more dispersive than the simple case of equation 2.8; frequency responses of these reflectors are considered in detail in the chapter on modelling.

In this thesis, these results will not be generalized to include non-specular and rough reflectors although there are several ways to proceed. Many conventional radar systems record rectified envelopes of returning signals so phase information is lost. Nevertheless spatial and temporal fading of such records can be used to estimate statistical properties of small-scale reflector roughness, as well as whether the roughness is blocky, undulating, or smooth with patchy variations in permittivity. Berry (1975) and Oswald (1975) discuss these methods which are based on Kirchhoff diffraction theory; they also discuss how to

use the same data to infer large-scale bed topography. A second approach uses an instrument capable of recording the phase of conventional radar echoes. This type of data is used by Walford and Harper (1981) who apply Berry's diffraction theory, as well as concepts akin to downward continuation of wave fields, to the interpretation of detailed glacier bed shape. In order to improve the resolution of their interpretations, they also consider a form of aperture synthesis. All these methods were developed for use with quasi-monochromatic radar data so would need to be modified for application to wide-band impulse radar data. The similarity of impulse radar to seismic sounding suggests that the vast body of seismological literature could be tapped with a view to resolving some of these differences. Walford and Harper (1981) mention that they were considering the application of their work to impulse radar data, and a PhD. dissertation on that work is currently in preparation by M. Kennett under Walford's supervision.

CHAPTER III

DIGITAL MODELLING AND DATA ENHANCEMENT

3.1 INTRODUCTION

In many respects, radio frequency echo sounding can be conveniently compared to seismology, the main difference of course being that pulses of electromagnetic energy are used instead of acoustic energy. As in seismology, propagation and reflection of pulses can be analyzed by considering these processes as a sequence of filtering operations (figure 3.1a). Since these operations are linear, they can be conceptually rearranged to isolate any process of particular interest. In this study glacier bed properties are being investigated, so the system is rearranged as per figure 3.1b which can be described in the frequency domain by the equation

$$E(\omega) = E_0(\omega)R(\omega) \ . \tag{3.1}$$

The assumption is that all the processes that have been lumped together to create the input wavelet $E_0(\omega)$ are well defined and that a solvable expression for the reflection coefficient $R(\omega)$ can be found which involves the interesting bed characteristics.

The general reflector model considered in this work consists of a relatively thin layer of some material separating two half spaces, ice and glacier bed. Chapter 2 presented a discussion of this reflector and the materials involved; the equation is reproduced here for convenience:

$$R(\omega) = \rho_{im} + \frac{\tau_{im}\rho_{mt}\tau_{mi}e^{-2\gamma_m x}}{1 - \rho_{im}\rho_{mt}e^{-2\gamma_m x}} \ . \tag{3.2}$$

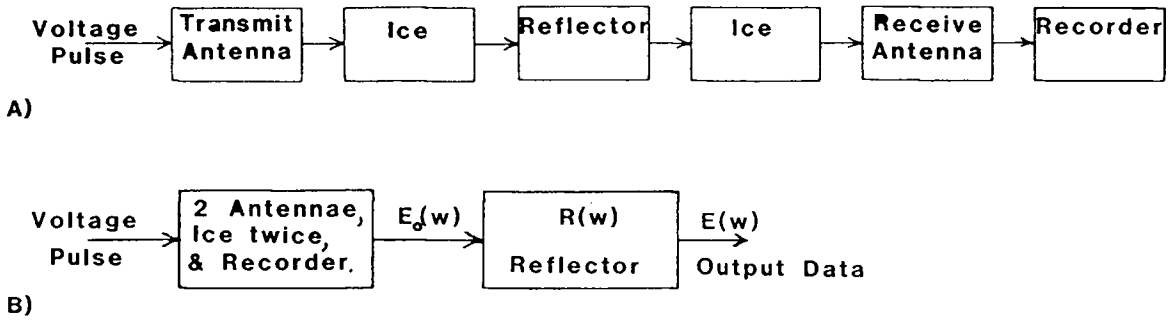

Figure 3.1. (A) Electromagnetic echo sounding modelled as a sequence of filtering operations. Six filters are required to describe the processes of pulse generation, propagation, reflection and reception. (B) The system rearranged to isolate the reflection process. $E_0(\omega)$ and $E(\omega)$ are the input and output wavelets and $R(\omega)$ is the reflection filter's impulse response.

The parameters are: reflection coefficients of two boundaries, ρ_{im} and ρ_{mt}; transmission coefficients at first boundary, τ_{im} and τ_{mi}; propagation constant of middle layer γ_m; and thickness of the layer x. The subscripts i, m, and t denote ice, middle layer and till or bedrock respectively. It should be noted again that equation 3.2 is a simplified model which assumes that plane waves are impinging at normal incidence on a plane, specular reflector and that the media in which propagation occurs are homogeneous dielectric semiconductors.

All the components in this equation are frequency-dependent, so reflection from a boundary of this type is, in effect, a dispersive process. Therefore echoes of wideband impulse radar signals might be expected to show changes in character that can be interpreted in terms of the properties of the two-boundary reflector. On the basis of this expectation, one plan for analysis would be to estimate bed characteristics from field data by using a forward modelling scheme. The relations from chapter 2 would be used in equation 3.2 to find $R(\omega)$ and equation 3.1 would then be solved repeatedly using various values for the parameters (ensuring of course that the values chosen make physical sense). The calculated data $E(\omega)$ obtained in these trials could then be compared to the

true data, the parameters readjusted, and further trials carried out until a reasonable match was obtained.

The difficulty encountered with this scheme is the common geophysical problem of wavelet estimation. In order to solve equation 3.1, the input wavelet $E_0(\omega)$ must be determined. This involves determining the transfer functions of all those operations in figure 3.1a that have been lumped together as one in figure 3.1b. Of these, propagation through ice can be approximated as a non-dispersive, attenuating process (shown in chapter 2) and the recording apparatus can be considered transparent for our purposes. The actions of the antennas on the other hand must be carefully considered if the wavelet is to be determined analytically. A short digression is required here to explain this point.

Chapter 4 shows how the echo sounding impulse is generated by impressing a high voltage step function onto a damped dipole antenna. The behavior and impulse response of such an antenna in free space is discussed by Kanda (1980) for both receiving and transmitting modes of operation. In our case however, there are several complications. We have not yet determined the current as a function of position on the antenna arms, the antennas are not in free space but at the interface of two infinite dielectrics (air and ice), and we would have to consider both near and far field components in the radiating equations. Incorporating Kanda's transfer equations in this analysis is therefore far from simple. As a result, rather than beginning by solving this problem, the first job is to determine whether real reflectors will have any significant effect on electromagnetic pulses such as those used in impulse radar.

Some kind of estimated wavelet is therefore required. It is noted in chapter 4 that, because of propagation effects, the signal $E_0(\omega)$ will have at best three lobes. A convenient waveform of this type is the so-called Ricker wavelet; a zero phase wavelet used extensively by seismologists which is given by equations 3.3 and 3.4 from Sherriff and

Geldart (1982):

$$e_0(t) = (1 - 2\pi^2\omega_m^2 t^2)\exp[-\pi^2\omega_m^2 t^2] \tag{3.3}$$

$$E_0(\omega) = \left(\frac{2}{\sqrt{\pi}}\right)\left(\frac{\omega^2}{\omega_m^3}\right)\exp[-\omega^2/\omega_m^2], \qquad \phi(\omega) = 0\ . \tag{3.4}$$

Further justification for using a Ricker wavelet in the modelling can be seen in figure 3.2. A real echo is shown to have a magnitude spectrum that is very similar to that of a Ricker wavelet, and the echo itself looks like a phase rotated Ricker wavelet. If we assume that phase rotation is caused by complex propagation processes, then a Ricker wavelet is a reasonable input signal to start with.

As a result of these considerations, the modelling experiments discussed in this chapter involved solving equation 3.1, with equation 3.2 as the filter impulse response $R(\omega)$ and a Ricker wavelet as the input $E_0(\omega)$. Various versions of $R(\omega)$ were tried and the resulting output wavelets were compared to the original Ricker wavelet. In this way, parameters affecting echo shape were determined and estimates were made of the range of values revealed by real data.

3.2 FILTER MODELLING

3.2.1 Sampling

Before carrying out the modelling procedure itself, the sampling parameters must be set to ensure that field data, modelled data and filters are compatible. The one fixed parameter is the sampling rate of field data. This was measured to be very close to the design specification of $\Delta t = 10\,\mu\text{s}/1024\,\text{samples} = 9.766\,\text{ns/sample}$. Next, the number of points considered adequate to yield useful results without compromising either numerical accuracy or computational efficiency was chosen to be $n = 128$ points. Filters are constructed in the frequency domain and are made compatible with these data sets by setting the frequency sampling interval at $\Delta f = f_N/128$, where f_N is the Nyquist frequency, the

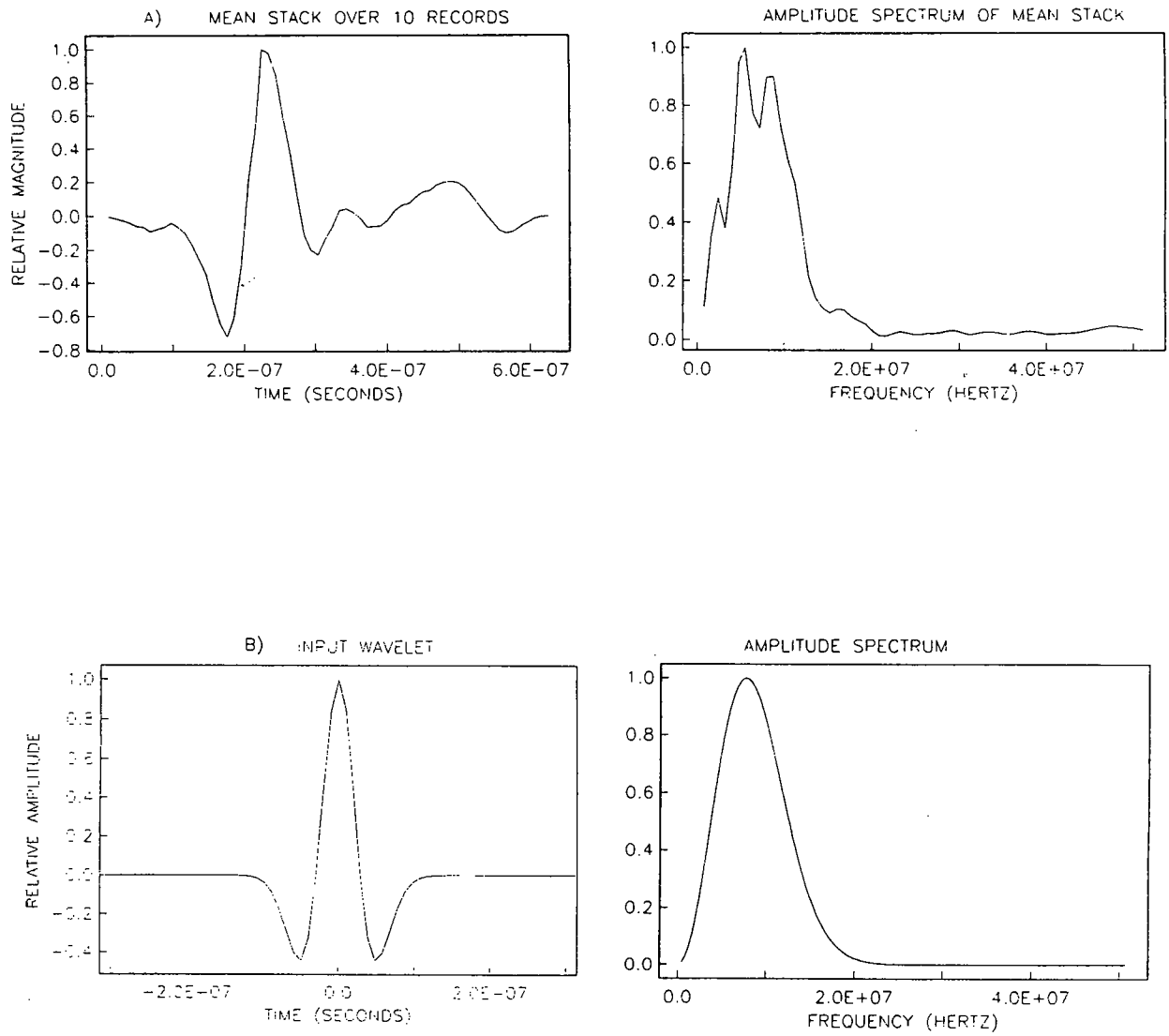

Figure 3.2 (A) An average wavelet and its spectrum. This is the mean stack over records 24 to 33 from the close-spaced survey (chapter 6). The 64 point data window consists of samples 120 to 184. (B) A Ricker wavelet and its spectrum. Note that ω_m (used in equations 3.3 and 3.4) is the frequency with maximum amplitude.

highest frequency reproducible with the given sampling rate. Therefore $\Delta f = 400.2\,\text{kHz}$ and filters were calculated at 128 positive frequencies from 0 to 51.23 MHz. The Ricker wavelet $E_0(\omega)$ (or $e_0(t)$ in the time domain) was calculated with the same sampling interval (Δf or Δt) using equations 3.3 or 3.4. It was made to resemble field data as closely as possible by setting the parameter ω_m close to the approximate peak frequency of real data. It will be shown later that reasonable reflectors can be expected to emphasize low frequencies so, since figure 3.2a depicts an echo, the estimate of $E_0(\omega)$ has used a maximum frequency of $f_m = \omega_m/2\pi = 7.7\,\text{MHz}$ which is slightly higher than that of the average signal in figure 3.2a.

3.2.2 Forward Modelling

Glacier bed properties will now be examined using forward modelling. In order to facilitate what is basically a trial and error process, a two-step procedure is employed. The first program calculates the reflection coefficient $R(\omega)$. It uses the 10 basic parameters listed in table 3.1 to generate a set of $R(\omega)$s over which any one of the parameters may be varied. The second program then passes an input wavelet $E_0(\omega)$ through each one of these filters and plots the output wavelets so that the effects of varying one parameter at a time can be easily examined.

First consider the program for calculating $R(\omega)$. Details will not be dwelt upon but it is worth pointing out some of the important features. The sampling constants (Δf, Δt, and n) are set first and passed to the second program to ensure consistent processing. Options such as whether the glacier bed is to be wet or frozen are chosen interactively and a list is kept of the initial input parameters (table 3.1) as well as those subsequently calculated. The relations of chapter 2 are used to calculate the final $R(\omega)$, which consists of complex amplitudes at 128 frequencies from 0 to 51.23 MHz. The last few points of this spectrum are tapered to ensure a smooth transition to zero amplitude at the edge of the spectrum. This minimizes oscillations when inverse transforming to

Table 3.1. Input parameters to the program which constructs $R(\omega)$.

Conductivity of glacier ice	σ_i
Permittivity of glacier ice	ϵ_i
Conductivity of mixed layer	σ_m
Volume fraction of rock in mixed layer	V_{rockm}
Permittivity of rock in mixed layer	ϕ_m
Thickness of mixed layer	x
Bulk conductivity of frozen layer	σ_t
Conductivity of interstitial water	σ_w
Volume fraction of rock in till	V_{rockt}
Permittivity of rock in till	ϵ_t

the time domain, and is done by multiplying the last eight points with a cosine bell function as per Kanasewich (1981, section 9.3). If more than one version of $R(\omega)$ is to be produced, their spectra are listed sequentially so that the second program can use them in successive runs.

The filtering itself is carried out by the second program. Unless otherwise requested, the input to the filter $E_0(\omega)$ will be a Ricker wavelet constructed with the sampling parameters specified by the first program. The filtering can be carried out either by multiplication in the frequency domain or by convolution in the time domain; use of both helps validate the results. If a set of $R(\omega)$s is available, the corresponding final output wavelets (and/or spectra) are plotted to facilitate comparisons between them.

3.2.3 Glacier Bed Filters

Results from various filtering experiments will now be presented, starting with examples of reflection coefficients generated by program 1. Figure 3.3a shows the magnitude spectrum of $R(\omega)$ for a model consisting simply of glacier ice resting on a wet till bed with 30% porosity. The increased amplitudes at lower frequencies occur because the intrinsic impedance of till approaches 0 at $\omega = 0$. Also shown is the time domain representation

(A) $R(\omega)$ & $r(t)$ FOR ICE/TILL INTERFACE; PARAMETERS LISTED BELOW.

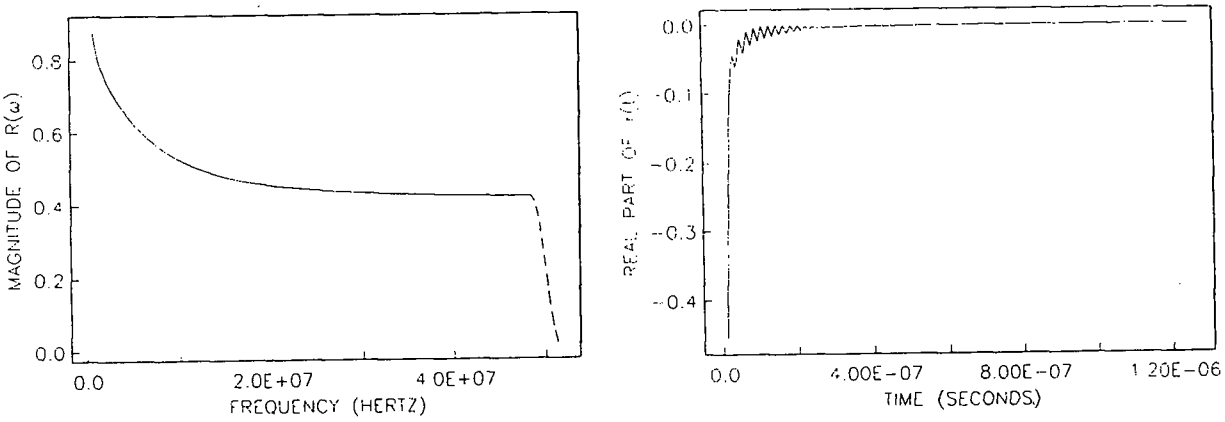

(B) $R(\omega)$ & $r(t)$ FOR 3 m THICK LAYER; PARAMETERS LISTED BELOW.

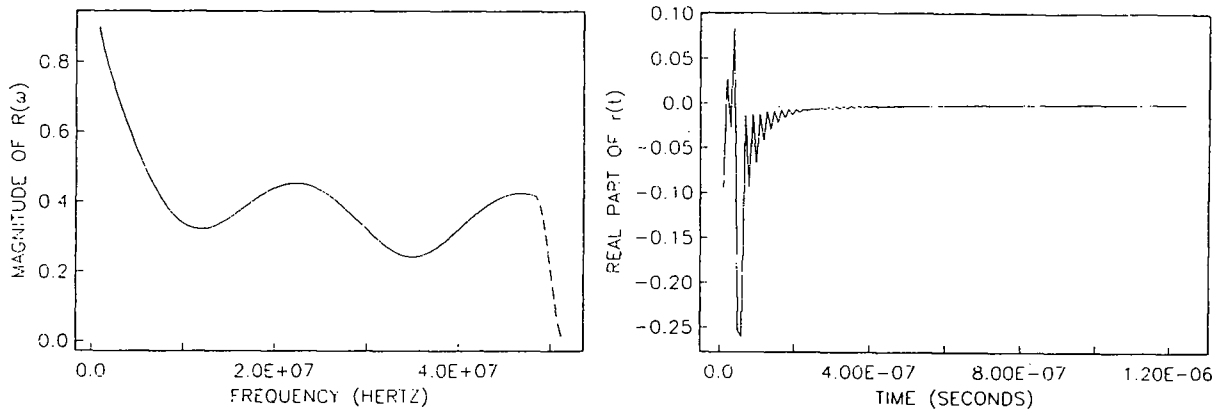

PARAMETERS OF REFLECTOR

CONDUCTIVITY OF GLACIER ICE;	SIGMAI= 0.29999996E-04
PERMITTIVITY OF GLACIER ICE;	EPSI= 3.1800003
CONDUCTIVITY OF MIXED LAYER;	SIGMAM= 0.90000001E-04
VOLUME FRACTION OF ROCK IN MIXED LAYER;	VROCM= 0.39999998
PERMITTIVITY OF ROCK IN MIXED LAYER;	EPSRCM= 7.0000000
THICKNESS OF MIXED LAYER;	THIC= 3.0000000
BULK CONDUCTIVITY OF FROZEN TILL;	SIGMAT= 0.10000003E-05
CONDUCTIVITY OF INTERSTITIAL TILL WATER	SIGMAW= 0.50000001E-01
VOLUME FRACTION OF ROCK IN TILL;	VROCT= 0.69999999
PERMITTIVITY OF ROCK IN TILL;	EPSRCT= 7.0000000
PERMITTIVITY OF BASAL MIXED LAYER IS (CALCULATED FROM VROCM,EPSI AND EPSRCM)	EPSM=4.4717
PERMITTIVITY OF GLACIER BED (WET) IS (CALCULATED FROM MIXTURE FORMULA)	EPST=18.339
CONDUCTIVITY OF WET GLACIER BED IS (CALCULATED USING SIGMAW & VROCT IN THE ARCHIE FORMULA FOR POORLY CONSOLIDATED SEDIMENTS)	SIGMA=.10918E-01

Figure 3.3 Spectra and time domain filter responses of two models. Signals used with these filters are bandlimited below 20 MHz; see figure 3.2. The last eight points of the spectra are tapered to zero. Important characteristics used or calculated by the program are listed in the table. (A) Glacier ice resting directly on a wet till bed. (B) Same but including a 3 m thick layer of mixed ice and rock between the ice and bed.

of the filter. It is an approximate delta function at time zero; the approximation would become closer to a true Dirac delta if the filter was less frequency-dependent. Small oscillations are a result of imperfectly approximating the spectrum near the Nyquist frequency. They are insignificant in our case because signals are bandlimited to less than 20 MHz (see figure 3.2). The parameter most responsible for frequency dependence is the conductivity of interstitial water σ_w. Higher values of σ_w result in larger $R(\omega)$ at the lower frequencies, although the asymptote at high frequencies is unaffected. Note that this asymptote is 0.412 but that the last eight points are tapered to zero. The asymptote can be verified by solving an approximate formula for the reflection coefficient for the case in which the ratio $\sigma/\omega\epsilon \ll 1$ (Jordan and Balmain, 1968). In this case, the intrinsic impedance η approaches $\sqrt{\mu/\epsilon}$ so that

$$|R(\omega_\infty)| = \left| \frac{\sqrt{\epsilon_t^{-1}} - \sqrt{\epsilon_i^{-1}}}{\sqrt{\epsilon_t^{-1}} + \sqrt{\epsilon_i^{-1}}} \right| = 0.412$$

where $\epsilon_t = 18.34$ and $\epsilon_i = 3.18$ from the list of figure 3.3a.

Inserting a layer 3 m thick consisting of 40% rock and 60% ice results in the filter spectrum shown in figure 3.3b. Features of note include the increased amplitudes at lower frequencies (similar to figure 3.3a) and the oscillating nature at higher frequencies. This occurs as a result of interference within the layer which results in minimum echo amplitudes occurring at frequencies for which the layer thickness x is an odd multiple of a quarter wavelength (that is the wavelength within the layer). In this example, $x = 3$ m and velocity in the layer is $v = c/\sqrt{\epsilon_r} = 300/\sqrt{4.472} = 141.9\,\mathrm{m}\,\mu\mathrm{s}^{-1}$, so there should be minima in the spectrum at $f_n = (2n-1)v/4x$ or at $f = 11.83$ MHz, 35.48 MHz, ... This is confirmed in the figure. These phenomena affect a significant portion of the wavelet spectrum (see figure 3.2), emphasizing the importance of utilizing exact, complex

relations throughout the modelling process. Also noticeable in the second example is the decaying amplitude at higher frequencies, due to conductive losses in the middle layer. Finally, note how the time domain response implies that there will be two main echo features, a small echo from the top interface (the ice/mix boundary) and the main echo from the lower boundary across which there is a greater impedance contrast. The effect on an incident pulse will be seen in figure 3.3.

3.2.4 Filtering Results

The final modelling experiments can now be discussed, in which reflection coefficients such as those above are used as the impulse responses of filters and the Ricker wavelet of figure 3.4a is used as the input. Figure 3.4b shows a set of output wavelets calculated using the simple model of glacier ice resting on a porous till bed. A different porosity was used when generating each wavelet. As expected, greater porosity results in stronger reflections since the presence of more interstitial water raises the intrinsic impedance of the glacier bed. Further experiments showed that, in a bed with 30% porosity, variations of water conductivity in the range $10^{-4}\,\mathrm{S\,m^{-1}} < \sigma_w < 10^{-1}\,\mathrm{S\,m^{-1}}$ yielded minor changes of echo amplitude, with minor phase shifts becoming apparent for $\sigma_w > 10^{-2}\,\mathrm{S\,m^{-1}}$.

For figure 3.4c, a layer consisting of 40% rock and 60% ice was inserted between the glacier ice and a bed with 30% porosity. Over the first six trials, the thickness (x) of this layer was varied from 0 to 5 m, and for the last, $x = 5$ m and the bed was assumed frozen instead of wet. The impedance contrast from middle layer to bed is therefore reduced, resulting in a smaller echo. It should be made clear at this point that the time axis represents delay time in seconds after receipt of the echo from the first boundary, *i.e.* the ice/middle layer boundary. So, for the 5 m thick layer (with velocity of propagation $v = 141.9\,\mathrm{m}\,\mu\mathrm{s}^{-1}$ as mentioned previously), the first and therefore strongest return from the lower boundary appears after a two-way travel time of $t = 2x/v = 7.05 \times 10^{-8}$ s.

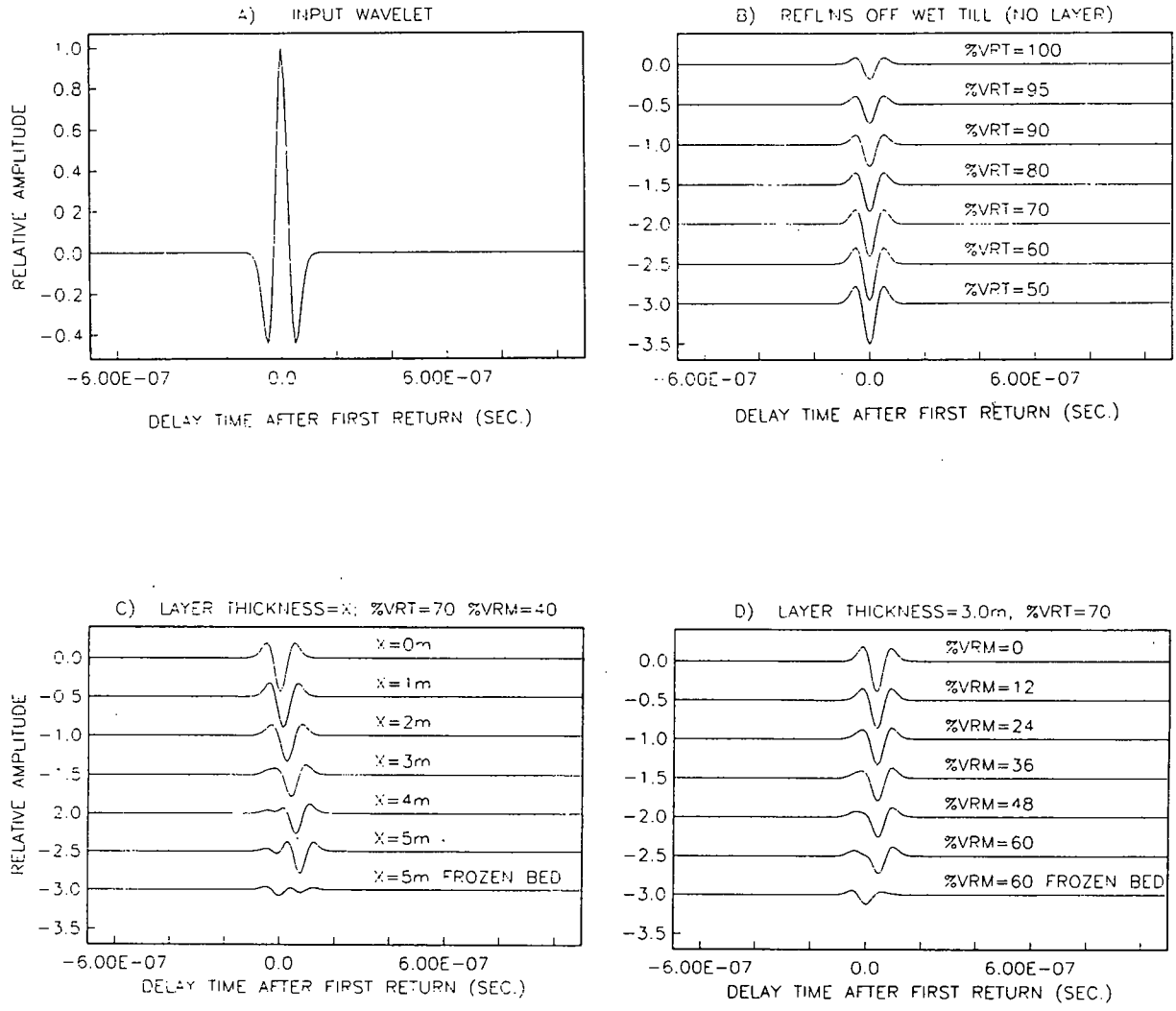

Figure 3.4 Results of filtering experiments. (A) The wavelet $e_0(t)$ that is incident on the reflector, *i.e.* the filter input. (B) Seven trials with a model of ice on a wet till bed. All parameters are kept constant except for the percent volume of rock in the till bed. The uppermost record represents an echo from a bed with 100% rock by volume. The other models have glacier beds consisting of varying amounts of uniformly dispersed rock spheres in a water matrix. (C) Now the model includes a thin layer between ice and bed. Layer thickness x is varied in six steps as per the figure title. The last record assumed a frozen bed. Percent volume of rock in the layer (%VRM) is 40% and in the bed (%VRT) is 70%. (D) Same as C but thickness is constant at 3.0 m and percent volume of rock in the layer is varied from 0% to 60%.

The final frame of figure 3.4 shows results from a model with $x = 3\,\mathrm{m}$ and a glacier bed porosity of 30%. Percent volume of rock in the middle layer was varied from 0 to 60%. This figure suggests that it would be difficult to accurately determine thin layer characteristics such as rock content from radar data such as ours. Visible effects to the wavelet occur only for layer thicknesses greater than about 3 m and for rock concentrations greater than about 35%. Such layers are not uncommon however (Drewry, 1986; Maxwell, 1986) so these results suggest that subglacial layers must be considered when interpreting data.

One more glacier bed studied consisted of a layer of wet till between ice and solid bedrock. Results confirmed the suspicion that the till/bedrock interface would be nearly invisible because the ice/till interface reflects most of the incoming energy and the till layer itself is highly attenuating.

Finally, it is interesting to examine whether a thin layer of water at the glacier bed (or a Weertman film (Drewry, 1986)) will be visible to the radar. Table 2.2 gives a summary of reflection coefficients for single boundary reflectors. Consider the result of using these in equation 3.2. If the thickness of the water film is $x < 4$ mm, then $e^{-2\gamma x} \approx 1$ and equation 3.2 becomes $R \approx \rho_{iw} + 0.25/-58.2° = 0.40/164°$. This is similar to the coefficient for wet till and not far from that of solid rock (see table 2.2). The implication is that these various reflectors would be difficult to distinguish given the type of data we have, a difficulty elaborated upon in chapter 6.

3.3 DATA ENHANCEMENT

These experiments demonstrate that variations of reflector parameters of glaciological interest will cause only small changes in echo character. Examination of field data suggests that such subtleties are likely to be masked by other contributions making up the complete signal. These will include the wavelet itself, large-scale reflector characteristics

(such as the bulk properties of ice), and random noise. Clearly what is needed is some method of discriminating between the various components of the final complete echo.

3.3.1 Alignment and Mean Stack

If large-scale reflector properties are of interest, the simplest way to eliminate small-scale features is to find an average across the section or, in seismological terminology, to generate a mean stack. For best results this requires the removal of any so-called residual statics, which are minor shifts in echo return time not due to changes in reflector depth. Timing anomalies do exist in data gathered with the UBC instrument and are caused by hardware instabilities that have not yet been corrected. An automatic aligning program has therefore been used across sections when true depth information is no longer of interest but bed properties, *i.e.* echo shape, are.

To align each trace, time shifted or "lagged" versions of the trace are cross-correlated with a reference trace, and the lag which yields the highest correlation value is used to shift the trace in question. The window over which correlations are calculated and the number of time shifts tried for each trace are both chosen interactively to help minimize computational expense. To state the procedure more formally, lagged or time shifted versions of the trace to be aligned, $x_n(t)$, are cross-correlated with the reference trace, $x_1(t)$, using equation 3.5 (see for example Kanasewich, 1981: ch. 6).

$$X_L(t) = \frac{1}{(t_2 - t_1)} \sum_{i=t_1}^{t_2} x_1(t_i) \times x_n(t_i + L) \tag{3.5}$$

in which t_1 and t_2 are end points of the correlation window and L is the lag applied to trace 2. Trace 2 is then shifted by an amount L_m which produces the largest value of $X_L(t)$. This method of aligning traces is not very robust but works well if there is a strong common signal such as that of figure 3.5.

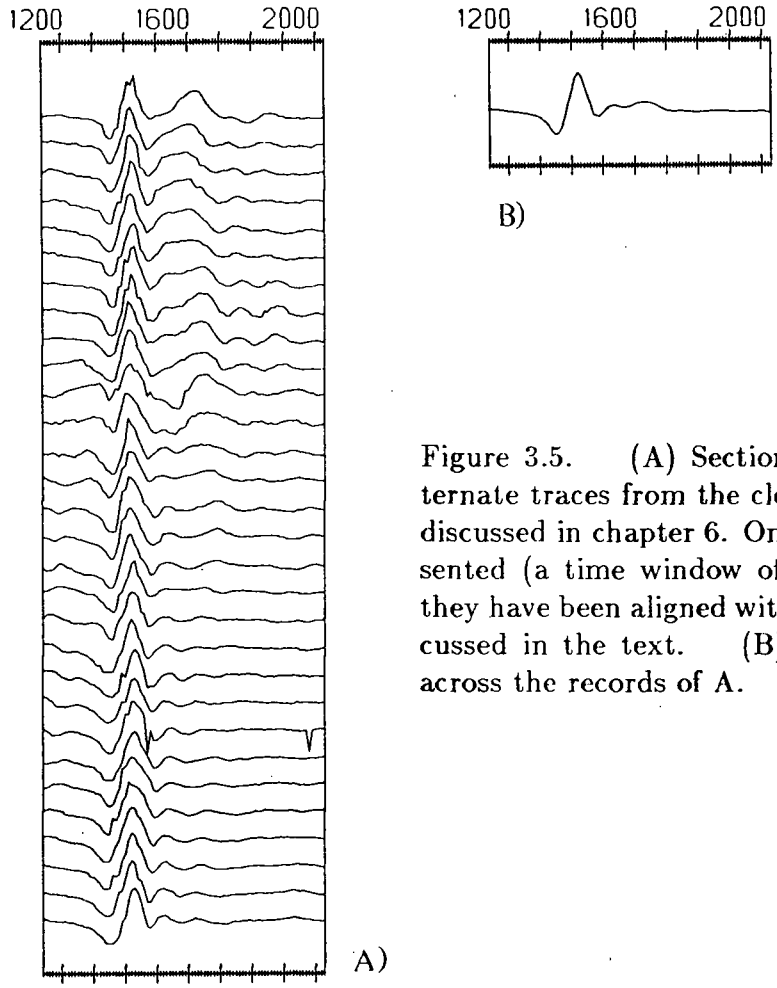

Figure 3.5. (A) Section consisting of alternate traces from the close-spacing survey discussed in chapter 6. Only the echo is presented (a time window of 90 samples) and they have been aligned with the program discussed in the text. (B) The mean stack across the records of A.

Now with the section of aligned traces, an average trace can be calculated using equation 3.6,

$$\overline{x}(t) = \frac{1}{N} \sum_{i=1}^{N} x_i(t) \tag{3.6}$$

where $\overline{x}(t)$ is the average trace and N is the number of traces. As an example, figure 3.5a shows an aligned portion of data. Equation 3.6 was applied with $N = 30$ traces and time going from 1.14 μs to 2.03 μs (*i.e.* 90 samples were used) to produce the trace of figure 3.5b. This average record could be used in comparison with modelling experiments (using a correct input wavelet $E_0(\omega)$) to estimate bulk properties that apply across the entire section. But we are still unable to interpret features that appear to vary across the

section. In this example the trailing (right hand) edges may reveal spatial variations in subglacial properties, and in other cases, englacial features or temporal changes of glacial or subglacial properties may be of interest. To facilitate the interpretation of such subtle echo features, the multichannel Karhunen-Loève transform (KLT) has been employed, the rudiments of which will now be discussed.

3.3.2 Principal Component Decomposition

The goal is to differentiate between signal components that are coherent from trace to trace, and components that are more variable. The multichannel Karhunen-Loève transform (KLT) does this by converting a set of n real data signals $x_i(t)$ $i = 1, \ldots, n$ into an alternate set $\psi_i(t)$ $i = 1, \ldots, n$. The conversion is optimal in the sense that the resulting $\psi_i(t)$ are orthogonal and are arranged in order of decreasing energy content, and the greatest possible amount of coherent information is packed into the smallest possible number of vectors $\psi_i(t)$. The transform can be written as

$$\psi_j(t) = \sum_{i=1}^{n} a_{ij} x_i(t), \qquad j = 1, \ldots, n \tag{3.7}$$

and its inverse, or the reconstruction of the data using the $\psi_i(t)$, as

$$x_i(t) = \sum_{j=1}^{n} b_{ij} \psi_j(t), \qquad i = 1, \ldots, n \tag{3.8}$$

which are from Jones (1985: ch. 2). Both transformation matrices A (with elements a_{ij}) and B (with elements b_{ij}) can be shown to be the eigenvector matrix R derived from the covariance matrix of the input data. The derivation of this result is carried out by first defining a truncated reconstruction of the data $\tilde{x}_i(t)$ using less than all the $\psi_i(t)$. The square of the difference, or truncation error, between $x_i(t)$ and $\tilde{x}_i(t)$ is then minimized

by setting the partial derivatives of this difference with respect to a_{ij} and b_{ij} to zero. A pair of equations is obtained in which the covariance matrix of the data $\Gamma = XX^T$ appears along with A, A^T, B, and B^T. Manipulation of these equations shows how $A = B = R$ if the truncation error is to be minimized. So the KLT is carried out by first forming the covariance matrix Γ and then decomposing it into its eigenvector matrix R and the corresponding diagonal eigenvalue matrix Λ. In other words, $\Gamma = R\Lambda R^T$. Then the multichannel KLT is written as the pair of equations

$$\Psi = R^T X \tag{3.9}$$

$$X = R\Psi \ . \tag{3.10}$$

The columns of R are the eigenvectors of Γ, the rows of X represent discretized versions of the data traces and the rows of Ψ are known as the principal component vectors of the transformation.

The interactive program I have written to perform the KLT on subsets of real data (up to 100 traces with up to 100 points each) includes the following functions: (i) parameters such as the number of traces, position and length of the time window along the trace and output format can be selected; (ii) a mean stack can be calculated (as in figure 3.5b); (iii) eigenvectors and eigenvalues of the correlation matrix can be either listed or plotted graphically; (iv) any number of principal components (p.c.'s) can be calculated and plotted if required; (v) any subset of these p.c.'s can be used to reconstruct the data. Making each step interactive ensures economic use of computer time by, for example, limiting the number of principal components generated to only those required. Figure

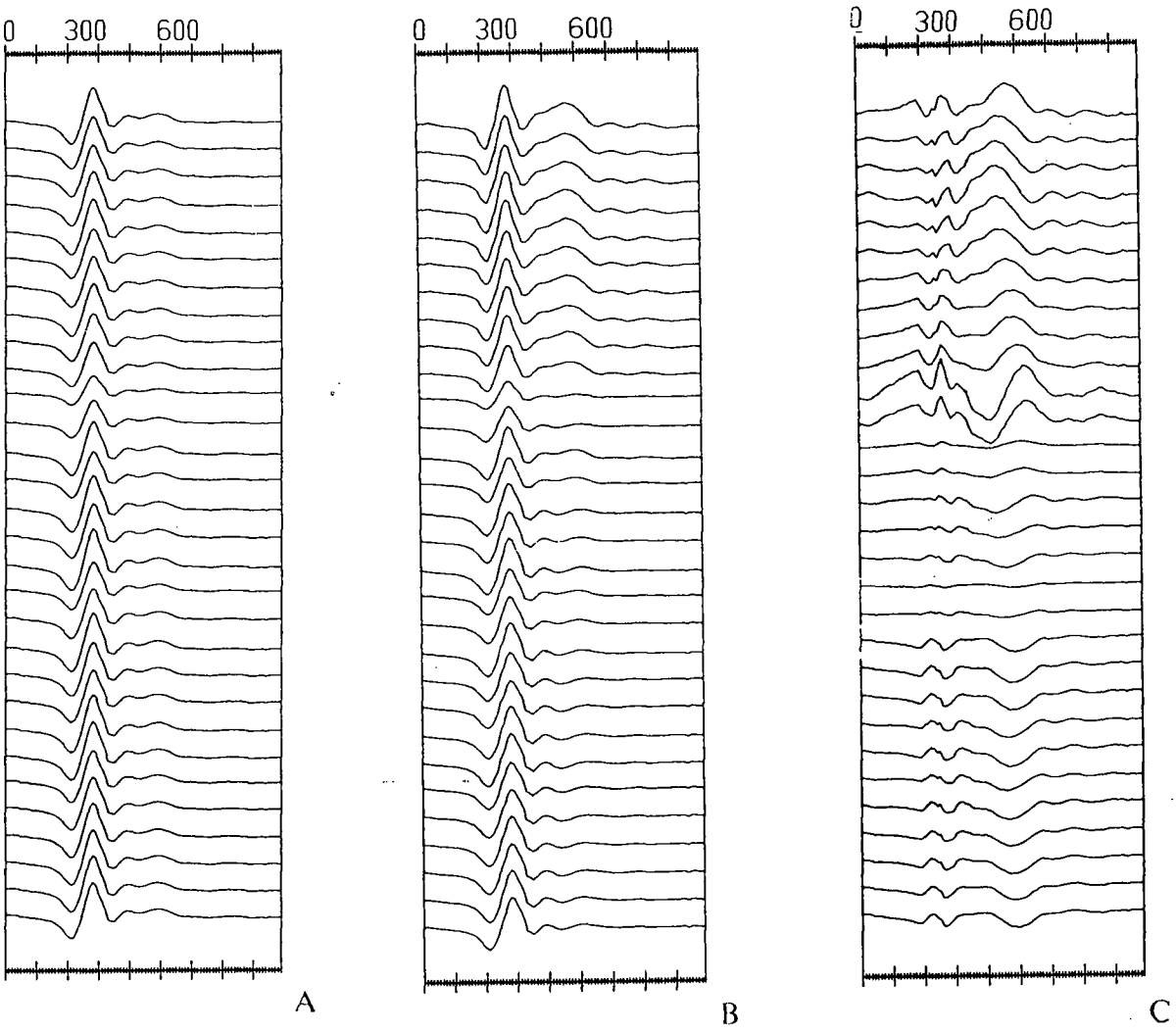

Figure 3.6. Data from figure 3.5a after reconstruction with only a few of the principal components derived with the Karhunen-Loève transform. (A) Reconstruction with only the first principal component. (B) Reconstruction with the first and second principal components. (C) Partial misfit reconstruction with the second and third principal components.

3.5 was generated with this program and figure 3.6 illustrates the use of the KLT on the same data set.

Some insight can be gained into how the KLT works by comparing figure 3.6 to the original data and corresponding mean stack. When only the first p.c. (calculated using equation 3.9) is used in equation 3.10, the resulting reconstructed traces will only contain information that is coherent across all traces. Such a reconstruction is not generally very useful but is given in figure 3.6a to illustrate that, as expected, each new trace is very

similar to the mean stack of figure 3.5b. Less coherent information is retained in the lower order principal components. A reconstruction which uses both the first and second principal components (figure 3.6b) includes some of the trailing edge features that are visible but confused in the raw data of figure 3.5a. Variations from trace to trace can be further emphasized by reconstructing traces without the most coherent information. For example, figure 3.6c was generated by using only p.c.'s two and three. Such misfit reconstructions also serve to emphasize particularly anomalous or noisy records such as traces 12 and 14.

The eigenvectors and eigenvalues of the correlation matrix can also be of use. Inserting the relation $XX^T = R\Lambda R^T$ into equation 3.10 shows that $\Lambda = \Psi\Psi^T$. In other words, Λ is the covariance matrix of Ψ, so the eigenvalue λ_i may be viewed as a measure of the energy content of the corresponding principal component $\psi_i(t)$. The sum $E = \sum_j \lambda_j$ represents 100% of the energy in the data so the amount of energy represented by each individual p.c. can be found from $e_j = \lambda_j / E$. These can be used to determine how many components would be needed if a reconstruction containing a certain percentage of total energy is required, to emphasize either coherent energy or incoherent energy.

A further application of the eigenvalues involves using their ratios to make quantitative assessments of coherency or similarity. For example, the so-called modified eigenvalue ratio, EVR, discussed by Jones (1985)

$$\mathrm{EVR} = \frac{\sum_{j=1}^{m} \lambda_j}{\sum_{j=m+1}^{n} \lambda_j} \tag{3.11}$$

will be large for a record set with similar signals (since most of the energy will be packed into the first few p.c.'s) and will be smaller for a set of dissimilar signals. Such a similarity

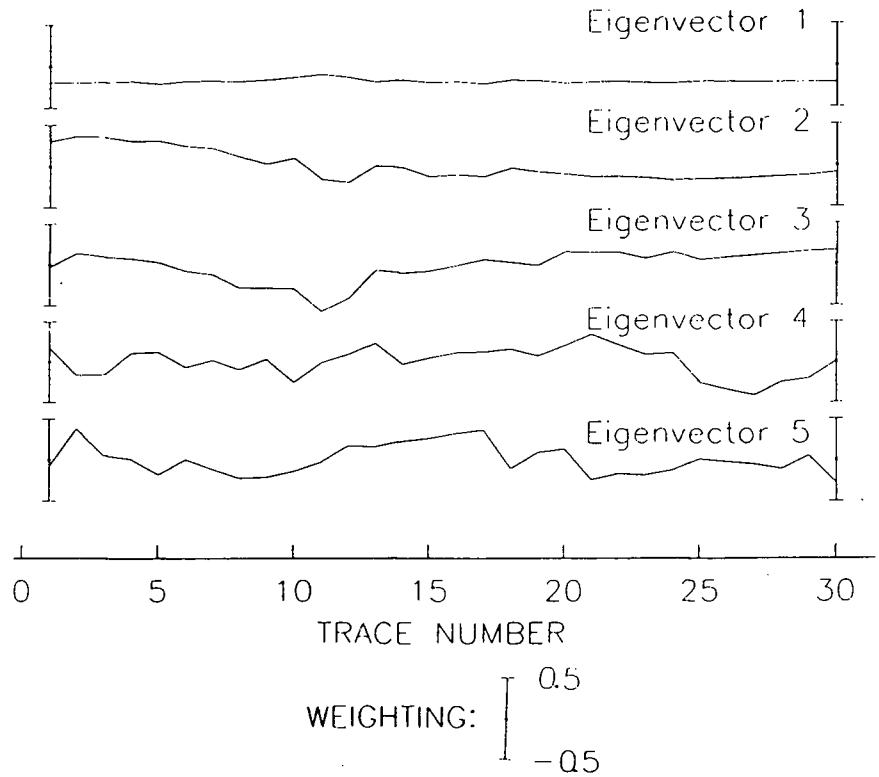

Figure 3.7. The first five eigenvectors found using equation 3.9 on a slightly smoothed version of the data in figure 3.5a. "Weighting" represents the weight of a particular trace's contribution to the p.c. corresponding to the eigenvector number. If a cluster of traces have similar weights for a particular p.c. then those traces have similar components at energy levels represented by corresponding eigenvalues.

measure could be used in various forms of cluster analysis to compare features exhibited by separate sets of records.

The eigenvectors of Γ, noted above to be the rows of the matrix R, can also be of use. If r_{ij} is the element in the i^{th} row and j^{th} column of R, it can be considered as a measure of the contribution of the i^{th} trace to the j^{th} principal component. In other words, it indicates how much of the i^{th} trace is projected onto the j^{th} principal component. A measure of the similarity between two traces can be found by calculating the square of the difference between projections of the two traces onto a given set of principal components.

Alternatively, the eigenvectors could be plotted to graphically depict the weight of each trace's contribution to a given p.c. Figure 3.7 is a plot of the first five rows of Ψ constructed from a slightly smoothed version of the data in figure 3.5a. The smoothing reduced the worst of the random noise by low pass filtering with a cutoff around 35 MHz. (The software described by Prager (1983) was used to perform this task.) The first eigenvector shows that most traces contribute similarly to the first p.c.; this is because the traces have a strong common signal. The second eigenvector shows that traces 1 through 10 are similar and traces 20 through 30 are similar. Lower order vectors show more random contributions from each trace, reflecting the randomness of lower energy components of the signals.

The method of KLT can be further refined to involve the use of complex data so that phase changes are incorporated into all applications. In this way greater compression is possible, frequency domain data can be dealt with directly, and even residual statics can, within limits, be accommodated. Jones (1985) shows how, for Ricker wavelets, time shifts of up to $t_s \leq 0.4\omega_m$ (refer to equation 3.4) can be accommodated for using phase shifts. The current work has not used the more expensive complex KLT because the data have large timing anomalies (see chapter 5) and have required alignment. Such an unreliable timing reference makes small-scale phase information difficult to extract and interpret.

3.4 CONCLUSIONS

This chapter has been concerned mainly with placing limits on how much can be interpreted from impulse radar echoes from a glacier bed. Two analytical approaches have been considered; the first was based on modelling electromagnetic pulse propagation and reflection as a filtering process and the second was aimed at enhancing field data. Modelling experiments using Ricker wavelets showed that some glaciological properties

should be easily determinable, such as whether there is a frozen or wet bed, while other properties, such as whether basal layers exist, will be harder to define accurately using radar data alone. Enhancement using p.c. decomposition was shown to have good potential for emphasizing data characteristics that would otherwise be obscured by strong common components or noise.

The remaining chapters of this thesis will examine field data in the light of these considerations and the methods will be applied with a view to making practical glaciological interpretations.

CHAPTER IV

INSTRUMENTATION

4.1 INTRODUCTION

The original requirments for the UBC portable impulse radar were that it be capable of generating very short duration signals centred at a frequency of a few megahertz, and that it be able to record echoes with a depth precision of 1 m and a maximum penetration depth of a few hundred metres. It was desirable to obtain records which could be processed in the lab, or even in the field, using signal enhancement techniques similar to those of seismology. Problems of practical field operations were also addressed. Small size, light weight (and hence low power requirements), and automatic operations are all important if the difficulties of working on temperate glaciers are to be minimized.

These considerations resulted in the instrument illustrated in figure 4.1. It consists of a transmitter and an antenna which together emit a pulse of about 20 MHz bandwidth with a peak at about 8 MHz, and a digitizing receiver which records the electric field strength at its antenna for 10 μs after emission of the pulse. From a system point of view (figure 4.2), the instrument is organized around a microprocessor which, in response to commands from the operator, will initialize the acquisition of records and handle the operations of identifying, storing, retrieving and displaying them. The following more detailed discussion considers each of the four major components separately: the transmitter; the antennas; the receiver and digitizing circuitry; and the microprocessor, software, and peripheral functions. Finally, I will comment on the instrument's physical configuration as it relates to actual field operations.

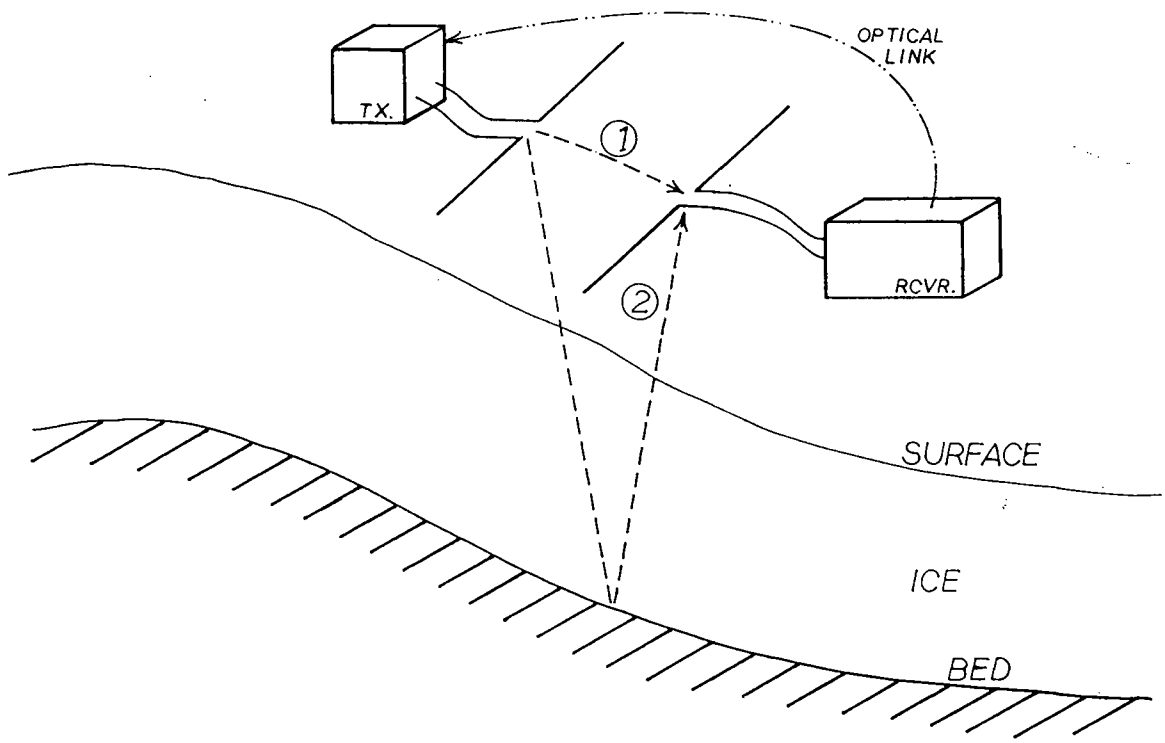

Figure 4.1. Field configuration of the UBC impulse radar instrument. Transmitter (TX) is triggered by the receiver (RCVR) via the optical cable. Energy path 1 is known as the surface or direct arrival; energy path 2 is the glacier bed echo.

4.2 TRANSMITTER

Most impulse radar systems discussed in the literature (*e.g.* Watts and England, 1976; Sverrisson and others, 1980; Morey, 1974; Sellman and others, 1984) generate the required impulse of electromagnetic energy by delivering a single-phase voltage pulse to the terminals of an antenna designed to radiate over a broad band of frequencies. The voltage pulse is usually generated by using a solid state switch to connect as nearly instantaneously as possible a charged capacitor directly to the antenna. Watts and Wright (1981) describe a pulse generator of this type that uses for the high speed switch a set of bipolar transistors operating in the avalanche mode. Such a design has many advantages. It is simple, inexpensive, has a voltage rise time of a few nanoseconds, can develop a few kilowatts with a single transistor and can run either at a fixed rate as a relaxation oscillator or as a triggerable pulse generator. A conceptually similar system can be built using a

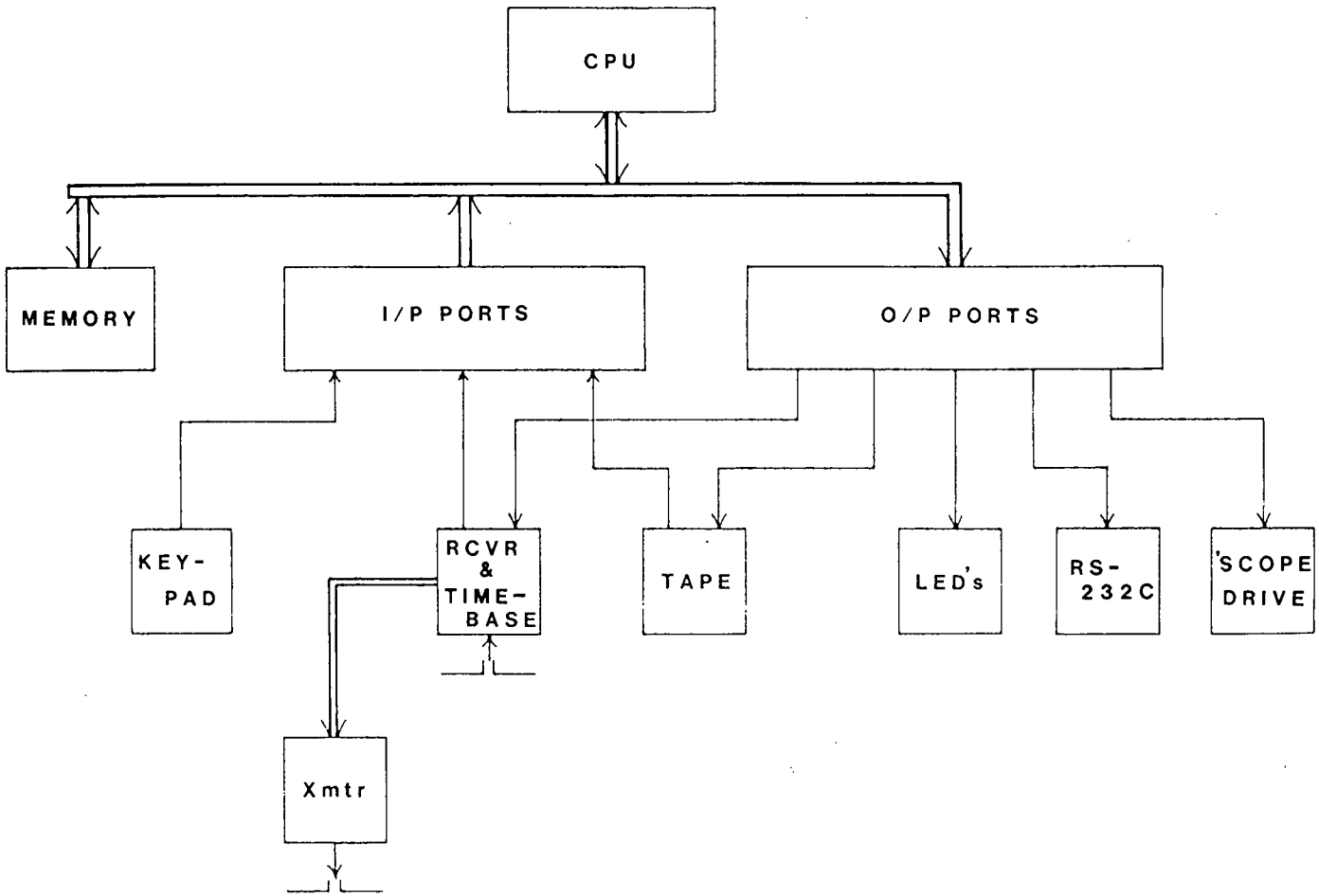

Figure 4.2. System block diagram. Components are discussed in the text.

silicon-controlled rectifier (SCR) as the switch (Sverrisson and others, 1980). Rise times are somewhat slower but SCRs are more efficient than avalanche transistors, eliminating the need for heat dissipation and reducing the total power requirements. This is the type of transmitter designed for the UBC impulse radar instrument.

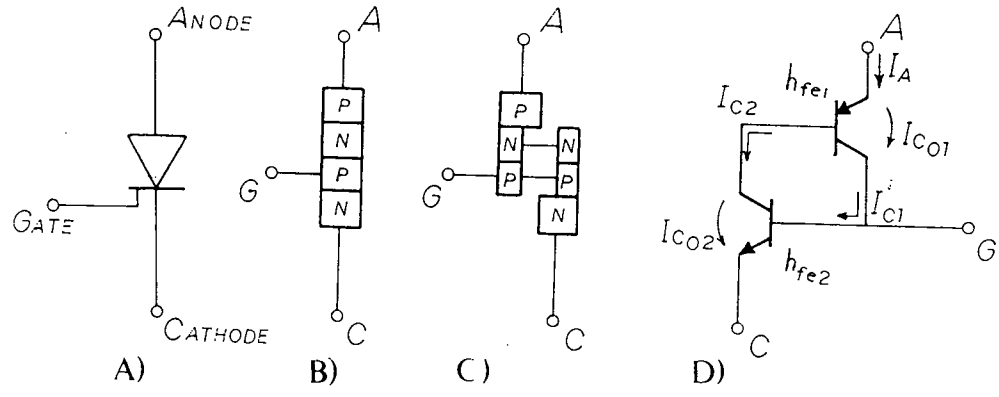

Figure 4.3 Conceptual operation of SCR switches. See text for details. (A) SCR symbol. (B) SCR construction. (C) SCR function. (D) SCR functional diagram. I_{co} is leakage current. If I_c and I_b represent collector and base currents, then h_{fe} is forward gain such that $I_c = I_{co} + h_{fe}(I_{co} + I_b)$.

It is critical to the generation of useful pulses that the voltage step be as fast as possible, so a discussion of SCR switches is in order. Referring to figure 4.3, an SCR can be viewed as a pair of transistors in series so that the anode current I_A will depend on the individual current gains, h_{fe1} and h_{fe2}, and collector-emitter leakage currents, I_{co1} and I_{co2}, according to equation 4.1 (Gutzwiller, 1967):

$$I_A = \frac{(1 + h_{fe1})(1 + h_{fe2})(I_{co1} + I_{co2})}{1 - h_{fe1}h_{fe2}} \quad . \tag{4.1}$$

This equation results from algebraic manipulation of the following three equations, re-

lating currents I_A, I_{co1} and I_{co2}:

$$I_A = I_{c1} + I_{b1},$$

$$I_{c1} = I_{co1} + h_{fe1}(I_{co1} + I_{c2}),$$

$$I_{b1} = I_{c2} = I_{co2} + h_{fe2}(I_{co2} + I_{c1}).$$

An SCR is in the forward blocking or *off* mode when the anode is at a positive voltage with respect to the cathode and the so called loop gain $G = h_{fe1}h_{fe2} \ll 1$. As G approaches 1, I_A increases, the second transistor applies a positive feedback current to the base of the first, and they both drive each other into saturation. This is the *on* condition in which the anode and cathode are virtually short-circuited. This avalanching or switching on can best be initiated by increasing the leakage currents because h_{fe} is directly proportional to emitter current. Current leakage between anode and cathode is dependent on anode-to-cathode voltage drop, the rate of change of this voltage (due to device capacitance), and temperature (due to carrier mobility in semi-conductors). But the most straightforward method of initiating avalanching is to inject a small charge into one of the two internal layers; hence the provision of a "gate" terminal on the internal P (conventional SCRs) or N layer (complementary SCRs). Once in the *on* mode, the SCR will revert to its *off* state either if I_A drops below the device's so called "holding current" (regardless of gate current), or if I_A drops below the "latching" current after the gate current has been removed. These characteristics are specified by the manufacturer.

The radar transmitter consists of two SCRs arranged in a push-pull configuration. When they are simultaneously triggered by a current pulse at their gates, they discharge a pair of capacitors into the antenna such that one arm of the dipole receives a large positive pulse and the other arm receives a large negative pulse. The resultant 1200 V pulse at the antenna terminals has an exponential edge which reaches a rate of change

of $10.2\,\mathrm{V\,ns^{-1}}$ over its latter half (figure 4.4). Before switching, the SCRs are holding off approximately 800 V on each anode and after triggering, the anode voltage drops rapidly to a point where I_A falls below the latching current. Then the SCRs revert to the *off* condition and the capacitors can recharge in time for the next trigger signal.

Figure 4.5 is a simplified schematic diagram to which the following practical notes refer (see the appendices for the complete schematic). Capacitor C_1 was chosen to be $0.01\,\mu\mathrm{F}$ and R_c limits the charging rate to suit the small DC-to-DC converter used as a high voltage supply (Venus Scientific, Inc. model C8T; converts 12 V DC at 190 ma to 800 V DC). Resistors, R_D, are required to reference the circuit to ground and to provide a slow discharge path for the current which was dumped into the antenna arms. These are discussed in section 4.3. The trigger generator converts the optical trigger signal into a current pulse suitable for forcing the SCRs into an avalanching condition. A pulse transformer with dual secondary windings ensures simultaneous timing of the two triggers and resistors R_{G1} and R_{G2} are selected so that trigger currents are appropriate for the individual characteristics of each SCR. In this way avalanche breakdown of both SCRs can be tuned to occur at exactly the same time as long as ambient conditions are identical, a condition ensured by fixing the two devices close to each other on the same heat sink. During field trials it was found that overall timing is temperature-dependent such that lower ambient temperatures result in greater delays between arrival of the trigger signal and emission of the pulse. This is because a greater charge (*i.e.* a longer current pulse) is required to initiate avalanching when the semiconductor junctions are at a lower temperature.

4.3 ANTENNAS

The next step is to consider how the pulse that is applied to the antenna (illustrated in the oscilloscope photographs of figure 4.4) is radiated as a short electromagnetic wavelet.

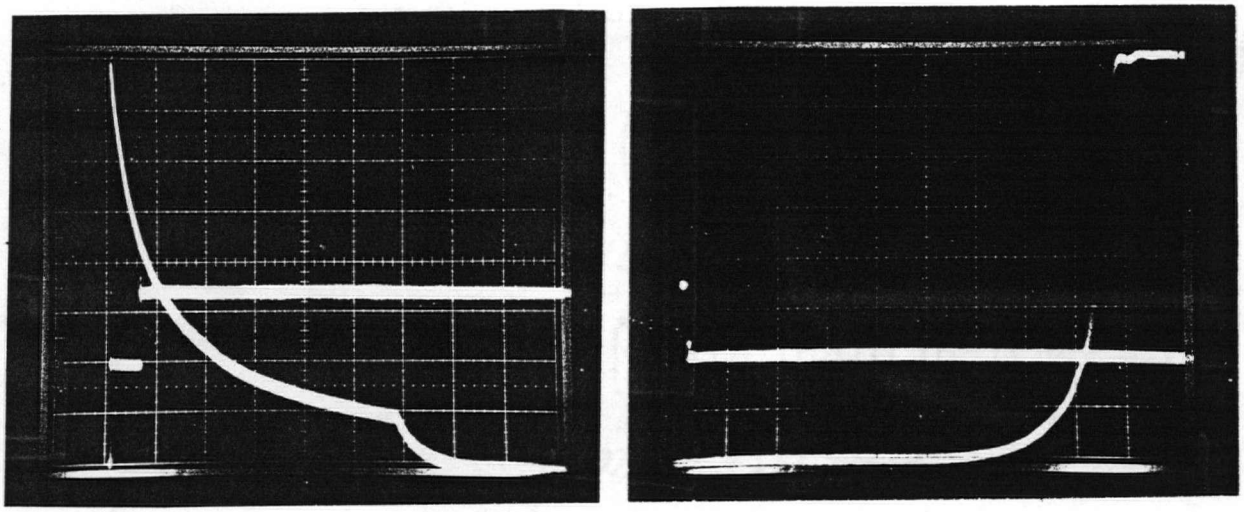

A) B)

Figure 4.4. Oscilloscope photographs of pulse generator waveforms. (A) Shows the complete voltage pulse at the antenna terminals. The small, negative, square pulse is the trigger command arriving from the receiving unit. Scale: 150 V per vertical division for the spike, 1.5 V per vertical division for trigger pulse, 20 μs per horizontal division for both. Note that both traces start at the second division. (B) Same as A in all respects except that the time axis is 0.1 μs per division. This emphasizes the approximately 0.8 μs delay between arrival of the trigger signal and the actual switching of the SCRs. Colder ambient temperatures increase this delay. SCR switching results in an exponential rise in voltage across the antenna terminals. This can be considered as a good step function because the trailing edge visible in photo A is very long relative to the rise time exhibited by photo B.

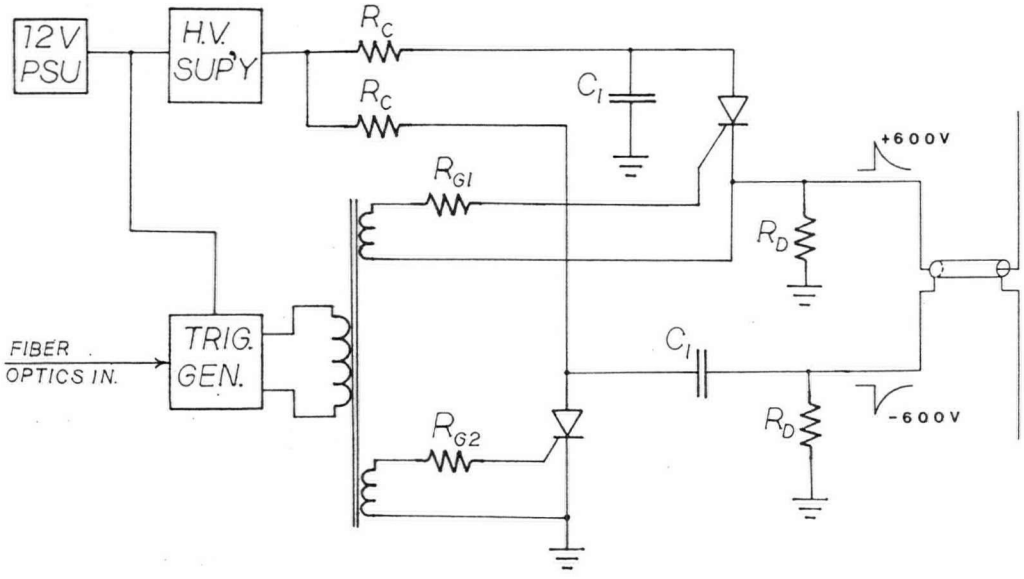

Figure 4.5. Simplified circuit diagram of the transmitter referred to in the discussion of transmitter operation.

A very broad bandwidth antenna (one with good transient performance) is required to damp out natural resonances. A dipole antenna with this characteristic is shown by Wu and King (1965) and by Rose and Vickers (1974) to consist of dipole arms for which internal resistance increases towards the outside ends. The effect is to reduce the current towards zero as the pulse travels outward along the dipole arms, thus reducing reflections at the ends of the arms and preventing the current distribution on the antenna from being a standing wave. The internal resistance profile that optimizes the impulse response (regardless of efficiency) can be found using relations derived by Wu and King (1965) (with corrections by Shen and King (1965)). They show that at a position x from the centre of the dipole, the internal impedance $Z(x)$ for which a pure outward travelling wave exists on an antenna arm of length h is given by

$$Z(x) = \frac{\xi\psi}{2\pi(h-x)} = \frac{R_0}{h-x} \; . \tag{4.2}$$

The term ξ is the intrinsic impedance of the medium and ψ is the ratio

$$\psi = \frac{\text{vector potential on the antenna surface}}{\text{current along the antenna}}$$

at the point where the current is a maximum. If ψ is considered as virtually constant with respect to x, and the antenna radius a is small, ie. $a \ll h$, then the magnitude of ψ is given by

$$|\psi| \cong \left| 2\left(\sinh^{-1}\frac{h}{a} - C(2ka, 2kh)\right) + j\left[2S(2ka, 2kh) + \frac{1}{kh}(1 - e^{-j2kh})\right]\right| \tag{4.3}$$

(Wu and King, 1965 (equation 29), and Shen and King, 1965) where, for the antenna used on Trapridge Glacier: $h = 5.0\,\text{m}$ is the length of each dipole arm; $a = 0.5\,\text{mm}$ is

the radius of the antenna wire; $k = \omega/v$ is the wave number; $hk = \pi/2$ since this is a half-wave dipole; $h/a = 1 \times 10^4$; and $2ka = \pi \times 10^{-4}$. Also,

$$C(b,x) \approx \int_0^x \frac{1-\cos t}{t}\,dt \qquad \text{if } b \ll x$$

$$S(b,x) \approx \int_0^x \frac{\sin t}{t}\,dt \qquad \text{if } b \ll x\ .$$

These so-called Cosine and Sine integrals are handled as per Abramowitz and Stegun (1972) and ψ is found to be $|\psi| = |16.5 - j2.43| = 16.68$. Concerning the intrinsic impedance $\xi = \sqrt{\mu/\epsilon}$, the method of Sverrisson and others (1980) is followed, whereby the permittivity of the medium in which the antenna operates is found by using

$$\epsilon = \epsilon_0\epsilon_r = \epsilon_0\sqrt{\epsilon_{\text{ice}}\epsilon_{\text{air}}} = 1.78\epsilon_0$$

Magnetic permeability is that of nonmagnetic materials ($\mu = \mu_0$), so $\xi = \sqrt{\mu_0/1.78\epsilon_0} = 281.1$ and equation 4.2 yields $Z(x) = 748.8/(h-x)$. For this optimally damped antenna, Shen and King (1965) show that the efficiency is only around 8% or 9%. Therefore R_0 must be reduced and a compromise found between sufficient damping and adequate radiated energy for sounding. In general, R_0 will not be the same for different antenna lengths, nor will a single R_0 be optimum for a given antenna on different glaciers. Only rough estimates can be made unless optimization is carried out in the field where ice depth, temperature, scattering properties, and instrumentation will all contribute to system performance. The length h determines the centre frequency of the pulse emitted and is also chosen as a compromise between resolution and power loss due to scattering. In the present case, the resistive loading was approximated by inserting fixed resistors

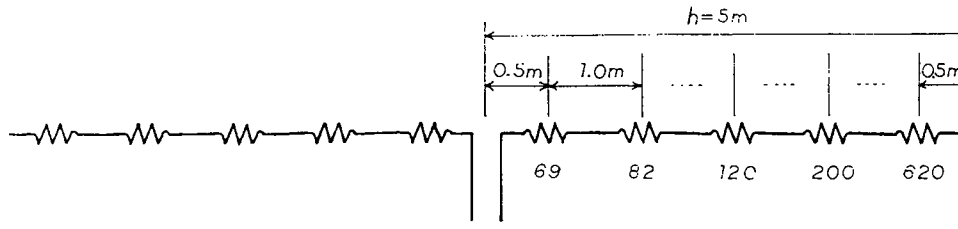

Figure 4.6 Diagram of antennas used on Trapridge Glacier. Resistances are in ohms and the two sides are symmetrical.

of values found using equation 4.2 with $R_0 = 300\,\Omega$, and the resulting antenna used on Trapridge Glacier is shown in figure 4.6.

The actual wavelet emitted when the antenna in figure 4.6 is excited by the input of figure 4.4 is difficult to estimate analytically because the current distribution on an antenna resting on the air/ice interface is not accurately known. However, the situation can be considered qualitatively. Our damped antenna is modelled as a resistor in series with a capacitor (Wu and King, 1965). Therefore a step voltage applied to the driving point will result in a "one-lobed" current pulse; that is, current will be in one direction and will first rise and then fall. Now, it is fundamental to the theory of electromagnetic radiation (Jordan and Balmain, 1968, p.319) that the vector potential in the far field of an antenna is proportional to the first time derivative of the current in the antenna. By the reciprocity theorem of antennas (Jordan and Balmain, 1968, p.345), the voltage on a receiving antenna is related in a similar way to the far field vector potential, so the waveform recorded by the receiver will look like the second time derivative of the original current pulse. Therefore, if the pulse generator can impress a step voltage onto the antenna, the best possible echo will be a three-lobed waveform.

The frequency emitted depends on the antenna length. Since it behaves approximately as a half wave dipole, it is tuned close to a frequency with wavelength $\lambda \approx 2h$; that is to a frequency $f_c \approx v/2h$ where $v = c/\sqrt{\epsilon_{\text{ice}}}$. Consequently, wavelet spectra are expected to have a peak around $f_c = c/(\sqrt{3.18} \times 2h) = 8.4\,\text{MHz}$. Considering that this is a damped, not a true dipole antenna, that *effective* antenna lengths have not been

calculated, that they rest on an interface of dielectrics, and that echoing and propagation are dispersive, the spectra of wavelets received agree reasonably well with this estimate (figure 3.2).

Rapid discharge of the current in the antenna would produce negative currents resulting in secondary emissions that would degrade the waveform. This is why the resistors R_D in figure 4.5 are large, resulting in the long trailing edge of the pulse seen in figure 4.4, and hence causing negligible reverse antenna currents. (Recall that current in a capacitor (*i.e.* in the antenna) is proportional to dV/dt.)

4.4 RECEIVER

The receiver's task is to amplify the signal on the receiving antenna and to digitize it at an effective rate of 100 MHz without the high cost, large power requirements and low resolution of most real-time "flash" digitizers. The solution is to use the sampling time base method, and the circuit (see figure 4.7 for a block diagram) is a modification of one described by Narod and Clarke (1983). This method uses a high-speed sample-and-hold (S/H) device to grab one sample of the signal and hold it for digitizing. The subsequent sample is obtained by repeating the echo and moving the S/H 10 ns further along the signal. In order to gather a complete record, this process is repeated 1024 times until 10 μs of data has been collected.

Precise timing is obtained by comparing an accurate linear voltage ramp to a reference voltage. If the reference voltage is changed, the time at which both signals are identical will change by an amount proportional to the ramp height, ramp duration and change in reference voltage. In the UBC radar, successive sample positions are obtained by lowering the reference by 10 mV. The ramp voltage runs from 10.00 V to 0.00 V over a period of 10 μs so, for each new sample, the time at which the two voltages are equal is moved forward by $(10\,\text{mV}/10\,\text{V}) \times 10\,\mu\text{s} = 10\,\text{ns}$. The transmitter is triggered simultaneously

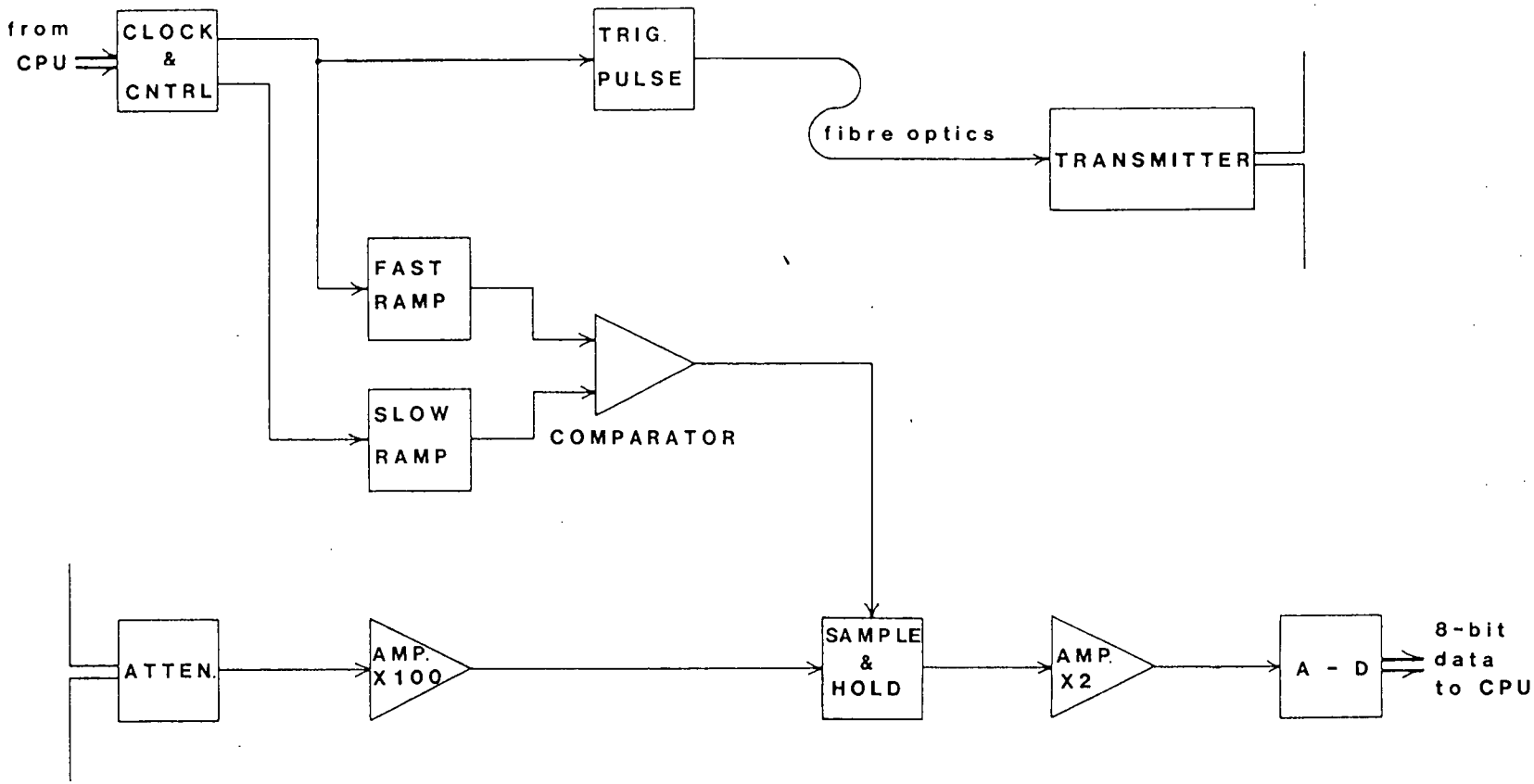

Figure 4.7. Receiver block diagram. Components are discussed in the text.

with the start of the ramp, so echoes returning within 10 μs will be recorded; in other words, the maximum depth observable will be $d = (v \times 10\,\mu\text{s})/2 = 840\,\text{m}$. This complex procedure is required because our low power, 12-bit analogue-to-digital converter (ADC) takes 35 μs to perform the conversion and the resulting number must then be properly stored. In fact, the rate at which samples can be gathered is further limited by the maximum pulse repetition rate of the transmitter. This is 250 Hz because capacitors C_1 of figure 4.5 take 4 ms to recharge. Therefore, since the 1024 samples each require one complete pulse, gathering one record takes 4.1 seconds.

Details of the electronics will not be presented but some notes concerning the blocks in figure 4.7 are worthwhile. Clocking and control are based on a 1 MHz crystal clock, with divider circuits generating the required timing pulses. The transmitter is triggered synchronously with the fast ramp which is generated by an operational amplifier configured as a precision integrator. The slow ramp is the variable reference voltage referred to above. It is generated by clocking a 10-bit binary counter once for each sample and converting the count into an accurate voltage level with a digital-to-analogue converter. The comparator is a precision circuit which produces a 50 ns pulse when one input voltage passes from greater than to less than the other. The S/H device starts tracking the input signal on the rising edge of this pulse and the trailing edge signals the S/H to hold the input level for conversion into a digital number by the ADC.

The input stage is a five-transistor wide band amplifier preceded by a variable attenuator. Traditionally, the input impedance of a receiver is designed to match that of the receiving antenna (which in our case is identical to the transmitter antenna). This maximizes the transfer of power from antenna to receiver and prevents the antenna from reradiating a portion of the signal. To date, however, most impulse radar work on glaciers has been carried out by simply plugging the receiving antenna into the high impedance input of an oscilloscope and photographing the trace triggered by the surface arrival.

Such mismatching can work for two reasons. First, the antenna itself is designed not to ring by including the damping resistors. Second, the low signal-to-noise ratio expected for severely mismatched systems is not important since local ambient radio frequency noise in mountain environments is usually very low. Given these considerations, it becomes desirable to have a receiver with a high input impedance because then the voltage on the antenna can be seen with a minimum of that signal being dropped across the input impedance. The UBC radar's receiver was not optimized in the prototype, but since the records obtained on Trapridge Glacier were entirely adequate, the system has not yet been improved.

4.5 COMPUTER, CONTROL AND DATA HANDLING

It has already been mentioned in the introduction that the instrument is under the control of a microprocessor. The computer is built with components of the COSMAC 1800 microcomputer system, manufactured by RCA (RCA, 1977) and consists of a CDP1802 central processing unit, 4 kbytes of read-only memory (containing the program), 1.25 kbytes of random-access memory (used as a data buffer), and input/output ports for communication with peripheral hardware. As figure 4.2 illustrates, these peripherals include: (i) a keypad with which the user enters commands and identifies records, (ii) an LED display to inform the user of the current system status, (iii) a digital cassette tape recorder for permanent data storage, (iv) an RS-232C interface for transferring data to other devices, (v) a digital-to-analogue converter for displaying a record on an oscilloscope, and (vi) the sampling time base receiver discussed previously.

The entire system is under software control and operates as follows (see the flow chart of figure 4.8). After initializing the registers, pointers and control lines (at power up or by pressing "reset"), the system rests idle until an instruction is keyed in on the hexpad. The sequence of keys is stored until the "enter" button is recognized, at

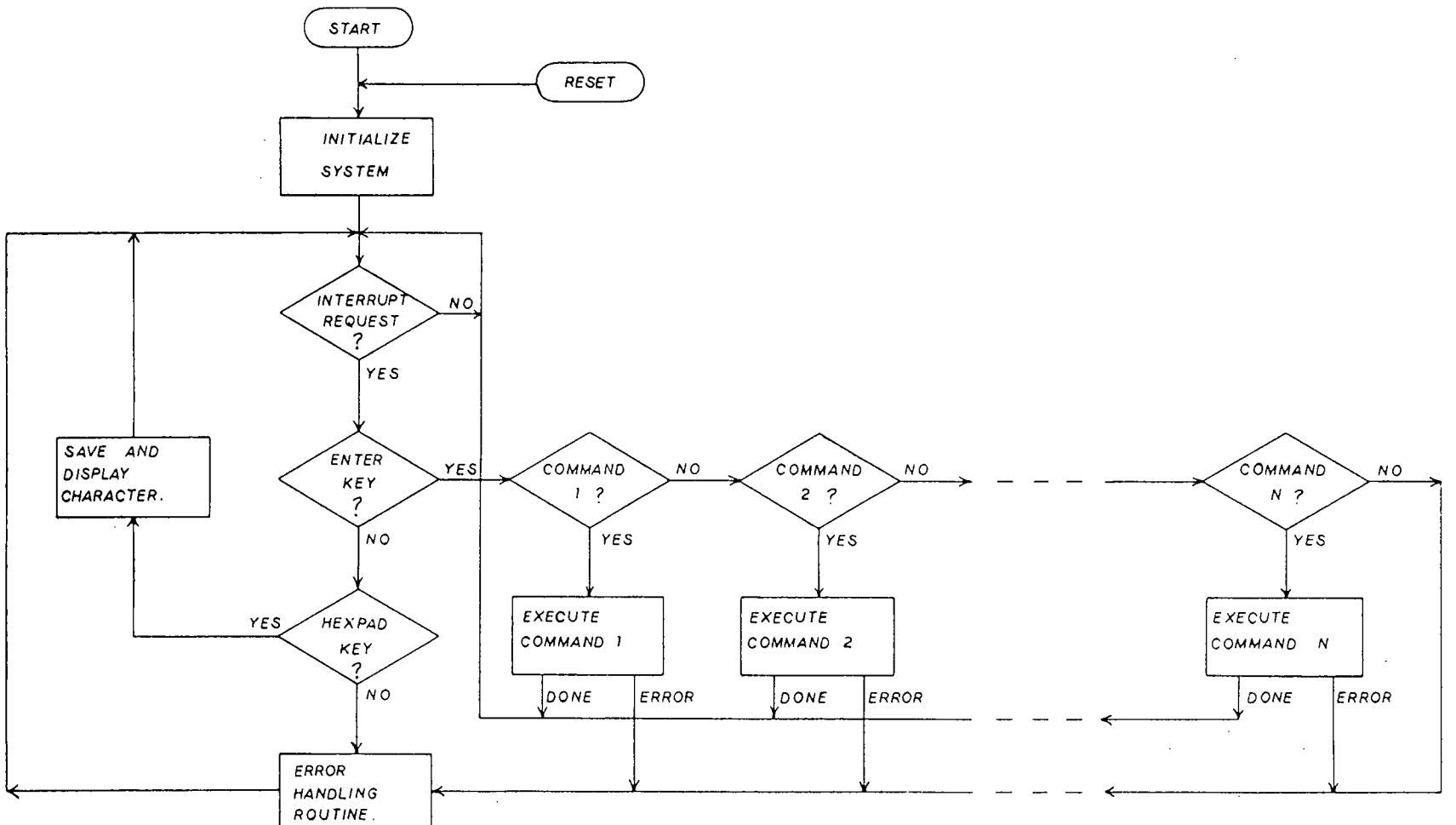

Figure 4.8 Simplified software flow chart. See the text for an explanation.

Table 4.1 System instructions

Fill data buffer with byte 'XX'	*A0XX*
Load forward write command	*A1*
Cassette rewind	*A2*
Write byte 'XX' onto cassette	*A3XX*
Load forward read (finds file gaps)	*A4*
Reverse one file	*A5*
Backspace and load forward to file gap	*A6*
Read one byte off cassette onto LED's	*A8*
List tape byte by byte on LED's	*A9*
Auto-acquisition every 'XX' minutes	*AFXX*
List current header buffer on LED's	*BC*
List first 'XX' bytes of data on LED's	*BDXX*
List current format block on LED's	*BF*
Initialize data cassette	*C1*
Gather a record and display on oscilloscope	*CD*
Dump header and data onto RS-232C	*DB*
Dump entire cassette onto RS-232C	*DC*
Display data buffer contents on oscilloscope	*DD*
Dump next file onto RS-232C	*DF*
Write LEOT mark (use with caution)	*F1*
Advance tape 'XX' files and read data	*FAXX*
Reverse tape 'XX' files and read data	*FBXX*
Display current file header	*FC*
Open new file and store current data	*FD*
Find file 'XX' and read it	*FFXX*

List of instructions currently available for controlling the radar. New instructions require additional software.

which point the sequence is decoded and the requested task initiated. These can be classified as data collection, display, record identification, storage and retrieval tasks, or as diagnostic functions; a complete list of instructions is given in table 4.1. Suitable status messages or requests for information are displayed on the 8-digit display and when a task is completed, the system either returns to its idle state or displays appropriate error messages. Records are gathered by the sampling time base asynchronously with respect to the computer. After the initial start command, transfers of data from the ADC to the buffer memory (one sample at a time) include two-way hand-shaking communication between the CPU and receiver. After a complete record has been collected, it can be

visually displayed by outputting pairs of numbers representing amplitude and sample number to the oscilloscope's Y and X channels respectively. This is done with two digital-to-analogue converters by the oscilloscope driver which outputs the complete record 25 times per second. This means that a small, low-cost, low-power oscilloscope can be used for inspecting results in the field; the Tektronix model 211 was used on Trapridge Glacier.

Data are stored permanently on cassette tapes as files of 1024 samples, each sample having 8-bit resolution. The system will also request identification information from the operator and attach this to each record as a header containing the time, date, location, gain, and record number. A maximum of 50 such records can be stored on standard digital data cassettes. The digital recorder/player and its control card are a commercial unit supplied by Memodyne Corporation (the model 333 "minicorder").

Data are recovered by reading the records off the cassette either individually by file number or sequentially to dump a complete tape. It can be released to another computing system through the on-board RS-232C serial interface. For the present, data is reformatted to make it compatible with the plotting and processing package that was designed for dealing with data produced by the UBC UHF radar system (Narod and Clarke, 1983). This package (Prager, 1983) performs such operations as plotting, smoothing, DC bias removal, signal differentiation, and time-dependent amplitude variation either on individual traces or on suites of traces. Additional subroutines were added specifically for impulse radar data. For example, instrument bias can be subtracted and traces can be shifted or truncated. Various other processing programs have also been written, including the alignment, spectral analysis, principal component decomposition and amplitude processing routines discussed elsewhere in this thesis.

4.6 FINAL COMMENTS

In order to facilitate field operations, the instrument is configured as two separate units; the first is the transmitter and the second contains all the remaining components. The transmitter trigger signal is sent from the receiver via an optical cable which electrically isolates the two units while maintaining reliable, uncomplicated operation. Identical antennas are used for transmitting and receiving so that they are interchangeble in the field. Dipole arms are 5 m long and are constructed as 1 m lengths of 18 AWG wire with loading resistors at their midpoints. These are installed in sections of plastic pipe so that the antennas are rugged, collapsible, and can have loading resistors or length varied conveniently in the field. Each unit requires a power supply capable of maintaining a minimum of 12 V. Twelve "D" size dry cells in series (18 V) are adequate to run the transmitter but the higher currents demanded by the cassette deck and high-speed circuitry in the receiver have been found to drain such a source too quickly. This is in spite of using CMOS technology for the digital circuits, as well as using software to power down the sampler when it is not being used. Lantern batteries or gel cells are more appropriate and automobile batteries were used when time-varying targets were being studied over long periods of time. These experiments use a software routine which will record echoes at regular intervals selectable in one-minute steps from 1 to 255 minutes. The entire system was configured to fit in a backpack for small-scale studies (see frontispiece) and was fitted into a rugged, waterproof case for more extended field work on Trapridge Glacier. These and other specifications of the impulse radar instrument are summarized in appendix 1.

CHAPTER V

FIELD WORK AND DATA CHARACTERISTICS

5.1 PRELIMINARY FIELD TRIALS

In this chapter, experiences gained in early trails will be briefly discussed, current field methods will be explained, and basic characteristics of signals obtained on Trapridge Glacier in July 1986 will be considered.

In July 1984 the first transmitter test was conducted on Trapridge Glacier by triggering the transmitter continuously and recording echoes on the screen of a high speed oscilloscope connected directly to the receiving antenna. A set of soundings down the centreline of the glacier was obtained and results were encouraging enough to continue the development of the digitizing receiver (see figure 5.1.).

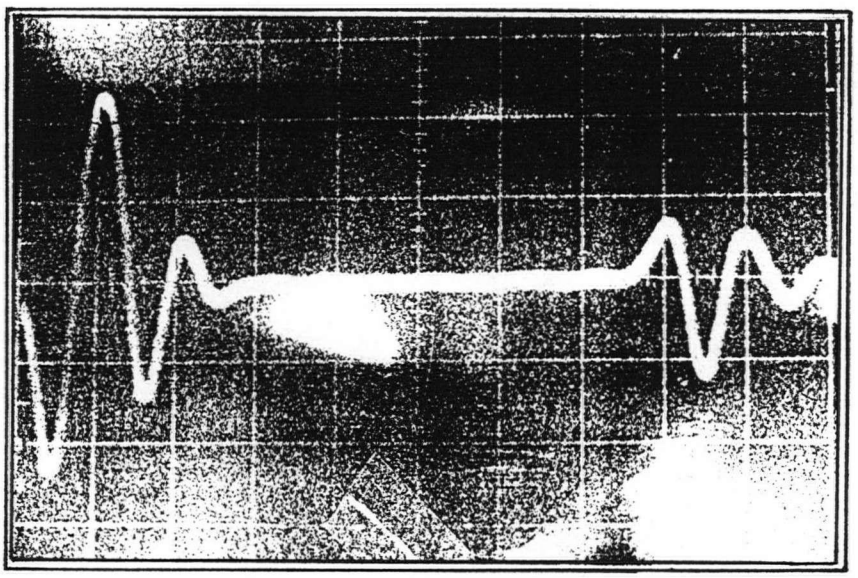

Figure 5.1 One sounding from the transmitter tests of July 1984. The array was similar to that used in more recent work except that no digitizing receiver was used. Horizontal scale is 0.1 μs per division and vertical scale is 50 mV per division.

The entire system was taken to Trapridge Glacier in July 1985, but poorly designed receiver electronics prevented any useful results from being obtained. These problems were corrected in time to take the system to Athabasca Glacier in the Canadian Rockies in November 1985. Unseasonably cold temperatures (between $-25°$ and $-40°$ C) prevented this prototype system from providing any data, but useful experience in cold temperature field operations was gained. The trip also prompted a laboratory assessment of the behavior of SCRs at low temperatures. The extended switch-on delay times discussed in section 4.2 were discovered by running the transmitter in a box cooled with dry ice. These and other temperature-dependent effects will be noted later when the three-day continuous survey is discussed.

In May 1986, the complete system was taken to Helm Glacier in Garibaldi Provincial Park near Vancouver for final system verification, and to assess the feasibility of using the equipment on very lightweight expeditions. Although the data obtained from this very warm, shallow glacier (less than 40 m deep according to Park personnel) were of marginal use, experience with the equipment resulted in further minor modifications (such as reconstruction of the antennas) which greatly simplified subsequent field operations. It was also found that two operators can handle enough gear to carry out three or four days of echo sounding without extra logistical support. The frontispiece illustrates how the system was deployed for this work.

5.2 FIELD OPERATIONS ON TRAPRIDGE GLACIER

Owing to the extensive amount of work planned for the 1986 field season, a more rugged and convenient configuration of the equipment was required than that used on Helm Glacier. Figure 5.2 illustrates how the transmitter, antennas and receiving unit (including receiver, monitoring oscilloscope and miscellaneous operating gear) were deployed so that the system was easily operated by one person on safe terrain.

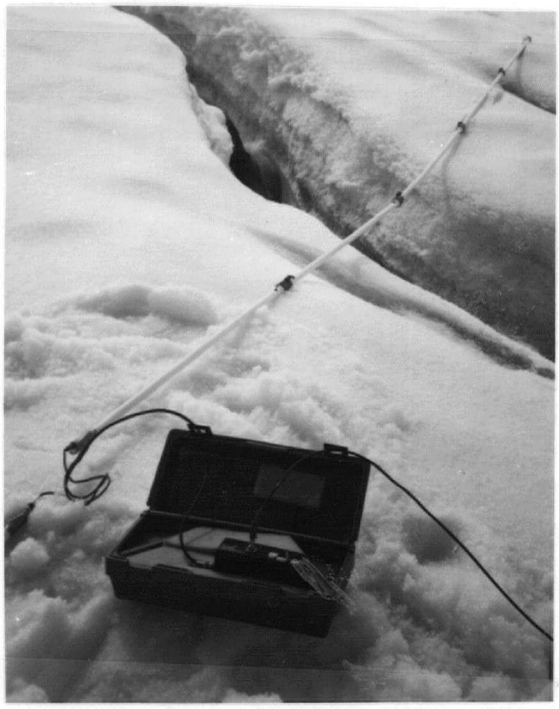

A.

B.

Figure 5.2 Equipment configuration as used on Trapridge Glacier, July 1986. (A) Transmitter installed in a small tool box; power supply consisting of twelve "D" size dry cells is included. Also note the modular construction of the antenna as described in section 4.2. (B) Receiver, monitoring oscilloscope, power supplies for both (dry cells for the oscilloscope and dry cells or external higher capacity batteries for the receiving unit) and miscellaneous equipment. The optical cable is visible in the upper left. The padded metal case is on a small sled.

In all cases, the sounding array was the same; antennas were placed 20 to 25 m apart and were perpendicular to the survey line. Other antenna polarizations were found to be inadequate. When placed in line with each other, inductive coupling between the antennas resulted in unacceptably large surface wave signals, and when placed perpendicular to each other the echo amplitude became very small. Further experiments with antenna configuration showed that shortened or folded dipoles did allow visible echoes to be recorded but never at amplitudes approaching those obtained with the original setup.

5.3 CHARACTERISTICS OF ECHO SIGNALS

5.3.1 Signal Features Caused by the Instrument

Those features of the signal due specifically to the instrument will now be considered, with reference to figure 5.3. The calibration record provides a crystal-controlled timing reference (1 MHz) and helps confirm that the system is recording correctly throughout its dynamic range. Also shown are two records made at the same location at different gain settings. The surface wave signal is prominent near the beginning of these traces, followed by the echo at about 1.4 μs. These signals are superimposed on a low-frequency negative bias which is probably caused by inductive coupling between the two antennas. If the receiver input impedance was much higher, the receiving antenna would be unable to support a current flow, thus reducing this effect substantially; see for example the trace of figure 5.1 made with the high input impedance of an oscilloscope loading the antenna. This effect is not otherwise associated with equipment because a recording made without the transmitter firing (*i.e.* with the optical cable disconnected) shows only small effects over the first microsecond of the record, most probably owing to interference within the receiving electronics. This can be removed from data traces by subtraction.

Figure 5.3c helps explain the problem of timing uncertainty prevalent throughout most of the records. Previous researchers have used the surface wave signal to trigger

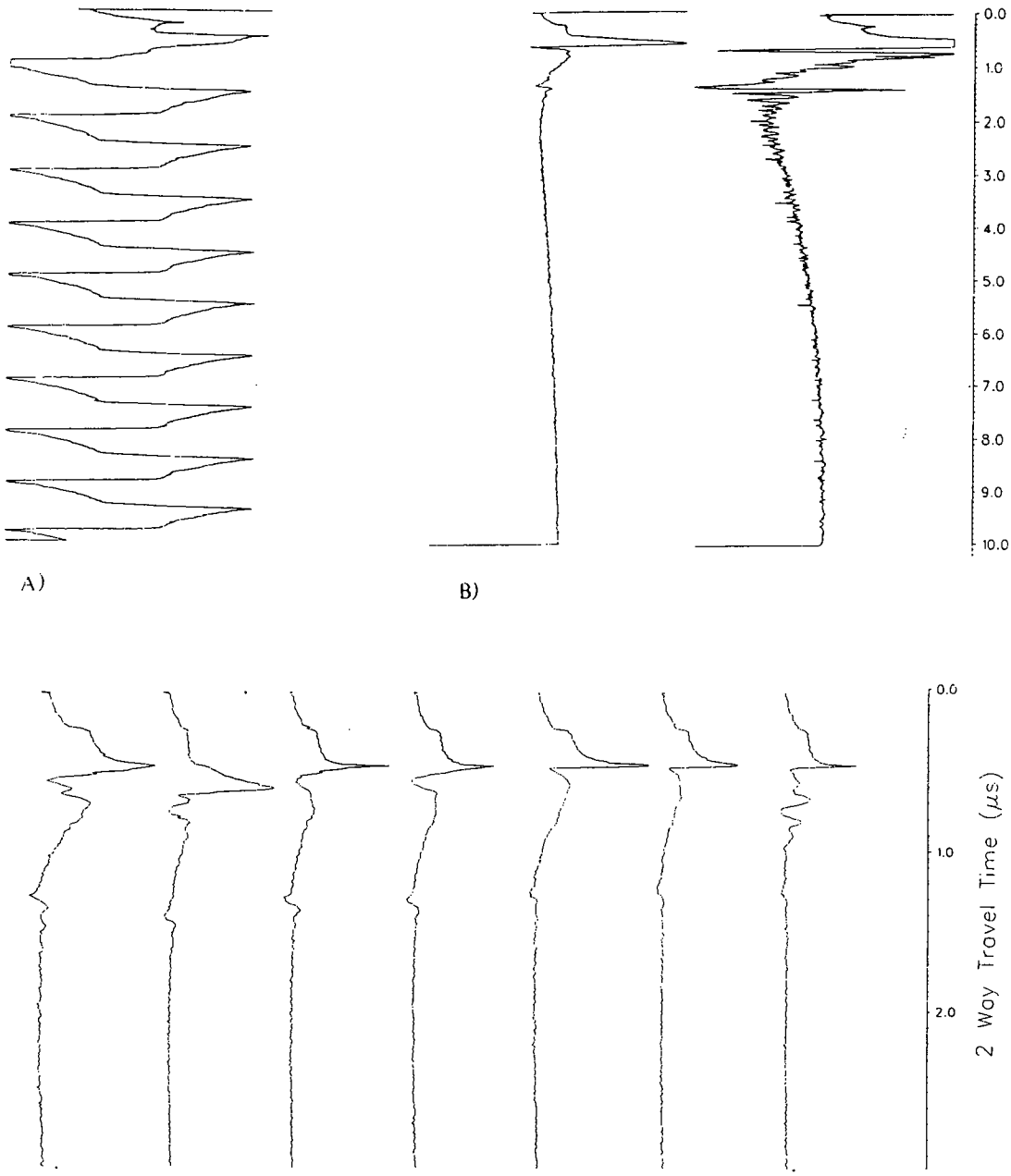

Figure 5.3 Examples of raw data recorded on Trapridge Glacier, 1986. Complete, 1024 sample records are shown in (A) and (B), with the first and last samples having been forced to plus and minus full scale respectively. (A) Crystal-controlled calibration record of 1.0 MHz. (B) Two soundings at the same location; the first was recorded with a gain of 40 and the second with a gain of 150. (C) Various records at low gain taken within hours of each other on the centreline profile. Note that only the first 3 μs of these traces are displayed.

the receiver (*e.g.* Walford and others, 1986; Jezek and Thomson, 1982; Watts and Wright, 1981) but with only variable success. The UBC radar was designed to begin recording before the transmitter fires in order to ensure that the complete surface wave is recorded, thus providing reliable timing reference points. However, most traces are recorded with a gain sufficient to preserve the details of the echo but which severely clips the surface wave signal. Figure 5.3c shows several recordings made at low gain and demonstrates how variable the surface wave signal can be from one location to another. Therefore the exact time of onset is often uncertain by as much as 150 ns, resulting in potentially large depth uncertainties. This variability also emphasizes the problem of wavelet estimation alluded to in chapter 3.

5.3.2 Quantitative Interpretation of Individual Traces

When analyzing echo characteristics, either absolute quantities of the signals can be considered, or relative variations within a signal or set of signals can be examined. The first method must take into account the relations describing propagation of electromagnetic waves from a transmitting antenna, through the medium of propagation, to a receiving system. If all the invariant parameters in these relations are known, it is possible to relate W_r, the useful power delivered to the receiving antenna's load (and presumably the measured quantity), to W_t, the total power fed to the transmitting antenna. First the receiver is assumed to be recording signals that have travelled a distance $r \gg \lambda$, the wavelength in the medium. Also, both antennas are assumed to have identical antenna power gain g_p: a parameter which characterizes the antenna's efficiency and directionality as a function of frequency. The power density P of the electromagnetic field at a distance r from the transmitter is given by $P = g_p W_t / 4\pi r^2$, and the received power is given by $W_r = PA$, where $A = g_p \lambda^2 / 4\pi$ is the effective antenna aperture. For propagation in a lossless medium, combining gives $W_r = W_t (g_p \lambda / 4\pi r)^2$. If there is attenuation and/or dispersion during propagation, and received energy has been reflected from a

boundary with reflection coefficient R, then P is reduced by a factor of $(Re^{-\gamma r})^2$. Thus the received and input powers are related by

$$\frac{W_r}{W_t} = \left(\frac{\lambda g_p R e^{-\gamma r}}{4\pi r}\right)^2 \tag{5.1}$$

Consider now what is known about the parameters of equation 5.1. Constants associated with the media of propagation were discussed in chapter 2. They are the attenuation constant γ, the range r, which is deduced from the two-way travel time, and R, the reflection coefficient. R is presumably the least well known quantity, but can be estimated if the glacier bed properties are known. The instrument properties are not so easily obtained. Chapter 4 discusses how difficult it is to describe the behavior of the antennas quantitatively, but g_p is likely to be small since efficiency of such antennas is low (Shen and King, 1965). Many other types of radar can find their respective g_p by recording echoes from known reflectors (for example, airborne systems can record echoes from water; *e.g.* Narod and Clarke (1983)), but this is impractical for the ground-deployed UBC system with its 20 m centre-frequency wavelength. W_t is also hard to estimate for this wide band system. The total power available at the antenna terminals as well as the antenna's driving point impedance must be measured on the ice if correct values are to be obtained; this has not been done as yet. The ratio W_r/W_t could be replaced by the squared ratio of input and received voltages if the driving and receiving impedances were identical; this is not so and again, to circumvent this problem, the antenna driving point impedance is required.

Rather than pursuing analysis of absolute quantities, more reliable results may be obtained by considering ratios of signal components in such a way that factors common to both parts, such as antenna properties, can be cancelled. Jezek and Thompson (1982) attempt to estimate signal attenuation from the ratio of echo amplitude to surface wave

amplitude. This measure of total attenuation A_t is attributed to absorption A_b, geometric losses A_g, scattering losses A_s, and reflection R. If all these terms are expressed in decibels, then

$$A_t = A_b + A_g + A_s + R. \tag{5.2}$$

For Trapridge Glacier the attenuation constant can be calculated using the relations following equation 2.5. Using an average temperature of $-3°$ C., $\alpha = 0.004$ at a frequency of 8.0 MHz. Then, if the glacier depth is assumed to be 75 m (two-way travel path $r_e = 150\,\mathrm{m}$), $A_b = (20\log_{10} e^{-\alpha r_e})/r_e = -0.035\,\mathrm{dB\,m^{-1}}$. This is in excellent agreement with estimates compiled from various sources and presented in Jezek and Thompson (1982: Fig. 4). Scattering losses A_s will be considered negligible for this cold glacier at frequencies below 10 MHz (after considering Smith and Evans (1972), Watts and England (1976), and the temperature profiles from Clarke and others (1984)), and the reflection coefficient R can be estimated from equation 2.8 if necessary. Geometric spreading causes a reduction in echo strength proportional to $1/r_e$ (equation 2.5) and a reduction in surface signal strength presumed (from Annan, 1973) to be proportional to $1/r_a^2$ where r_a is the antenna separation. Then, following Jezek and Thomson (1982), propagation and antenna parameters are assumed the same for both surface and echo signals, and total geometrical losses that contribute to A_t are $A_g = 20\log_{10}(r_a^2/r_e)\,\mathrm{dB}$. Using these values from Trapridge Glacier, and considering the reflection coefficient to be $R = 20\log_{10} 0.46 \approx -7\,\mathrm{dB}$ (suitable if the glacier is resting directly on a wet till bed with 30% porosity; see chapter 3), equation 5.2 becomes $A_t \approx -5 + 17 - 0 - 7 = 5\,\mathrm{dB}$. Therefore the ratio of echo amplitude to surface signal amplitude is $10^{5/20} = 1.8$, *i.e.* the glacier acts as an amplifier. The most probable reason for this absurd result is the invalidity of assumptions made with respect to A_g. First, the transmit and receive antennas, although themselves identical, do not have identical driving point conditions.

Second, it is not likely that their parameters are the same for both surface and internally emitted energy. Perhaps most importantly, they are not in each other's far field; their separation distance is similar to one wavelength of the centre frequency. Even without these difficulties, the value of A_g is highly sensitive to the separation distance. By way of example, for $r_a = 24\,\mathrm{m}$, the resulting geometric loss is $A_g = 14.7\,\mathrm{dB}$ and for $r_a = 25\,\mathrm{m}$, the resulting geometric loss is $A_g = 17.4\,\mathrm{dB}$. Finally, the variations in surface signals demonstrated in figure 5.3c suggest that there are too many uncertainties in this part of the records to allow surface wave signals to be of much use.

As a result of all these considerations, the surface wave signal will not be used in the analysis of our data. Only echoes originating from within the glacier at distances of over two wavelengths will be considered, so that ratios can be taken which will reliably eliminate characteristics caused by the surface and equipment.

There are a few miscellaneous concerns that can be conveniently dealt with at this point. All theoretical and practical work has assumed that the energy arrives at a reflector at normal incidence. This is not strictly true since the antennas are spaced about 25 m apart. However, application of the appropriate equations for oblique reflection of electromagnetic energy (Jordan and Balmain, 1968) shows that for depths greater than 60 m, errors in the reflection coefficients are never wrong by more than 2%.

One more concern might be that a correction to account for the antenna spacing should be included in depth calculations. Without a reliable time reference, however, this correction becomes meaningless.

CHAPTER VI

ANALYSIS OF FIELD DATA

6.1 INTRODUCTION

In this chapter, results of echo sounding work carried out on Trapridge Glacier in July 1986 will be presented and, to some extent, interpreted. Exhaustive analysis is inappropriate because the 1986 field program was designed to assess how suitable the system is for addressing various glaciological problems, rather than to consider any such problems in detail.

Referring to the map of figure 6.1 for orientation, the surveys carried out are as follows. The centreline of the glacier was first profiled in order to use the instrument as a simple depth sounding tool in as many different situations as Trapridge could conveniently offer. The next three profiles followed lines of drill holes, and were meant to provide additional depth measurements as well as potentially complementary information on other features of the drilling program. Then a 60 m profile with soundings spaced 1 m apart was collected. The purpose was to provide a densely spaced set of data for bed property analysis and to try delineating where on the glacier bed a hole drilled the previous year had connected with a cavity. Finally, a set of records was gathered at one location at 20-minute intervals for 3 continuous days. Here, the object was to correlate temporal variations in the signals with concurrent measurements of basal pressure made by a sensor placed at the glacier bed directly below the radar. Correlation with other hydrological data collected at a site downstream of the glacier terminus was also planned.

Before considering these data sets individually, some general comments are in order. In most cases, only the first 5 μs of data are presented, and bad traces (most often

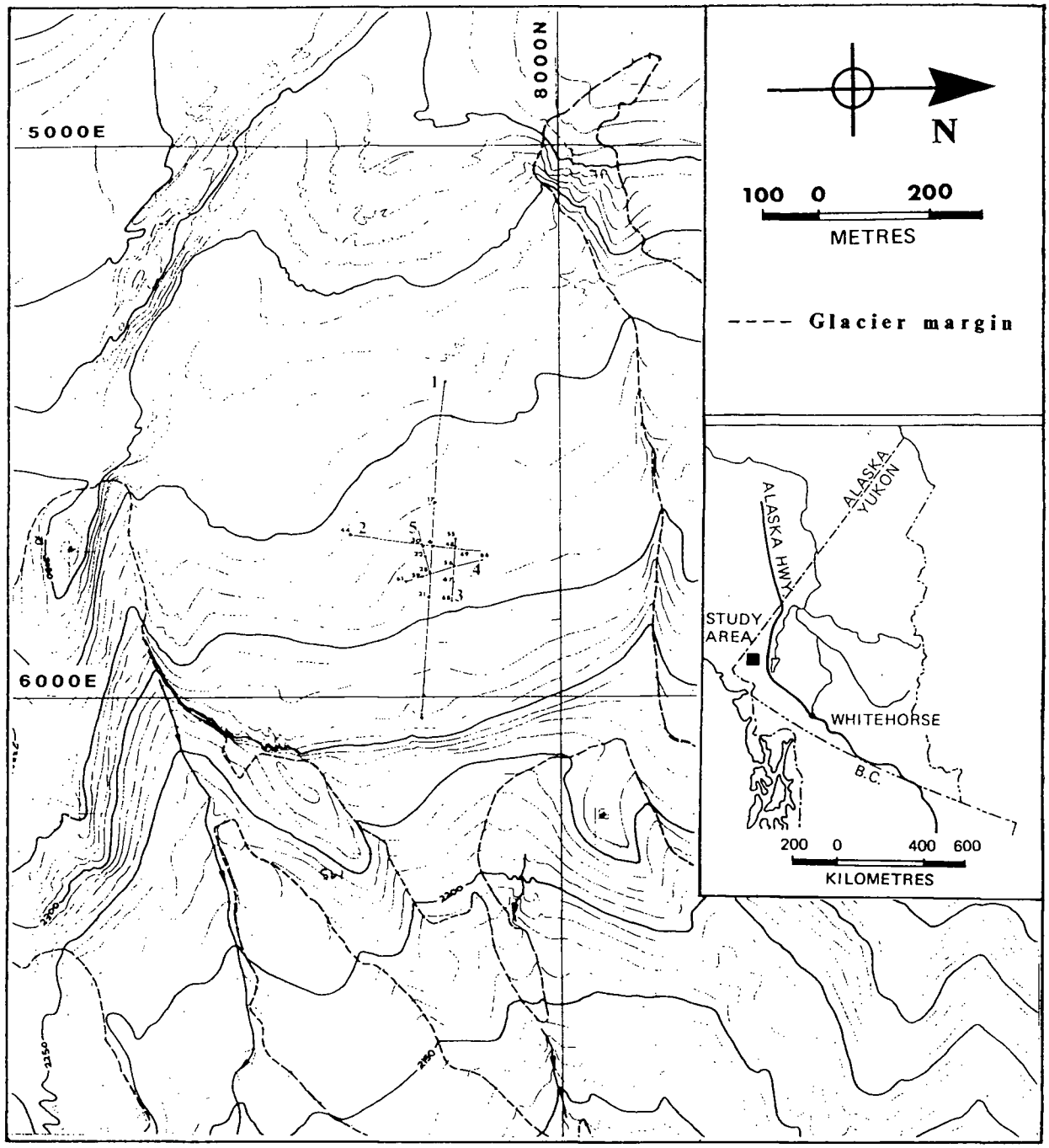

Figure 6.1 Radar profiles on the lower portion of Trapridge Glacier, Yukon Territory. Inset shows the study area. Coordinates are given as the last four digits of the respective Universal Transverse Mercator (UTM) coordinates, and contours are 10 m. Profile lines 1, 2, 3, 4, and 5 are labeled; small numbers locate specific drill holes. All points were surveyed by theodolite and laser ranger. The three-day continuous survey was carried out at hole number 28, the junction of profiles 1, 4 and 5. Note that glacier topography is now more rugged than this 1980 map indicates.

caused by tape writing or reading errors) are replaced by straight lines or blanks. Also, some editing was required to remove calibration traces and low gain records, and to otherwise rearrange the traces into logical sequences or profiles. The uncertainty in timing referred to in chapter 5 has been minimized as follows. For sections not requiring depth information (for example, if bed features were being studied over short distances), traces were aligned using the program discussed in section 3.3.1. Otherwise, traces were aligned individually with respect to visible features of the surface wave signal. In most cases there is also good control information from drilling data. These difficulties will be elaborated upon when each profile is considered separately.

6.2 CENTRELINE PROFILE

The centreline (figure 6.2) is a 500 m profile with soundings spaced at 20 m intervals. It is bounded by an icefall at the western end (although three records were taken within the icefall; another advantage of small, lightweight equipment) and by the now heavily crevassed bulge at the eastern end. (See Clarke and others (1984) for a discussion of this feature, which is characteristic of surge-type glaciers.) Detailed interpretations from this type of survey are impractical because, as we shall see in section 6.4, the fine structure visible at such shallow depths varies greatly within the 20 m sounding spacing. Therefore, this and the next three sections will simply be presented with accompanying figures and major features will be noted. For the centreline profile, traces were aligned with respect to the first falling edge of the surface arrival. Although in general this has been successful, some traces are poorly aligned, notably the fourth from the eastern end. A change in depth of 10 m within 20 m horizontal distance would likely have some form of surface expression on such a shallow glacier; however, none was evident at that location. Use of depths from the drilling program has helped constrain the zero time position on the vertical axis. Note that two records have some superimposed spikey noise. This is likely caused by tape reading or writing errors, most of which are corrected by a parity checking

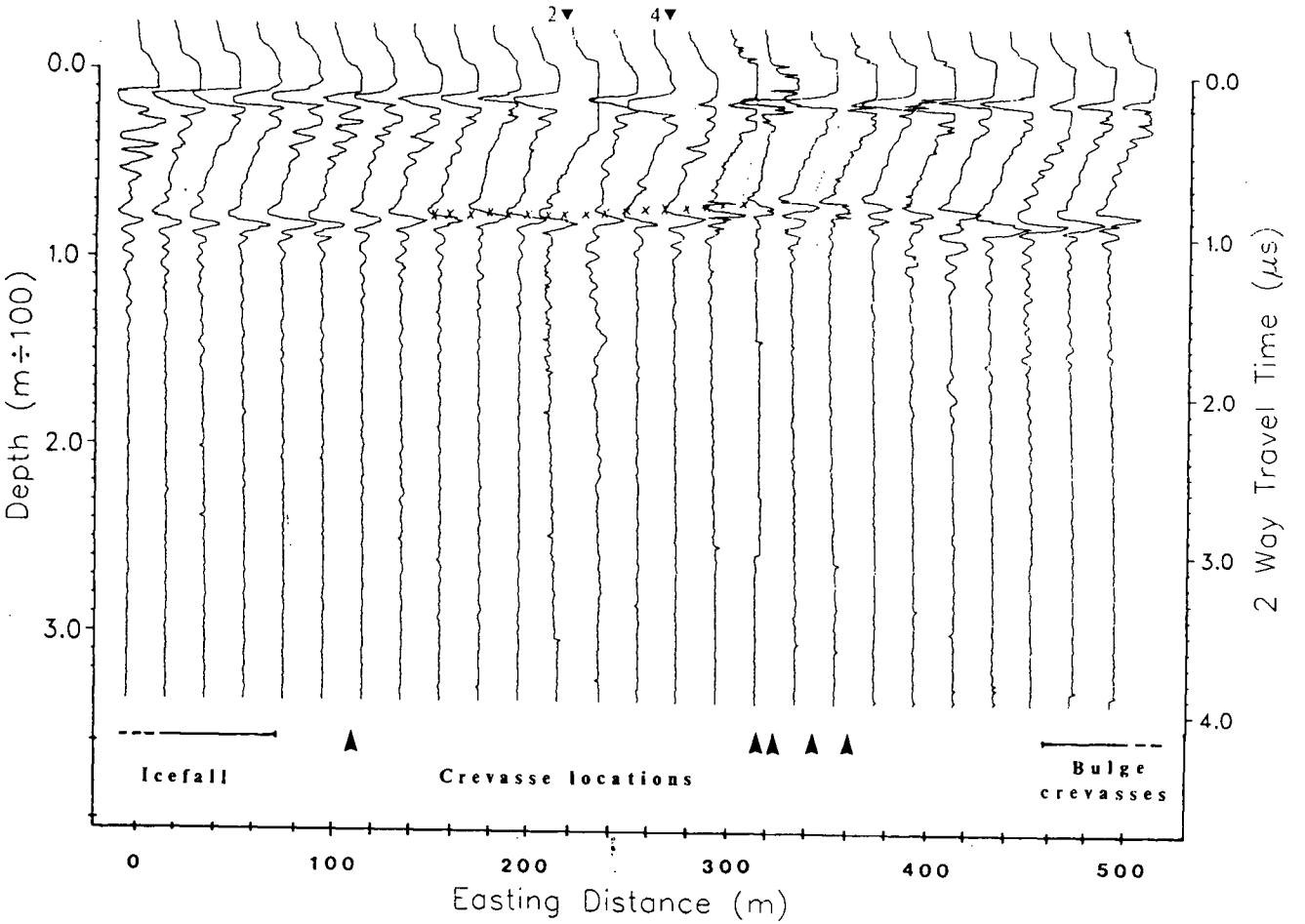

Figure 6.2 Profile 1, the glacier centreline (see the map of figure 6.1). Traces are unprocessed except for truncation of the latter half, alignment of the air wave signal, and plotting. Depth scale was derived using $v = 168.2\,\mathrm{m}\,\mu\mathrm{s}^{-1}$ for the velocity of e.m. waves in ice. Small $\times$'s indicate depths from the drilling program; triangles on top of the section locate profiles that cross this line; arrow heads under the section are locations of crevasses known to exist at the surface.

scheme upon reading of the tape. Major errors may not be recoverable, resulting in apparent amplitude spikes, but in most of these cases, the entire trace has been affected and has therefore been left out.

Observable surface features may help explain other apparently noisy intervals of traces. The first three traces were recorded in the lower portion of an icefall where internal structure is likely to be quite complex. Also, surface crevasses may represent vertical ice/air interfaces capable of generating echoes. The crevasse noted in the figure at 100 m was roughly 1 m across at the surface and was of considerable depth. Other crevasses noted were less than 0.5 m across.

The trailing edges of echoes are of particular interest since they represent effects either at the glacier bed, or at greater distances in directions other than vertically down. It is unclear whether the secondary lobe seen on most traces is a result of the wavelet emitted by the transmitter, or whether it represents a real feature at the glacier bed. A combination of both causes is likely because the lobe is present to varying degrees in virtually all traces gathered at Trapridge. Modelling results from chapter 3 (figure 3.6) suggest that a basal layer of debris-rich ice would have to be roughly 5 m thick to produce a secondary reflection 100 ns after the primary echo. It would also have to contain at least 40% rock by volume for the trailing echo to be as big as those observed. These values are possible but tend to be near the extremes of those observed under stagnant ice below Trapridge Glacier's current terminus (Maxwell, 1986).

Some trailing-edge effects may simply represent energy that has arrived indirectly at the reflector, possibly as a result of multiple echoing within complex structures of the glacier. Records from the icefall may be demonstrating these effects.

The trailing edges of the records from near the terminus are more intriguing. The echoes themselves have stronger amplitudes, and the appearance of multiple echoes at twice the travel time of bottom echoes suggests that here, the bed is a stronger reflector

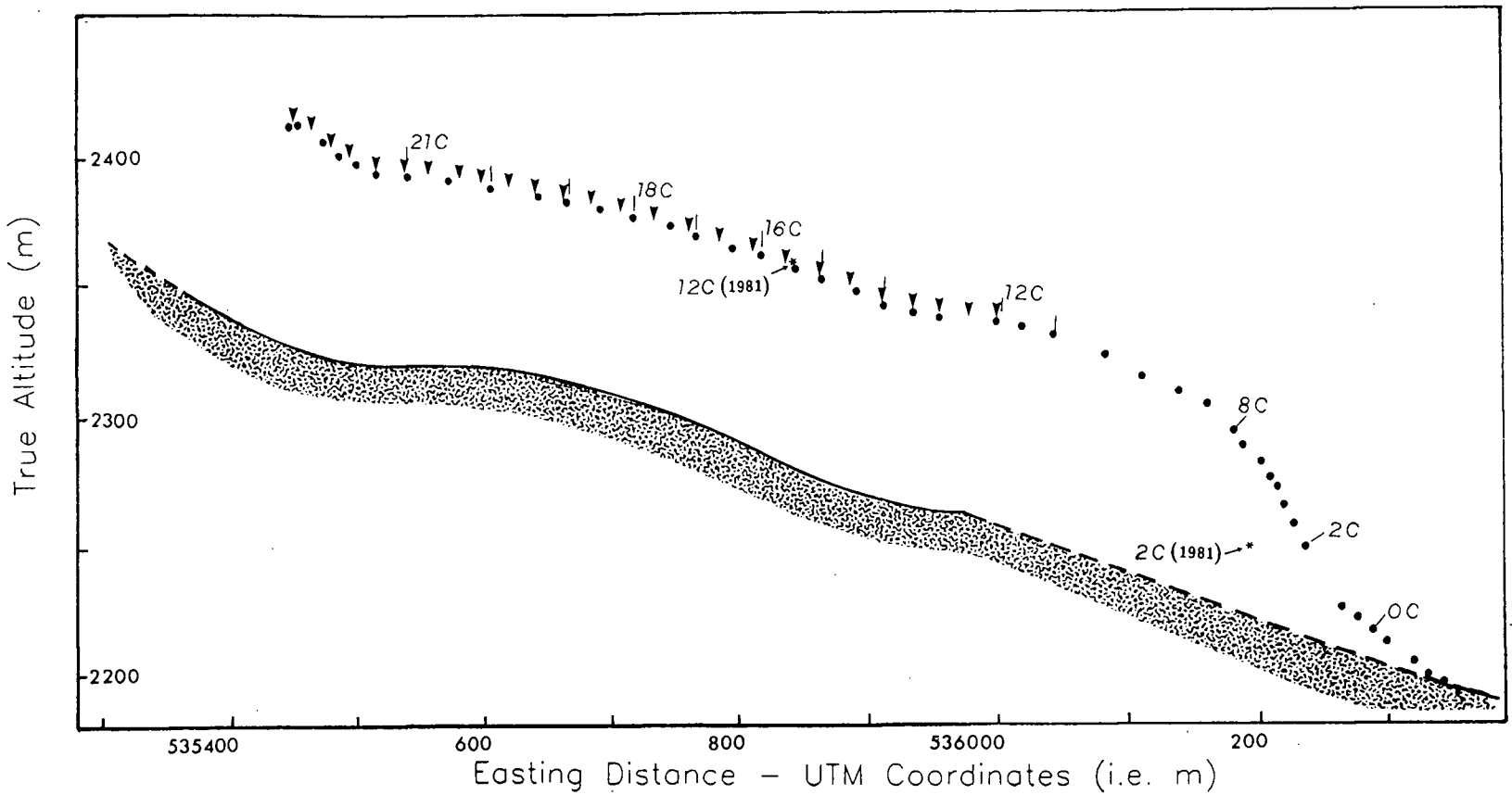

Figure 6.3 Cross-section of Trapridge glacier derived from the centreline profile. Note that vertical exaggeration is 2:1. Plotting this as a true east-west line is not strictly correct but is a good approximation in this case; see figure 6.1 for profile orientation. Surface locations (dots) were surveyed in July 1986 and permanent surface markers are noted (some with labels) by small lines. Positions of radar soundings are marked with small arrow heads. Bed topography was obtained by plotting circular arcs of echo range taken from figure 6.2 below each sounding site. The envelope of arcs was plotted as bed topography and agrees well with that derived from drilling information by Clarke and others (1984). The 1981 positions of two permanent centreline markers (stakes 12C and 2C) are also noted in the figure.

than higher up the glacier. This is at odds with the temperature data from Clarke and others (1984) which show that downstream from the bulge the glacier is frozen to its bed. However, that paper considers data that were gathered in 1983 and the glacier has evolved substantially since then. Also, the true elevation profile of figure 6.3 suggests that there is a topographic levelling at this location. It is conceivable that there is a tendency for water to collect at this location, resulting in stronger reflections of electromagnetic energy.

Focussing of echo energy by large-scale topographic features may contribute to these bottom echo characteristics. Harrison (1970) discusses how two closely spaced returns are possible if topography is such that energy will return to the source location from two sides of a concavity. Application of migration algorithms designed for solving the analogous problem in seismology would help determine whether such effects are occurring, but the current data do not warrant the application of such complicated procedures.

Unfortunately, no other work was done in this region during the 1986 field season, partly because it has become more crevassed in recent years. These crevasses may indeed be the cause of the complexity of the echoes, but if this is true, it is curious that there is not more detail between the surface and the bottom echo.

6.3 PROFILES COINCIDENT WITH DRILL HOLES

Sounding lines 2, 3 and 4 (figures 6.4, 6.5, 6.6) can be conveniently discussed together. For all of them, aligning in the same way as the centreline profile was less successful, as is evident from the numerous traces which have echoes at depths apparently discontinuous relative to their neighbours. The reason for this inconsistency is uncertain, although it should be pointed out that all the records except the first 17 of the long section (figure 6.4) are much noisier than sections taken at earlier dates (the centreline and close-spaced profile). This noise is not altogether random, indicating that the instrument itself may

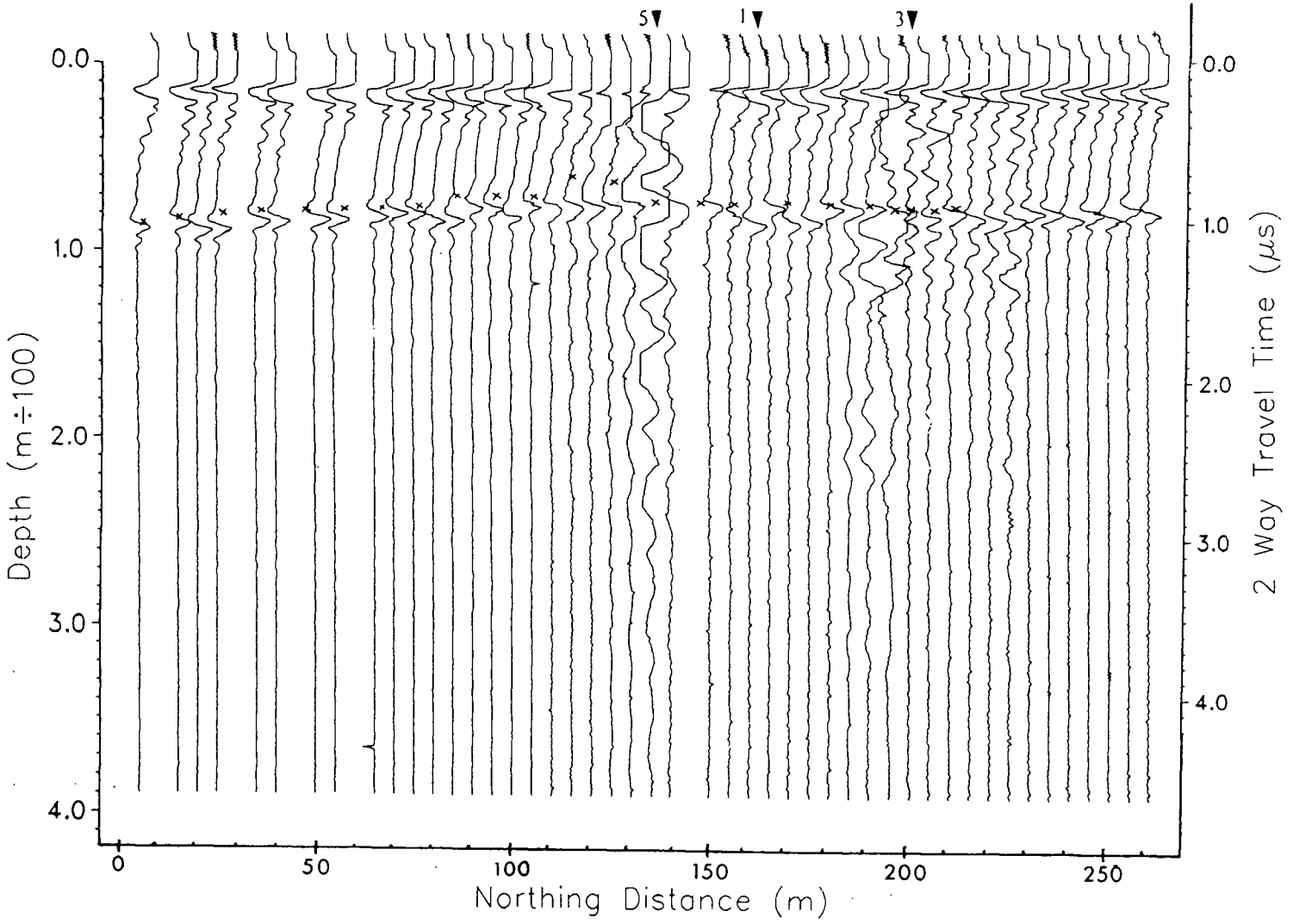

Figure 6.4 Profile 2, the longer of two transverse survey lines. Notes for figure 6.2 apply. Also, there is a buried medial moraine between 100 and 150 m and the drill holes between 190 and 210 m were connected to the subglacier drainage system.

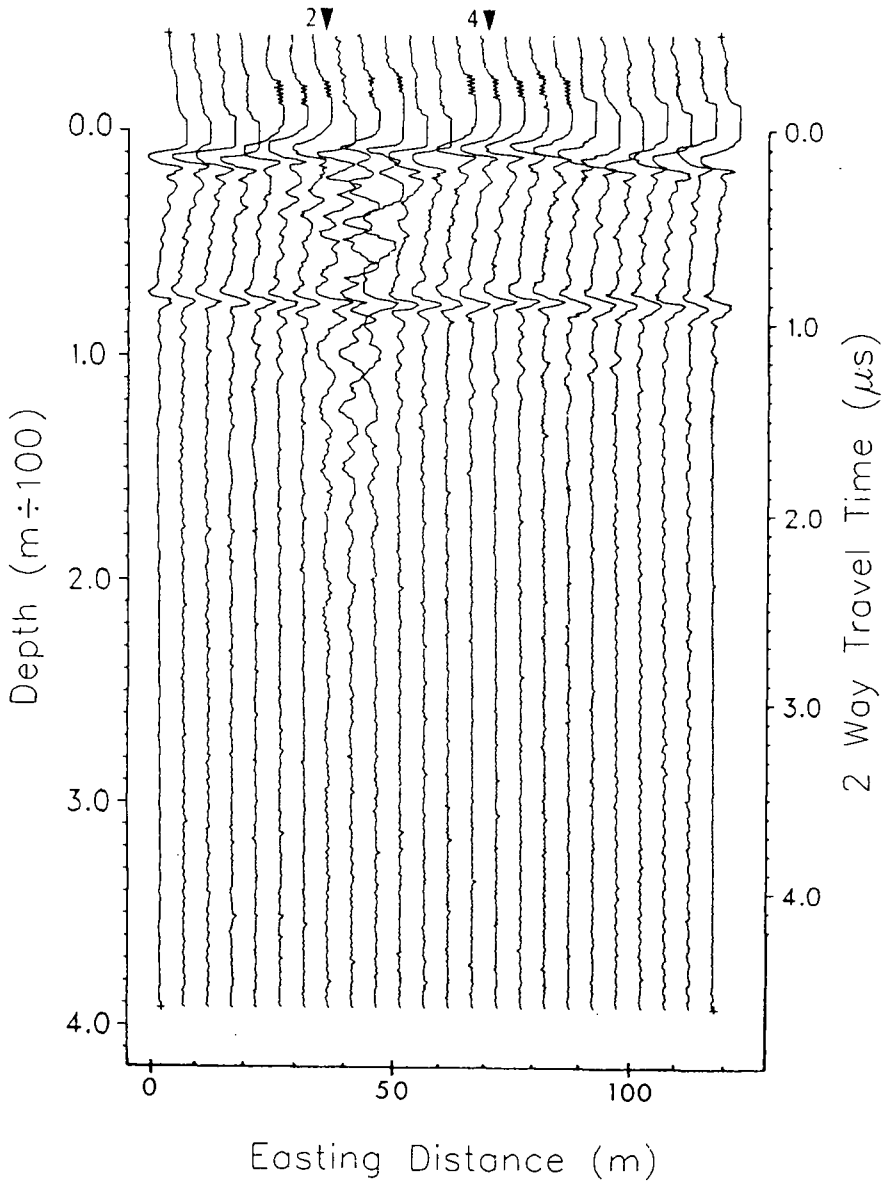

Figure 6.5 Profile 3, parallel to and north of the centreline. See figure 6.4 for notes.

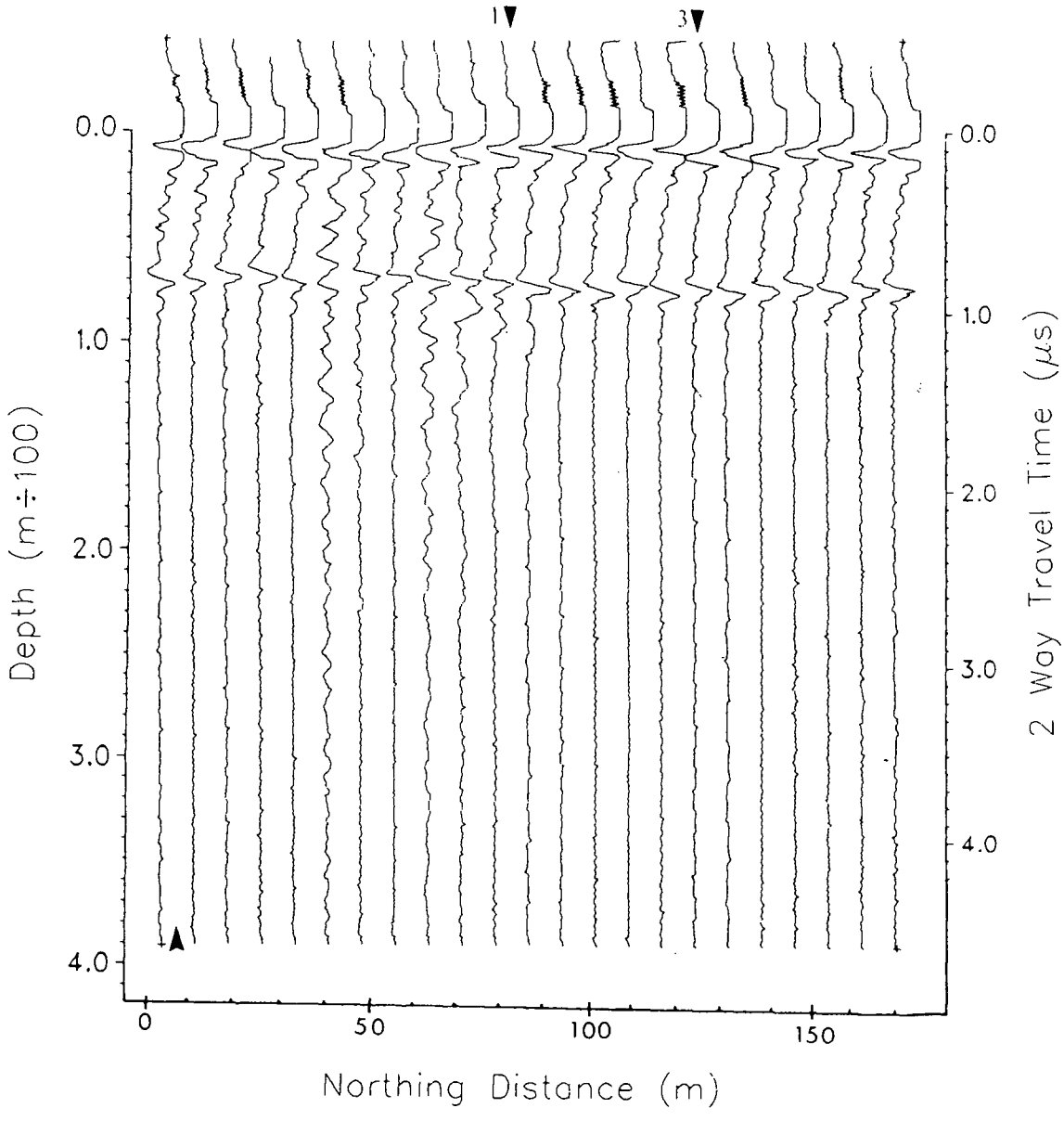

Figure 6.6 Profile 4, the shorter, eastern transverse survey line. See figure 6.4 for notes.

be at fault. Whatever the cause, it appears to be intermittent since the three-day data set (discussed in section 6.5) is neither as noisy nor as poorly aligned.

Glacier features along these lines should be noted next. The southern end of both transverse lines is bounded by a series of large crevasses, associated with a topographic rise. Also there is known to be a medial moraine running perpendicular to these two profiles, located roughly between 100 and 130 m of the long profile and between 37 and 70 m of the shorter profile. Note the anomalous drilling depths in profile 2 around 120 m, which probably indicate the presence of morainal material in the path of the drill. It should also be noted that the drilling equipment consisting of propane bottles, pumps, hoses, equipment cases etc. was at the intersection of the centreline and profile 2. Finally, surface conditions were extremely wet over the first 100 m of the long profile, but virtually dry and clear of snow for the rest of these three profiles.

Before looking at the most striking features of these profiles, it is worth noting that the trailing edges of most echoes do not exhibit secondary pulses as prominently as the centreline records. Also, at the points where profile lines cross each other, the echoes are similar in character, so it is probably safe to say that whatever causes the secondary lobes on the centreline is generally less evident across the width of the glacier under the drilling lines. There are notable exeptions, however. In all three profiles, secondary echoes appear in the vicinities of anomalous recordings. One is around the zone of buried morainal material, and another is located roughly 80 m further north. No mechanism for causing such dramatic effects on radar signals has been found, but there are a few ideas worth considering.

Chapter 2 discussed how a thin layer of contrasting intrinsic impedance will preferentially reflect frequencies for which the layer thickness is an odd multiple of a quarter wavelength. The fact that ringing echoes are possible from such a layer has been discussed by Smith and Evans (1972), and figure 6.7 models the effect using the scheme

explained in chapter 3. This is for a water layer bounded on both sides by ice, for example a water-filled crevasse. Such an effect could not occur at the glacier bed, however. It was noted in chapter 3 that thin "Weertman films" are not detectable with these radar techniques, and a thick basal water layer will not ring for the same reasons: attenuation in water is too great and the reflectivity of a water/glacier bed interface is too small. The observed anomalous records are therefore unlikely to be caused by water layers, especially those records that start ringing near the surface.

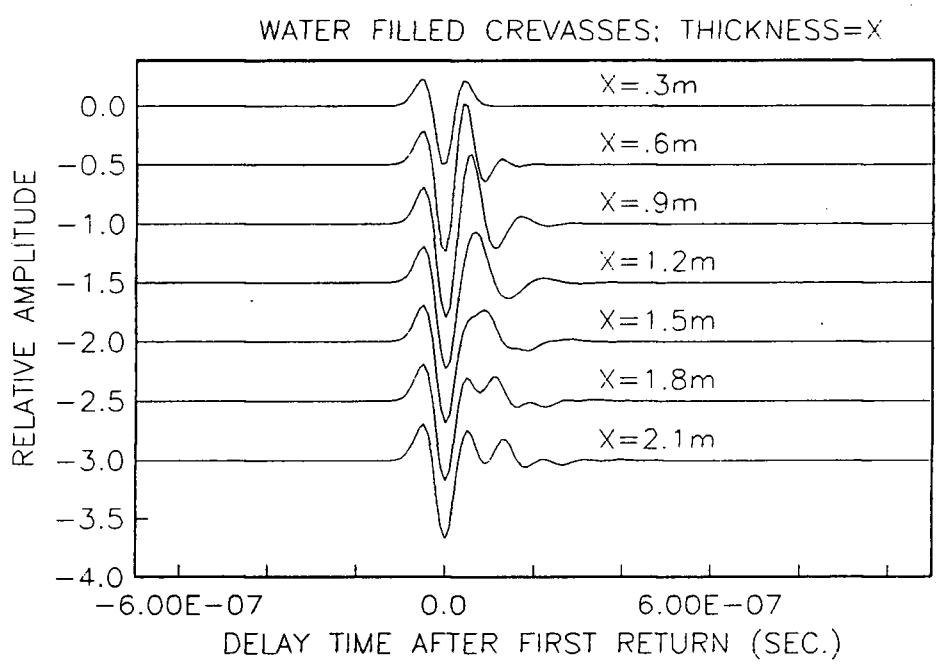

Figure 6.7 Modelling as per the methods of chapter 3 using the same input wavelet as figure 3.6. Ice parameters: $\sigma_i = 3 \times 10^{-5}\,\mathrm{S\,m^{-1}}$, $\epsilon_i = 3.18$. Water parameters: $\sigma_w = 0.01\,\mathrm{S\,m^{-1}}$ (appropriate for subglacial water but not for surface melt), $\epsilon_w = 81$.

Jacobel and Raymond (1984) suggest that ringing records observed on Variegated Glacier, Alaska, are caused by voids within the glacier. This explanation is less likely on Trapridge because it is cold throughout at this location. Furthermore, the theoretical work of Watts and England (1976) shows that the scattering efficiency of spheres is very small for radii less than 0.1λ. If the frequency is around 8MHz, spheres at least 4 m in

diameter would be required, and lower frequencies would require still larger scattering targets. Such large water-filled voids are unlikely to exist within a cold glacier.

Some of the records that have noisy rather than ringing characteristics are probably affected by morainal material; this is likely for traces between 110 and 140 m of profile 2 and for traces between 30 and 70 m of profile 4. These still have unexplained pulses following the bottom echo which are similar to a feature on the short, close-spacing survey presented next. Another possibility is that wiring on top of or within the glacier may be causing some effects. However, there is no consistency when comparing records that have been made near known emplacements of long wires. Crevasses may explain minor noise-like features on some records near the extremities of the profiles, but there are none near the northern ends of the surveys.

Finally, it is intriguing to note that the confused records at the north end of profile 2 (also evident on profile 3 at the point where these two lines cross) are in the same location as those drill holes that first revealed hydraulic connections to the glacier bed. No connections were found in any earlier holes, while most holes drilled after the first connections did in fact connect. Therefore the feature near the center of profile 2 had no associated connection, and there were connections over parts of profiles 3 and 4 that show no extraordinary characteristics. In addition, it is hard to see how features associated with the glacier bed could cause ringing or noisy signals at shorter delay times than those of the bottom echo.

The most important conclusion to be drawn from these three surveys is that more extensive coverage is required if anomalous echoes are to be better understood. Soundings must be taken at very dense spacing, two-dimensional coverage is required, and soundings with various antenna orientations should be made to distinguish features that may respond to different polarizations of incident electromagnetic waves.

6.4 PROFILE WITH CLOSELY SPACED SOUNDINGS

The profile made with soundings taken at 1 m intervals (figure 6.8) provides a number of possibilities for interesting glaciological interpretations. Two features become prominent after alignment with respect to the bottom echo (valid since depths along this line, determined from drilling data, were all 71.5 $\pm$ 0.5 m). The first feature, at the southern end, is a secondary pulse following the bottom echo. The second is the emergence of an englacial echo that becomes closer to the surface wave towards the northern end. This feature will be considered first since it can in principle be used as a reference when analyzing other signal features.

6.4.1 Englacial Reflector: Location and Reflectivity

The range to the internal reflector is found from figure 6.8 to be 53 m for trace 40 and 35 m for trace 60. Since these traces were recorded 21 m apart and the echo range changes by only 18 m, a line reflector causing this echo would lie at an angle of $\sin^{-1}(18/21)$ or 59° off the survey line. Photographs of the region show that there is a crevasse in roughly this orientation nearby. The result is further supported by comparing the internal echo amplitude of trace 50 with those of the records from the three-day continuous survey. This point is clarified in section 6.4.3. Note that a single reflecting body is an unlikely cause for such a reflection for the reasons explained in the previous section.

The reflection coefficient of an ice/air boundary is $R = 0.28$ from table 2.2. What happens to this coefficient if the reflector is in fact a thin air-filled crevasse? Equation 2.10 can be solved using the following parameters: $\eta_i = 211$; $\eta_a = 377$; $\rho_{ia} = 0.28$; $\rho_{ai} = -0.28$; $\tau_{ia} = 1.28$; and $\tau_{ai} = 0.72$. The propagation constant is $\gamma = \alpha + j\beta$; $\alpha \approx 0$ in air and $\beta = \omega/v = 0.168$ at 8 MHz in air. Solving equation 2.10 for crevasse thicknesses of 0.5 m $< x <$ 1.5 m yields reflectivities of $(0.057/-41°) < \rho_i < (0.127/-59°)$ or $-24.9\,\text{dB} < |\rho_i| < -17.9\,\text{dB}$. Thus the magnitude of the reflection coefficient is significantly less than for an interface with an infinite half plane of air, and the phase

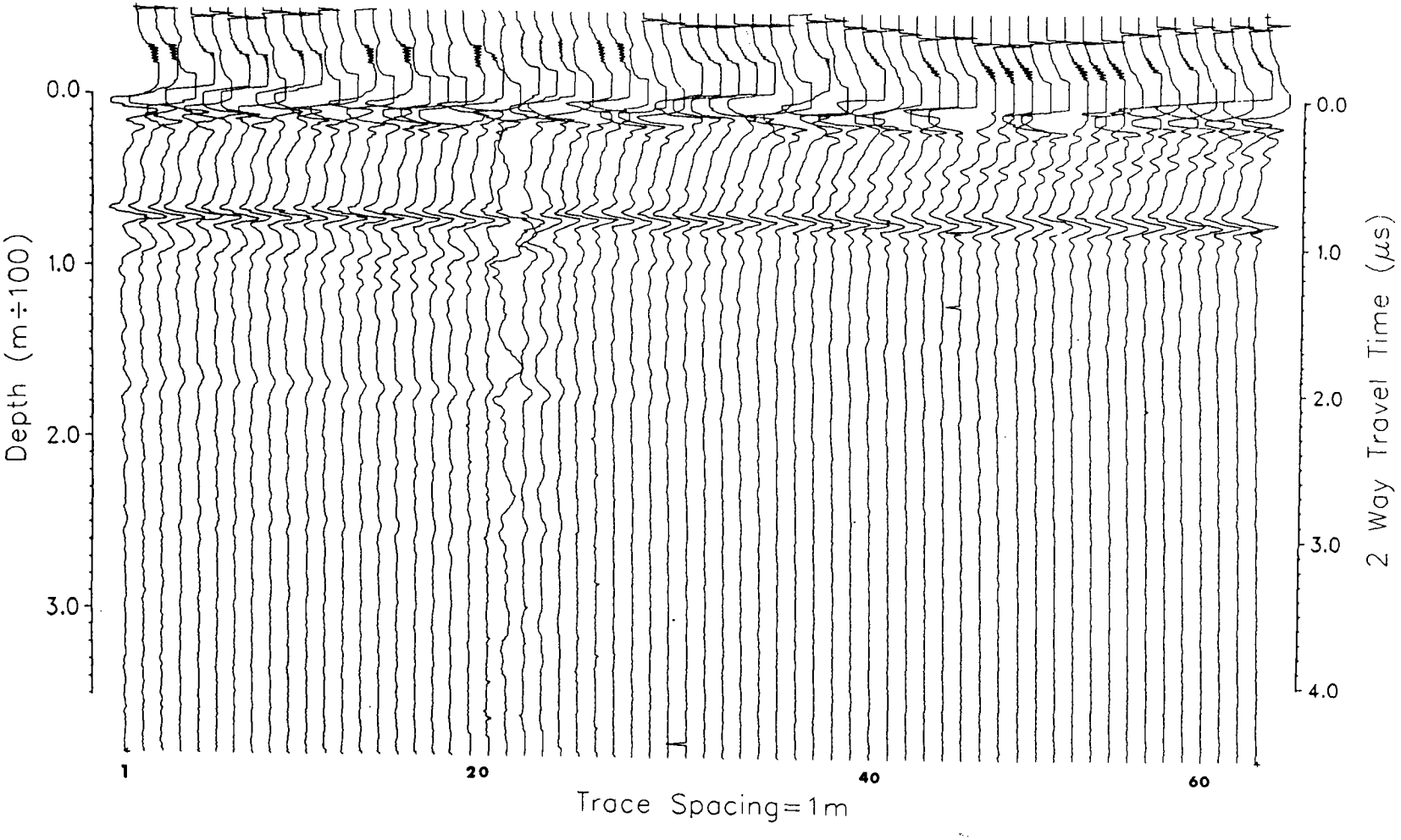

Figure 6.8 Profile 5, the close-spacing survey. Notes are as per figure 6.4. Note that these records have been aligned with respect to the bottom echo. Refer to the text for discussion.

of the echo will have been shifted. Actual echoes are too small to accurately reveal this phase shift, but it will be shown in section 6.4.3 that such reflectivities are consistent with echoes known to originate from a crevasse.

It is worth noting in passing that detection of crevasses in this way might help make surface travel over dangerously crevassed terrain safer. Radar frequencies may even be chosen to emphasize crevasses within a certain size range.

6.4.2 Estimation of Attenuation Constant

The amplitude of an echo a can be expressed in terms of its range r, the attenuation constant of the medium α, and the reflection coefficient ρ, by an equation similar to equation 2.5: $a = (K\rho e^{-\alpha r})/r$ in which K contains all the information regarding transmission power and system performance. If two echoes from the same target are recorded at different ranges and the ratio of their amplitudes is taken, the common factors K and ρ will cancel leaving an expression with the attenuation constant as the only unknown. That is:

$$\frac{a_1}{a_2} = \frac{r_2 e^{-\alpha r_1}}{r_1 e^{-\alpha r_2}} \,. \tag{6.1}$$

Amplitudes a_i were found with the aid of figure 6.9a which plots the maximum peak-to-peak amplitude found in given time windows for each trace. The figure caption explains minor processing that was required. Ranges were read from figure 6.8 and then equation 6.1 was solved for pairs of traces chosen to ensure that amplitudes were not contaminated by either the bottom echo or the surface wave signal. As might be expected from the variability of echo amplitudes seen in figure 6.9, the derived α's were also highly variable. The average α over 15 trials was $\overline{\alpha} = 0.0064$ with a standard deviation of $s = 0.0057$. This is significantly higher than the expected attenuation constant of about 0.003. The relations following equation 2.5 were used for this estimate, with the assumption that the average temperature of Trapridge Glacier's upper 20 m is about

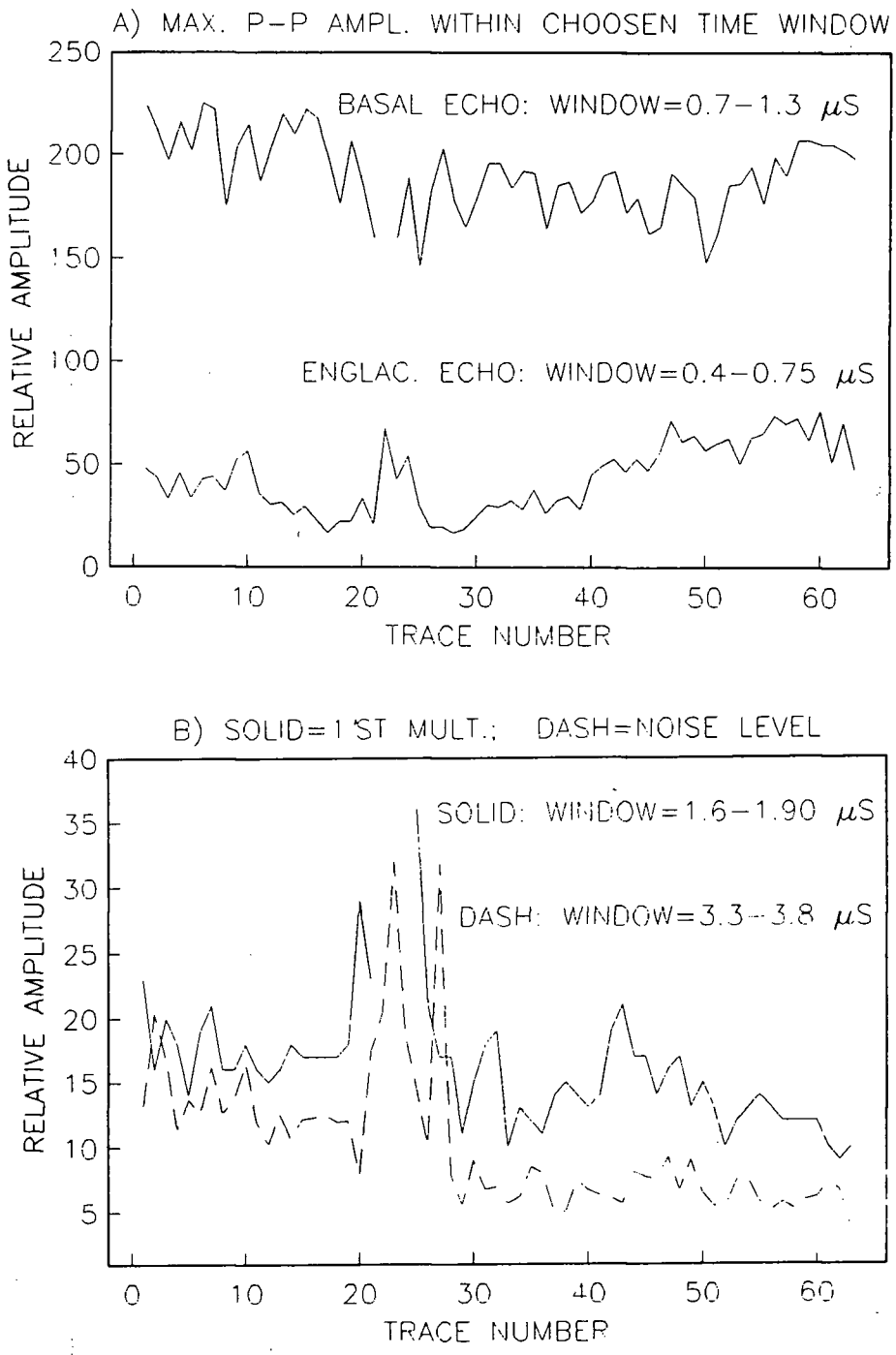

Figure 6.9 Amplitude plots of close-spaced profile. Basal echo: the maximum peak-to-peak amplitude was found within the time window shown and plotted for each trace. All others: The linear trend over all points within the window was found using least squares regression over all points within the window. This trend was removed and the maximum peak-to-peak amplitude then found within the window. In all cases, amplitude units are relative to the maximum dynamic range of the digitizing receiver which is 256; the analogue-to-digital converter currently has a resolution of 8 bits. Conversion to volts at the antenna depends on the gain setting at the time of recording.

6°C. Travel times are great enough to ensure that echoes are not air-path arrivals, so the signals have been acted upon only by features within the ice, or by the effect of travelling very near the ice/air boundary.

We must therefore consider which of the assumptions inherent in equation 6.1 have been violated. First, propagation is in a non-uniform medium, *i.e.* is parallel to a surface. Annan (1973) considers such a geometry; for distances of more than a wavelength, surface effects are expected to be small. Perhaps more important, the reflector is not an infinite plane. The situation is more like a diffraction problem with energy incident on a line diffractor (the crevasse lip). Alternatively, we could consider diffraction from a wedge-shaped body with the ice/air/crevasse corner as the apex, and the energy at grazing incidence along one side of the wedge. Narod and Yedlin (1986) discuss a similar acoustic problem, from which it is evident that both geometrical optics and diffracted wave fields would have to be considered. In the present case, complications due to normal incidence would also have to be included. This is by no means trivial and is beyond the scope of this thesis. Suffice it to say that solving equation 6.1 assuming only a diffracted wave field (implying geometrical losses proportional to $1/r^{3/2}$ rather than $1/r$) results in very small attenuation constants, so use of the complete solution is likely to yield answers that are less than the $\overline{\alpha}$ found above. In other words, we should expect signals returning from such a reflector to be smaller and to decay faster than echoes from an ideal plane reflector. Such behavior would imply a smaller attenuation constant, as predicted above simply from the physical properties of ice. The true attenuation constant can be confirmed only by more detailed consideration of the theory, and through controlled experiments in the field. Reduction of the variability by stacking would also help, a point considered again at the end of this chapter.

6.4.3 Basal Reflection Coefficient

If the internal echo originates from a known reflector, the basal reflection coefficient can be estimated. A ratio can be taken as above using the appropriate values for amplitude, range and attenuation:

$$\frac{a_i}{a_b} = \frac{r_b e^{-\alpha_i r_i} \rho_i G^2}{r_i e^{-\alpha_i r_b} \rho_b} \tag{6.2}$$

where the subscripts i and b denote internal and basal reflector parameters.

G accounts for the directionality of the antennas and must be included if the signal path is not perpendicular to the antenna array. It is related to the angle θ, between the signal path and the normal to the antenna in a manner dependent on the type of antenna. From Jordan and Balmain (1968, section 11.03),

$$G = \frac{\cos(\frac{\pi}{2}\cos\theta)}{\sin\theta} \tag{6.3}$$

for a half wave dipole and $G = \sin\theta$ for an elemental dipole. For a damped halfwave dipole, the value of G is likely to be between these two, probably closer to the elemental dipole. This factor affects both transmitting and receiving antennas, so the recorded echo strength will be reduced by a factor of G^2.

In our case, the remaining parameters of equation 6.2 are as follows. The two-way travel distances are taken from figure 6.8; the attenuation constants are $\alpha_b = 0.004$ (assuming an average temperature throughout the glacier of $-3°$C) and $\alpha_i = 0.003$ (average temperature in the glacier's upper 20 m is about $-6°$C); $G = 0.805$ assuming $\theta = 59°$ as above (the half-wave dipole formula gives this conservative estimate); the two amplitudes a_b and a_c are found as described in figure 6.9a; and the magnitude of ρ_i for a 1 m wide crevasse is $|\rho_i| = 0.09$ (-20.1 dB). Equation 6.2 was then solved with these parameters for traces 40 through 60 to yield an average basal reflectivity of $\bar{\rho}_b = 0.42$

($-7.5\,\mathrm{dB}$) with a standard deviation of $s = 0.05$. The result is most sensitive to G and ρ_i but expected variations of these two parameters can be somewhat constrained. Photographs of the area show that the survey line and crevasse are oriented about 60° to each other. Also, the englacial echo amplitude from trace 50 is approximately four-fifths of that for the same echo from the three-day data set (discussed later) which was recorded at the same location with antennas *parallel* to the crevasse. This implies a directionality factor $G = \sqrt{4/5} = 0.89$ which corresponds to an angle between reflector and antennas of about 65° (depending somewhat on whether a half-wave dipole or an elemental dipole is assumed when calculating G). Concerning ρ_i, photographs of the area show that the near by crevasse is indeed about 1 m wide.

It should be reiterated here that this average basal reflectivity was found under the same assumptions concerning propagation and reflector geometry as described in section 6.3.2. In fact, the crevasse echo can be expected to decay faster than assumed by equation 6.2, resulting in smaller basal reflectivities than predicted here. On the other hand, equation 6.2 also assumes a specular basal reflector. If the same data were used with a model including more realistic glacier beds, higher basal reflectivities would be predicted. These two effects may work towards cancelling each other, but until the complete relations are incorporated, the estimates above will be used to make tentative glaciological interpretations.

These considerations suggest that the glacier bed reflectivity is likely to be around 0.3 to 0.4 ($-10\,\mathrm{dB}$ to $-8\,\mathrm{dB}$). Table 2.2 shows that this is greater than that of a solid rock glacier bed and less than that of water layers that are thicker than a few millimetres. Porous materials with conductive interstitial water have reflectivities comparable to this result, and so do very thin water layers, or Weertman films. Whatever the bed is, it is probably uniform except for localized anomalies since most profiles have similar echo strengths. A Weertman film requires an impermeable bed (Drewry, 1986) and evidence

from temperature, drilling, pressure, and other hydrological investigations (Clarke and others, 1984; Clarke and others, 1986; Maxwell, 1986; Smart, personal communication) argue strongly against the widespread presence of a Weertman film under Trapridge Glacier. The conclusion then is that the radar data suggest a glacier bed with porosity in the range of 10% to 25% if water conductivity is conservatively estimated at around $100\,\mu\mathrm{S\,cm^{-1}}$. The same reflectivity could occur for lower porosities if water conductivity is higher.

6.4.4 Multiples and Secondary Bottom Echoes

Similar ratio calculations can be carried out using amplitudes of multiple arrivals and bottom echoes. The ratio in this case is

$$\frac{a_b}{a_m} = \frac{2e^{-\alpha r}}{e^{-\alpha 2r}\rho_a\rho_b} \tag{6.3}$$

where the 2's occur because the range for the multiple is twice that of the bottom echo; $\rho_a\rho_b$ is required since the multiple is reflected from the ice/air boundary once and from the bottom twice; and a_b and a_m are amplitudes of the bottom echo and multiple. Surface propagation and diffraction effects are of little concern in this case. Solving for the unknown gives $\rho_b = 12.6(a_m/a_b)$ when the depth is 71 m, $\alpha = 0.004$, and $\rho_a = 0.28$ from table 2.2. For traces at the eastern end, figure 6.9a shows $a_b \approx 180$ so that $\rho_b \approx 0.42$ ($-7.5\,\mathrm{dB}$) if $a_2 \approx 6$ is used. This is justified by figure 6.9b which plots the noise level at large time delays, as well as the maximum amplitudes of traces in the time window where bottom multiples are expected. (They are in fact faintly observed at around $1.7\,\mu\mathrm{s}$ in figure 6.8.) Removal of the noise level leaves $a_m \approx 6$ in the region of traces 30 to 60. The value of ρ_b found in this way reinforces the tentative conclusion that the glacier bed has a relatively high reflectivity.

The remaining prominent features are the strong secondary pulses following the bottom echo and the correspondingly strong multiples of these pulses. These are at the western end and correlate well with similar features of profile 2. They also appear to fade after the anomalous trace 21. No explanation has been found for such a trace when the soundings were only 1 m apart so, for the present, it must be counted as an error. The remaining features are too consistent to be dismissed, but they remain unexplained. Using equation 6.3, a basal reflection coefficient of $\rho_b = 12.6(a_m/a_b)$ would give $\rho_b = 12.6(15/200) = 0.95$. This implies an almost perfect reflector which is physically rather unlikely. Some form of constructive interference might be occurring, but there are insufficient data to speculate further. Figure 6.7 may shed light on the thickness of an ice enclosed, water-filled void that can produce ringing echoes, but such a void would have to resemble a crevasse in size (as argued in chapter 5), and no explanation has been found for the extraordinary strength of the multiples. The possibility of a cavity having been observed is tantalizing but is not supported by results from the drilling program (as yet unpublished).

Finally, the filtering experiments described in chapter 3 suggest that a thick layer of debris-rich ice could probably not cause such bottom echoes because the reflection coefficients of ice/rock mixtures are not high enough. More extensive surveys, as noted in the conclusions of section 6.3, are needed to further elucidate the features observed here, which were assumed to be associated with the connected hole of 1985.

6.5 THREE-DAY DATA SET

The set of records shown in figure 6.10 were recorded at 20-minute intervals over a period of three days at the same location as trace 50 of the close-spaced survey. Simultaneous recordings of pressure at the glacier bed were made in a manner similar to that reported by Clarke and others (1986), and the intention was to compare these data. Unfortunately, the 1986 pressure data are still unobtainable owing to technical problems with

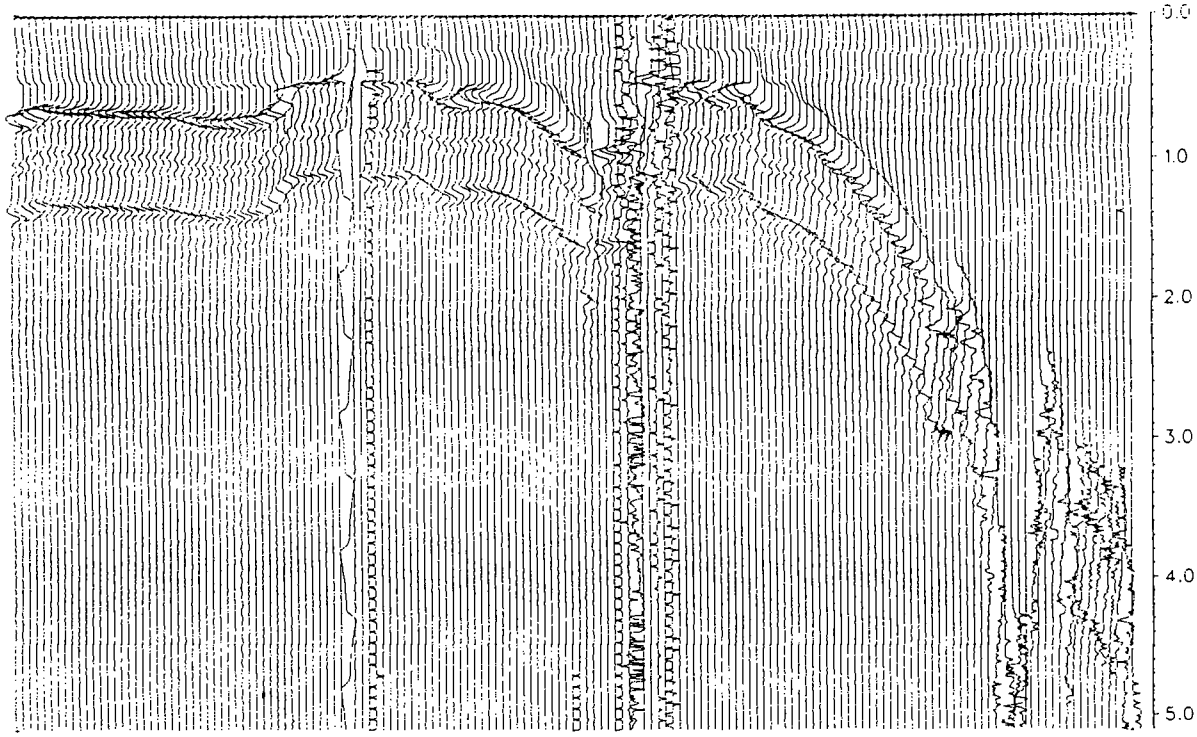

Figure 6.10 Complete set of raw data collected automatically over three days at drill hole number 28 (see figure 6.1). Increased transmitter triggering delays are observed during cooler periods (see figure 6.11 for times). Towards the end, temperatures dropped steadily during the onset of a storm. One calibration record is visible in the first half of the set, and noisy records in the center are caused by tape reading or writing errors.

the appropriate cassette reader. Temporal variations in bed reflectivity can therefore be analyzed only qualitatively in light of hydrology data that were gathered downstream of Trapridge Glacier's terminus and the known concurrent meteorology. The effects of cold temperatures are immediately evident in figure 6.10; triggering of the SCRs was delayed by the cold and in extreme cold (during the onset of a storm on the last day of recording), triggering became erratic so that each pulse was different and the sampling timebase receiver produced useless records. The unreliability of our cassette recorder for this kind of field application was also made clear. Twice during automatic operation, the system encountered uncorrectable read and/or write errors which left it unable to

proceed. It was restarted when found at the time cassettes were to be changed. This accounts for the gaps in time noted in figure 6.11, which displays the useful data after alignment with respect to the bottom echo.

Features immediately evident on this temporal section are as follows. An occasional noisy trace appears for unknown reasons; those that are unusable have been replaced with blanks. The secondary pulse following the bottom echo is present as in most sections recorded at Trapridge, but it appears to vary in size across the section. The same can be said for the englacial echo, the amplitude of which was used in the previous section. Finally, there is a hint of multiple echoes between 1.5 and 2.0 μs, also with somewhat variable amplitude.

Amplitude variations are displayed most conveniently in the plots of figure 6.12. Also shown is a normalized set of amplitudes constructed by dividing the bottom echo amplitude by the englacial echo amplitude. This ratio effectively removes signal components that are common to both signals. Evidently, the diurnal variations in basal echo amplitude are not related to changes in bed reflectivity because the englacial echo is affected to an almost identical degree. Any visible change in reflectivity caused by pressure or other hydrological events ought to be seen in this ratio plot since instrument and climatological effects should have been removed.

Another potentially interesting parameter is the average power level displayed in figure 6.12b. If the excessively noisy traces are ignored (blanks in this plot) there does seem to be a reduction in noise level arriving from sources at greater ranges than the depth. This may be a result of reduced englacial water content, possibly owing to the cooling trend in the weather, or perhaps to the draining of subglacial storage cavities. Such an event would lower the basal water pressure with a resulting decrease in the water table; the degree of interconnection amongst englacial water channels would determine the rate at which this level would drop. Speculative as these ideas are, it is intriguing

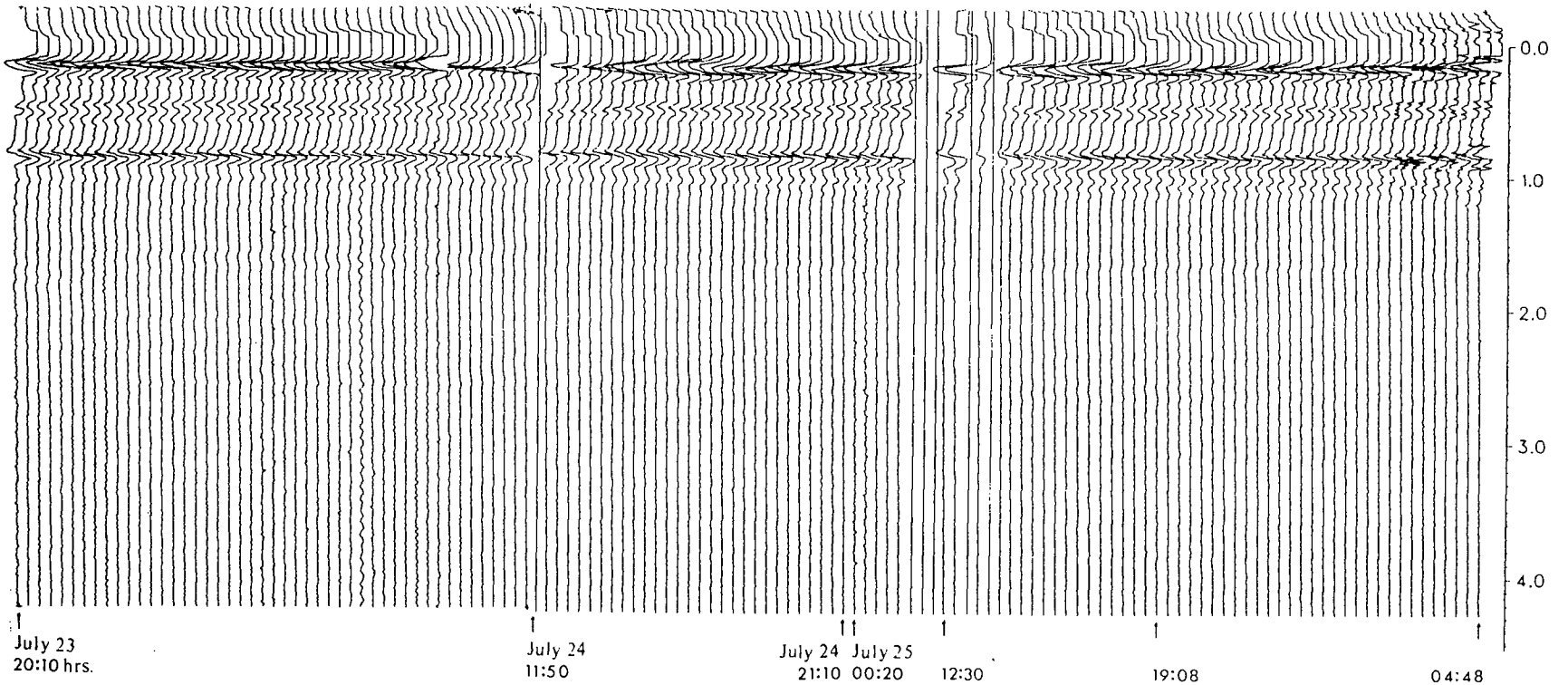

Figure 6.11 Usable records from figure 6.10 with noisy records zeroed and alignment carried out with respect to the leading edge of the bottom echo. Travel-time scale was set using drilling data to obtain depth at this site.

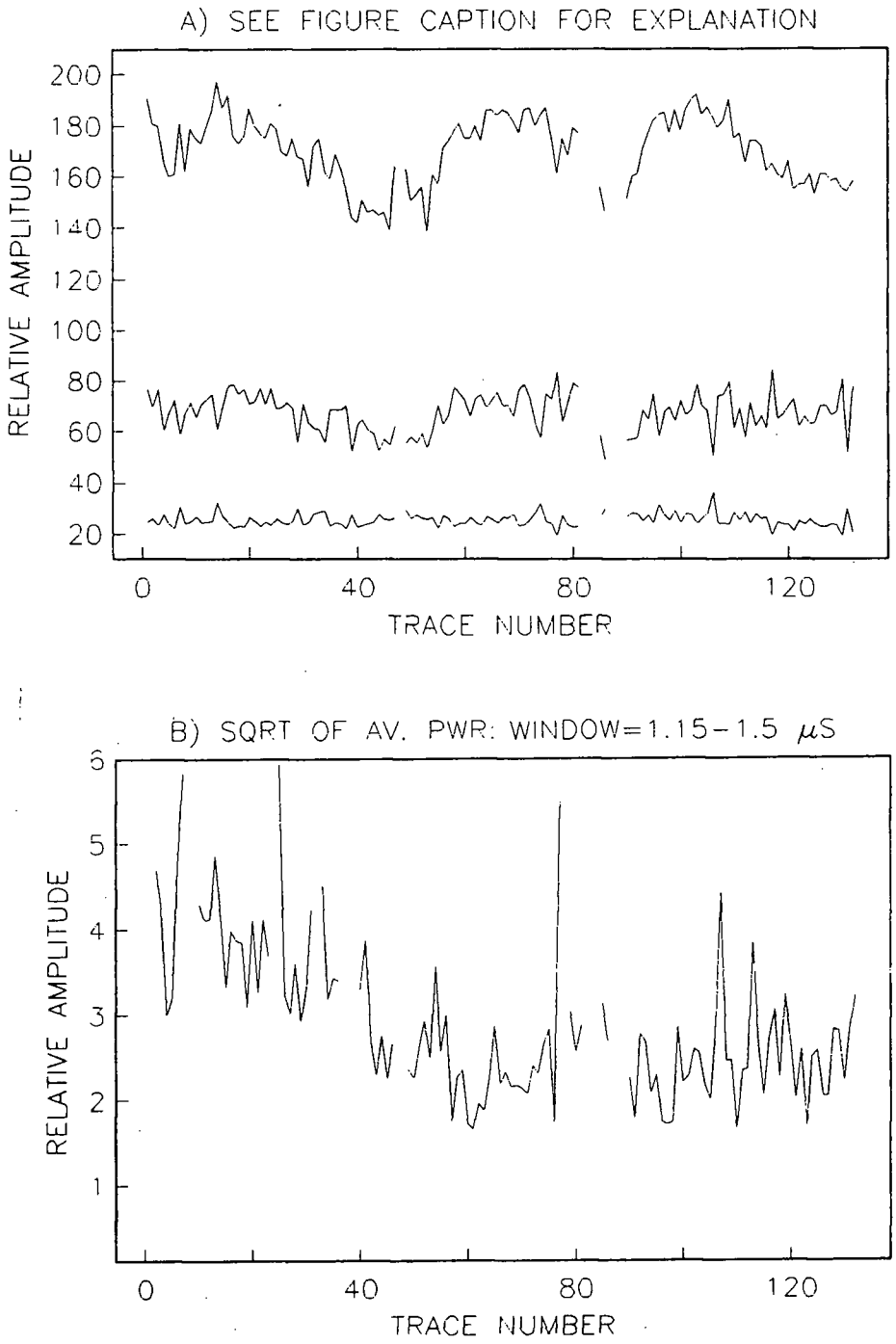

Figure 6.12 Amplitude plots found as per figure 6.9. Note that traces were recorded 20 minutes apart except for discontinuities noted in figure 6.11. (A) Three peak-to-peak amplitude plots. Basal echo amplitude, a_b, is uppermost and englacial echo amplitude, a_e, is in the middle. At the bottom is plotted $(a_b/a_e) \times 10$; multiplication by 10 is for plotting purposes only. (B) Linear trend over the window was removed (see caption of figure 6.9) and average remaining power within the window was found. Square root of the result was taken to improve plot appearance.

to note that a drainage event was recorded in the early morning of July 25, both by a water level pulse at the downstream staging recorder and by an anomalous *increase* in streamwater conductivity (C. Smart, pers. comm.,1986).

Principal component decomposition was used to try enhancing subtle variations in this section. Figure 6.13 shows various types of misfit reconstructions which exhibit the following characteristics. Most large-scale variations (or variations in the more common components) apparently occur in the echo amplitude and in the shape of the pulse following the bottom echo (figures 6.13c, 6.13f, and 6.13g). Small-scale variations are emphasized by reconstruction with lower order principal components, and appear to occur at the leading and trailing edges of the main echo (figures 6.13d, and 6.13e). In most cases, there is little suggestion of variations other than those related to the diurnal changes already discussed. Reconstruction with principal components 3, 4 and 5 (figures 6.13f and 6.13g) have the best potential in this case, showing signal inversions between traces 14 to 24, and 60 to 71. These correspond very well to the periods of falling echo amplitude and probably do not indicate anything more than what can be deduced from the amplitude plots of figure 6.12.

A final observation concerns the unexpected variability of signal character. Traces recorded only 20 minutes apart at the same location were expected to be more similar. Improvements might best be obtained by gathering more records at each location and stacking them. If noise is truly random, then the observed signal-to-noise ratio can be improved by a factor of $\sqrt{n}$ with an n fold stack. With the current system, this would not be difficult, providing that a higher capacity high voltage supply could be obtained for the transmitter, and a faster, more reliable digital storage medium could be obtained to replace the cassettes.

In conclusion, it should be noted that, in spite of being able to draw only tentative glaciological conclusions from this experiment, it is the first known set of data recorded

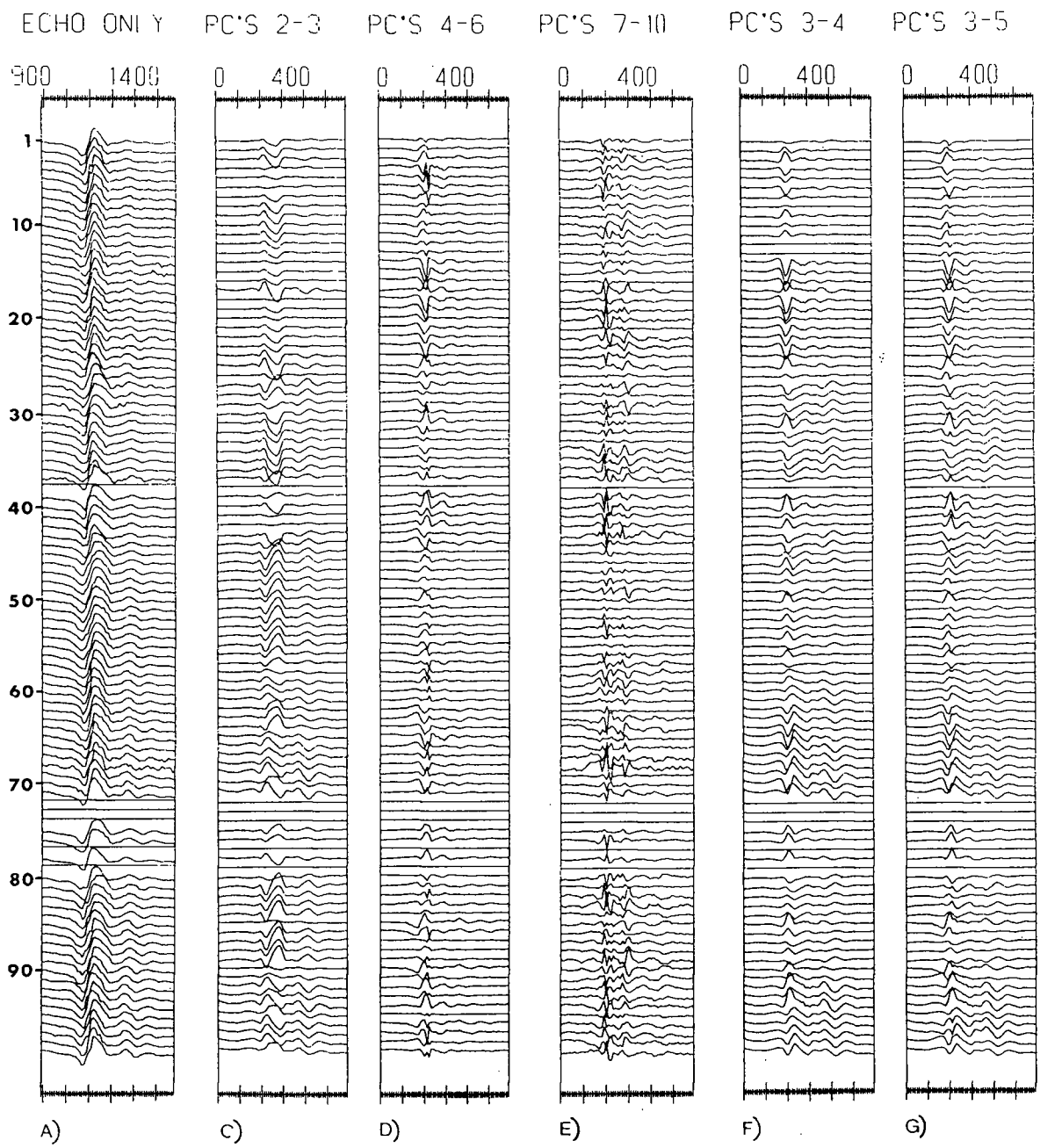

Figure 6.13 Results of reconstruction with principal components derived from traces 11 to 109 of figure 6.11. (A) The raw data; bottom echo only. (B) Mean stack across all 99 traces. (C) to (G) Reconstruction using only those principal components that are noted above each figure.

automatically over an extended time period. Readings taken at 20-minute intervals show distinct diurnal variations assumed to be caused by ambient temperature affecting SCR trigger timing and switching speed. The problems encountered are not insurmountable, and temporal radar data of this type may prove to be useful when taken in conjunction with other glaciological and hydrological data.

CHAPTER VII

SUMMARY

I have addressed theoretical and practical considerations concerning the application of impulse radar echo sounding to the geophysical investigation of glaciers. Theoretical discussion was begun by noting the wide range of values possible for electrical parameters of glacier materials. Table 2.1 summarizes these, and table 2.2 gives representative reflection coefficients for several possible reflectors of electromagnetic waves. Evidently, it should be possible to determine the type of glacier bed from the echoes, but in practice, exact reflectivities are not easily obtained. The modelling experiments discussed in chapter 3 suggest that finer structure of the glacier bed may be resolvable, but again, only large variations in physical features are likely to be noticeble in changes of echo character. Application of digital signal processing techniques such as the Karhunen-Loève transform may help separate the finer structure from large-scale signal features, but some care is required in applying and interpreting such methods.

The UBC impulse radar instrument was found to operate satisfactorily, given that it is a prototype. The major requirement is for a triggerable transmitter that is stable and temperature-compensated. An alternative and perhaps more practical solution to the timing problem would be to generate a signal at the transmitter to inform the receiver of the exact time of pulse emission. A further important hardware modification would replace the cassette with a more robust memory, perhaps solid-state random access memory. Also, portable computers are being considered for control and data manipulation in the field. The automatic data collecting facility has great potential for temporal studies

of glacier dynamics, and if the current system can be speeded up, will also help make depth profiling more efficient.

Interpretation of impulse radar data is greatly facilitated by including reference signals in the records. Quantitative analysis tends to be unreliable without having some known response with which to compare interesting signals. Future work may involve the use of fixed radar reflectors in the air or perhaps down crevasses, to be used as timing and amplitude references. The field work presented also emphasizes the difficulties of interpreting sparse data. This is a common problem throughout geophysics, and until the advent of lightweight digital technology, particularly evident in radio echo sounding of small glaciers. Instruments such as the one described in this thesis, especially if they can gather reliable data at high rates, will certainly help alleviate this problem.

Signals that have interacted with the ice/air interface were shown to be difficult to use. Neverthless, I employed echoes from a crevasse to help conclude that bottom echo amplitudes suggest a wet, porous glacier bed. Some anomalous features were discussed, but not adequately explained. Subglacial cavities capable of draining drill holes were perhaps observed, but this is still only speculative. Future work with the UBC impulse radar will involve gathering concurrent geophysical and hydrological data for comparative studies of these and other features.

Finally, it should be noted that the high quality of the 1986 data is partly due to successful operation of the equipment, but that local conditions were also an important factor. Trapridge Glacier is not only shallow (less than 100 m in the area investigated) but its temperature is below freezing throughout, minimizing attenuation of the radar pulses. Warmer, deeper glaciers must be sounded to evaluate the current system's performance on temperate glaciers.

REFERENCES

Abramowitz, M. and Stegun, I.A. (Eds.) 1972, *Handbook of Mathematical Functions*, Published by Dover publications, Inc.

Anderson, D.M., Pusch, R. and Penner, E. 1978, Physical and Thermal Properties of Frozen Ground, in *Geotechnical Engineering for Cold Regions*, Eds.: O.B.Andersland and D.M.Anderson, McGraw-Hill Book Company, U.S.A., 570p.

Annan, A. P. 1973, *Radio Interferometry Depth Sounding: Part 1 - Theoretical Discussion*, Geophysics, **38, no.3**, p.557-579.

Anann, A.P. and Davis, J.L. 1976, *Impulse Radar Sounding in Permafrost*, Radio Science **11, No.4**, p.383.

Arcone, S.A. 1981, *Distortion of Model Subsurface Radar Pulses in Complex Dielectrics*, Radio Science, **16, No.5**, p.855.

Arcone, S.A. and Delaney, A.J. 1982, *Dielectric Properties of Thawed Active Layers Overlying Permafrost Using Radar at VHF* Radio Science **17, No.3**, p.618.

Arcone, S.A. and Delaney, A.J. 1984, *Radar Investigations Above the Trans-Alaska Pipeline Near Fairbanks*, U.S. Cold Regions Research and Engineering Laboratory, CRREL Report **84-27**.

Berry, M.V. 1975, *Theory of Radio Echoes From Glacier Beds*, Journal of Glaciology, **15, No.73**, 65-74.

Bogorodsky, V.V. Bentley, C.R. and Gudmandsen, P.E. 1986, *Radioglaciology*, D. Reidel Publishing Company, Dordrecht, Holland, 254p.

Clarke, G.K.C. Collins, S.G. and Thompson, D.E. 1984, *Flow, Thermal Structure, and Subglacial Conditions of a Surge-Type Glacier*, Can. J. Earth Sci. **21, No.2**, 232-240.

Clarke, G.K.C. Meldrum, R.D. and Collins, S.G. 1986, *Measuring Glacier Fluctuations Using a Computer-Controlled Survey System*, Can. J. Earth Sci. **23, No.5**, 727-733.

Collins, D.N. 1981, *Seasonal Variations of Solute Concentration in Melt Waters Draining From an Alpine Glacier*, Annals of Glaciology **2**, 11-16.

Cook, J.C. 1960, *Proposed Mono-cycle Very-high-frequency Radar for Air-born Snow and Ice Measurement*, Transactactions of the American Institute of Electrical Engineers. **Pt.1, Vol.79** 588-594.

Cook, J.C. 1974, *Status of Ground-Probing Radar and Some Recent Experience*, Proceedings of Engineering Foundation Conference on Subsurface Exploration for Underground Excavation and Heavy Construction, Aug. 11-16 1974, Henniker New Hampshire. New York: American Society of Civil Engineers, p. 213.

Davis, J.L. 1975, *Relative Permittivity Measurements of a Sand and Clay Soil in Situ*, Geol. Surv. Can. paper **75-1C**, p.361

Davis, J.L. Topp, T.P. and Annan, A.P. 1976, *Electromagnetic Detection of Soil Water Content*; Progress Report 2, for Workshop on Remote Sensing of Soil Moisture and Ground Water, Toronto, Ontario, Nov. 1976.

Drewry, D. 1986, *Glacial Geologic Processes*, Edward Arnold (Publishers) Ltd. London, U.K. 276p.

Evans, S. 1965, *Dielectric Properties of Snow and Ice - A Review* Journal of Glaciology, **5, No.42**, 773-792.

Fagan, M. 1987, *Radar Sizes up Arctic Ice*, New Scientist, 12 February 1987 **No.1547**, p.35.

Glen, J.W. and Paren, J.G. 1975, *The Electrical Properties of Snow and Ice*, Journal of Glaciology, **15, No.73** 15-38.

Gutzwiller, F.W. (Editor), 1967, *SCR Manual (fourth edition)*, Published by Semiconductor Products Departement, General Electric Company.

Harrison, C.H. 1970, *Reconstruction of Subglacial Relief from Radio Echo Sounding Records*, Geophysics, **35, No.6**, 1099-1115.

Hoekstra, P. and Delaney, A.J. 1974, *Dielectric Properties of Soils at UHF and Microwave Frequencies*, Journal of Geophysical Research, **79, No.11**, 1699-1708.

Jacobel, R. and Raymond, C. 1984, *Radio Echo Sounding Studies of Englacial Water Movement in Variegated Glacier, Alaska*, Journal of Glaciology, **30, No.104**, 22-29.

Jezek, K.C. and Thompson, L.G. 1982, *Interpretation of Mono-Pulse Ice Radar Soundings on Two Peruvian Glaciers*, IEEE Trans. on Geoscience and Remote Sensing, **GE-20, No. 3**, p.243-249.

Jones, I.F. 1985, *Appliation of the Karhunen-Loève Transform in Reflection Seismology*, Unpub. PhD. Thesis, University of British Columbia.

Jordan, E.C. and Balmain, K.G. 1968, *Electromagnetic Waves and Radiating Systems*, Prentice-Hall Inc. Englewood Cliffs, New Jersey, 753p.

Kanda, M. 1980, *Transients in a Resistively Loaded Antenna Compared with Those in a Conical Antenna and a Horn*, IEEE Trans. on Antennas and Propagation, **AP-28, No.1**, 132-136.

Kanasewich, E.R. 1981, *Time Sequence Analysis in Geophysics*, The University of Alberta Press, Edmonton, Canada, 480p.

Keller, G.V. 1967, *Applications of Resistivity Methods in Mining and Groundwater Exploration Programs*, In Mining and Groundwater Geophysics, 1967, Proceedings of the Canadian Centennial Conference on Mining and Groundwater Geophysics, Niagara Falls, Canada, 1967, Ed. L.W.Morey.

Maxwell, M. 1986, *Basal Processes in Surging Glaciers*, Unpub. PhD. Thesis, University of British Columbia.

Morey, R.M. 1974, *Continuous Subsurface Profiling by Impulse Radar*, Proceedings of Engineering Foundation Conference on Subsurface Exploration for Underground Excavation and Heavy Construction, Aug. 11-16 1974, Henniker New Hampshire. New York: American Society of Civil Engineers, p. 213.

Morey, R.M. and Kovacs, A. 1985, *Analysis of Wide-Angle Reflecton and Refraction Measurements*, U.S. Cold Regions Research and Engineering Laboratory, CRREL Special Report **85-5**, Workshop on Permafrost Geophysics, Golden, Colorado, 23-24 Oct 1984, Editors: J.Brown, M.C.Metz, P.Hoekstra.

Narod, B.B. and Clarke, G.K.C. 1983, *UHF Radar System for Airborne Surveys of Ice Thickness*, Can. J. Earth Sci. **20, No.7**, 1073-1086.

Narod, B.B. and Yedlin, M.J. 1986, *A Basic Acoustic Diffraction Experiment For Demonstrating the Geometrical Theory of Diffraction*, Am. J. Phys. **54, No.12**, 1121-1126.

Olhoeft, G.R. 1978a, *Electrical Properties of Permafrost*, Proceedings of the Third International Conference on Permafrost, July 10-13, 1978, Edmonton, Alberta, Canada, Vol. 1, p.128.

Oswald, G.K.A. 1975, *Investigation of Sub-ice Bedrock Characteristics by Radio-Echo Sounding*, Journal of Glaciology, **15, No.73**, 75-88.

Paren, J.G. 1970, *Dielectric Properties of Ice*, Unpub. PhD. Thesis, University of Cambridge.

Post, A. and LaChapelle, E.R. 1971, *Glacier Ice*, University of Toronto Press, Toronto, Canada, 178p.

Prager, B.T. 1983, *Digital Signal Processing of UHF. Radio-echo Sounding Data from Northern Ellesmere Island*, Unpub. MSc. Thesis, University of British Columbia, 88 pages.

RCA Corporation. 1977, *User Manual for the CDP1802 COSMAC Microprocessor.* RCA Solid State, USA.

Robin, G. deQ. Evans, S. and Bailey, J.T. 1969, *Interpretation of Radio-echo Sounding in Polar Ice Sheets*, Philosophical Transactions of the Royal Society, Series A, **265**, 437-505.

Rose, G.C. and Vickers, R.S. 1974, *Calculated and Experimental Response of Resistively Loaded V Antennas to Impulsive Exitation*, Int. J. Electronics, **37** 261-271.

St. Amant, M. and Strangway, D.W. 1970, *Dielectric Properties of Dry, Geologic Materials*, Geophysics **35, No. 4**, 624-645

Sellman, P.V. Arcone, S.A. and Delaney, A.J. 1983, *Radar Profiling of Buried Reflectors and the Groundwater Table*, U.S. Cold Regions Research and Engineering Laboratory, CRREL Report **83-11**.

Shen, L.C. and King, R.W.P. 1965, *Correction to the Cylindrical Antenna with Nonreflecting Resistive Loading by Wu and King*, IEEE Trans. on Antennas and Propagation, **AP-13, No.6**, p.998.

Sheriff, R.E. and Geldart, L.P. 1982, *Exploration Seismology, Vol.1; History, Theory and Data Aquisition*, Cambridge University Press, Cambridge, U.K. 253p.

Smith, B.M. 1971, *Radio Echo Studies of Glaciers*, Unpub. PhD. Thesis, University of Cambridge

Smith, B.M. and Evans, S. 1972, *Radio Echo Sounding: Absorption and Scattering by Water Inclusions and Ice Lenses*, Journal of Glaciology, **11, No.61** 133-146.

Sverisson, M. Johannesson, Æ. and Bjornsson, H. 1980, *Radio-echo Equipment for Depth Sounding of Temperate Glaciers*, . Journal of Glaciology, **25, No.93**, 477-486.

Ulriksen, C.P.F. 1982, *Application of Impulse Radar to Civil Engineering*, Unpub. PhD Thesis, Lund University of Technology

Walford, M.E.R. and Harper, M.F.L. 1981, *The Detailed Study of Glacier Beds Using Radio Echo Sounding Techniques*, Geophys. J. R. Astr. Soc. **67** 485-514.

Walford, M.E.R. Kennett, M.J. and Holmlund, P. 1986, *Interpretation of Radio Echoes From Storglaciären, Northern Sweden*, Journal of Glaciology, **32, No.110**, 39-49.

Watts, R.D. and England, A.E. 1976, *Radio-echo Sounding of Temperate Glaciers: Ice Properties and Sounder Design Criteria*, Journal of Glaciology, **17, No.75**, 39-48.

Watts, R.D. and Wright, D.L. 1981, *Systems for Measuring Thickness of Temperate and Polar Ice from the Ground or from the Air*, Journal of Glaciology, **27, No.97**, p.459-469.

Wong, J. Rossiter, J.R. Olhoeft, G.R. and Strangway, D.W. 1977, *Permafrost: Electrical Properties of the Active Layer Measured in situ*, Can. J. Earth Sci. **14**, p.582.

Wu, T.T. and King, R.W.P. 1965, *The Cylindrical Antenna With Nonreflecting Resistive Loading* IEEE Trans. on Antennas and Propagation, **AP-13, No.3**, 369-373.

APPENDIX 1: Instrument Specifications

System

Depth precision	0.82 m
Maximum depth	841 m
Data storage	1320 bytes per record
	52 records per cassette
Time to gather one record	4 s
Time to store one record	40 s
Automatic data collection	Programmable — 1 to 255 min intervals
Weights (no batteries)	receiver unit — 5.1 kg
	transmitter — 0.4 kg
	antennas — 1.2 kg each

Transmitter

Peak pulse output	1200 V into antenna
Pulse rise time	40 ns from 37% to 100% of V_{max}
Pulse recovery	time constant is approximately 30 μs
Repetition rate	250 Hz
Internal triggering delay	0.8 μs at 24°C
Power requirments	idling — 95 ma at 18 V
	pulsing at 250 Hz — 280 ma at 18 V

Antennas

Type	Broadband (resistively damped) halfwave dipole
Dipole arm length	h = 5 m
Centre frequency	8.4 MHz in ice
	15 MHz in air
Damping coefficient	$R_0 = 300\,\Omega$

Construction: Wire and carbon resistors are installed inside 1 m sections of plastic pipe. Sections can be screwed together to form antennas with required centre frequency and damping characteristics.

Receiver Unit

Input impedance	3.6 kΩ
Total voltage gain	150
Attenuator	divide by factors of 1, 2, 4, 20 or 100
Sensitivity at maximum gain	LSB = 0.26 mV at rcvr. antenna
Amplitude resolution	8 bits
Bandwidth	46 MHz
Number of samples per record	1024
Sampling interval	9.76 ns
CPU	RCA CDP1802
Memory	4 kbyte of ROM
	1.25 kbyte of RAM
Clock speed	2.0 MHz
Inputs and outputs	hex keypad
	8 digit LED display
	oscilloscope driver
	RS-232C serial interface
	digital read/write cassette
Power requirements	Min. (system idling) — 450 ma at 18 V
	Max. (momentary) — 1800 ma at 18 V
	Gathering data — 960 ma at 18 V

Note: All digital circuits use CMOS technology.

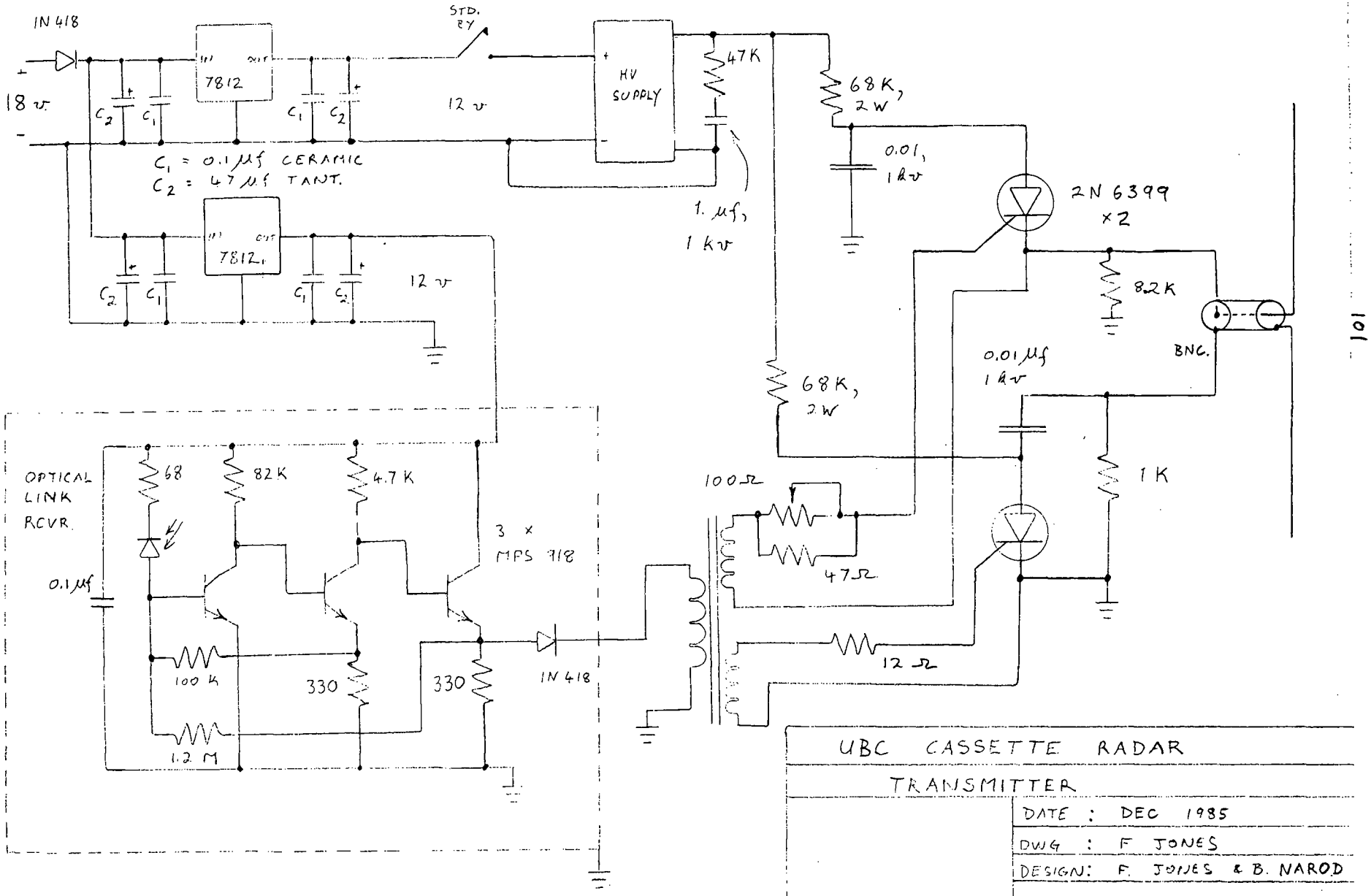

UBC CASSETTE RADAR

TRANSMITTER

DATE : DEC 1985

DWG : F JONES

DESIGN: F. JONES & B. NAROD

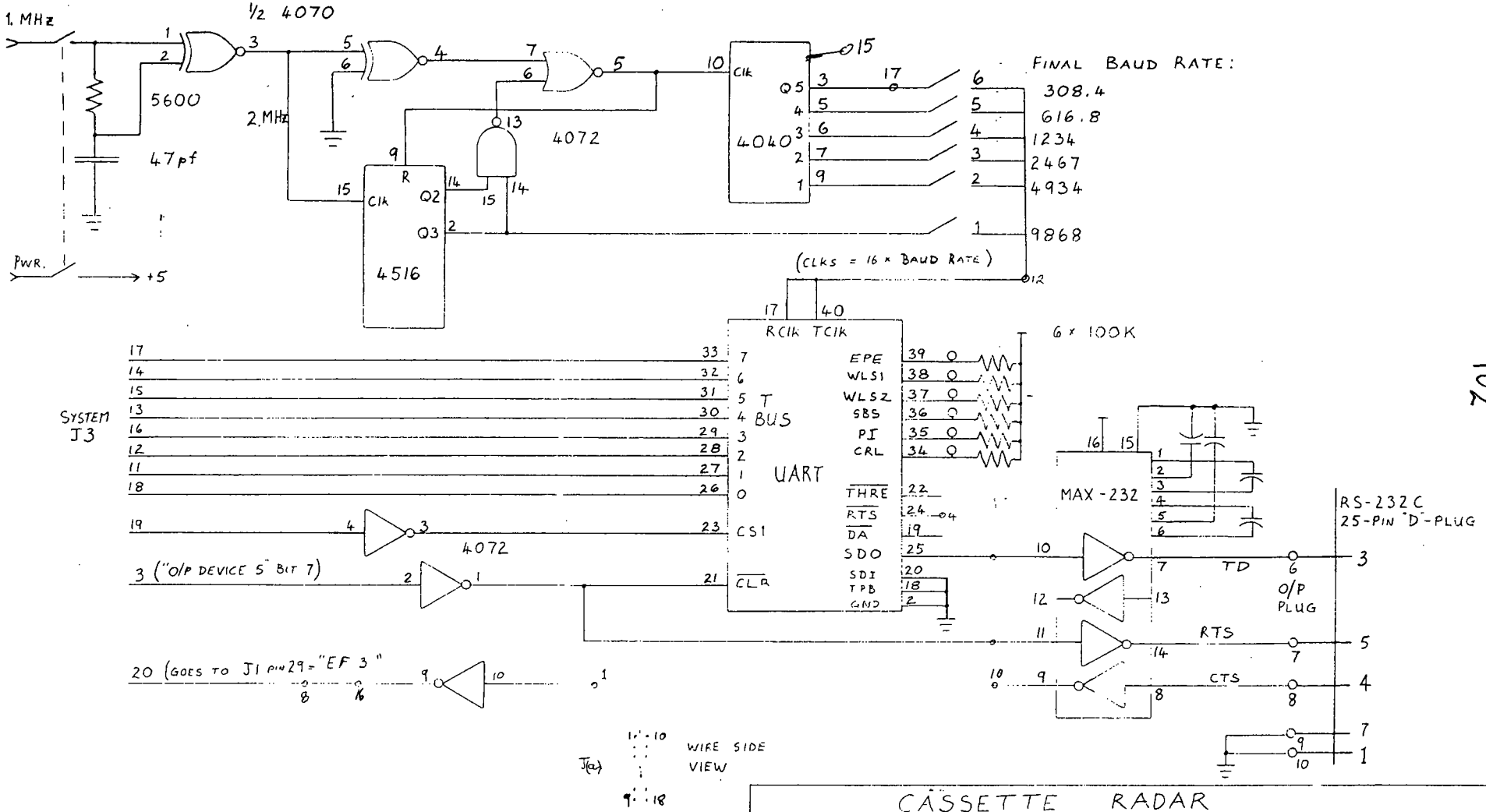

CASSETTE RADAR

UART : CDP 1854

* NOT CHECKED → 7-5-87

RS-232C INTERFACE

DRAWN: F. JONES (7-5-87)

DATE: APRIL 1986

DESIGN: F. JONES

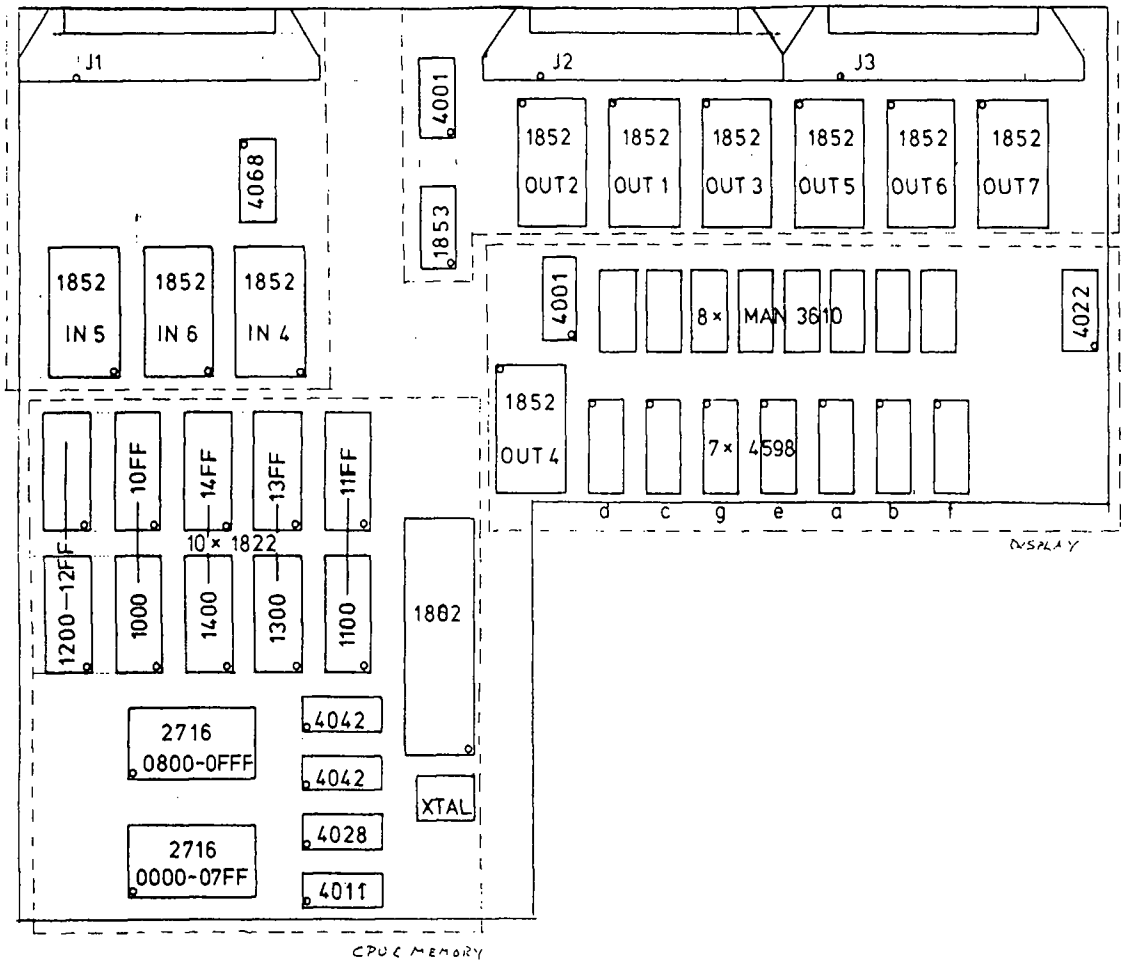

CASSETTE RADAR

CASSETTE LOGGER MAIN BOARD

ASSEMBLY DIAGRAM

DATE: APRIL 10, 1980

DRAWN BY: B. HARDS

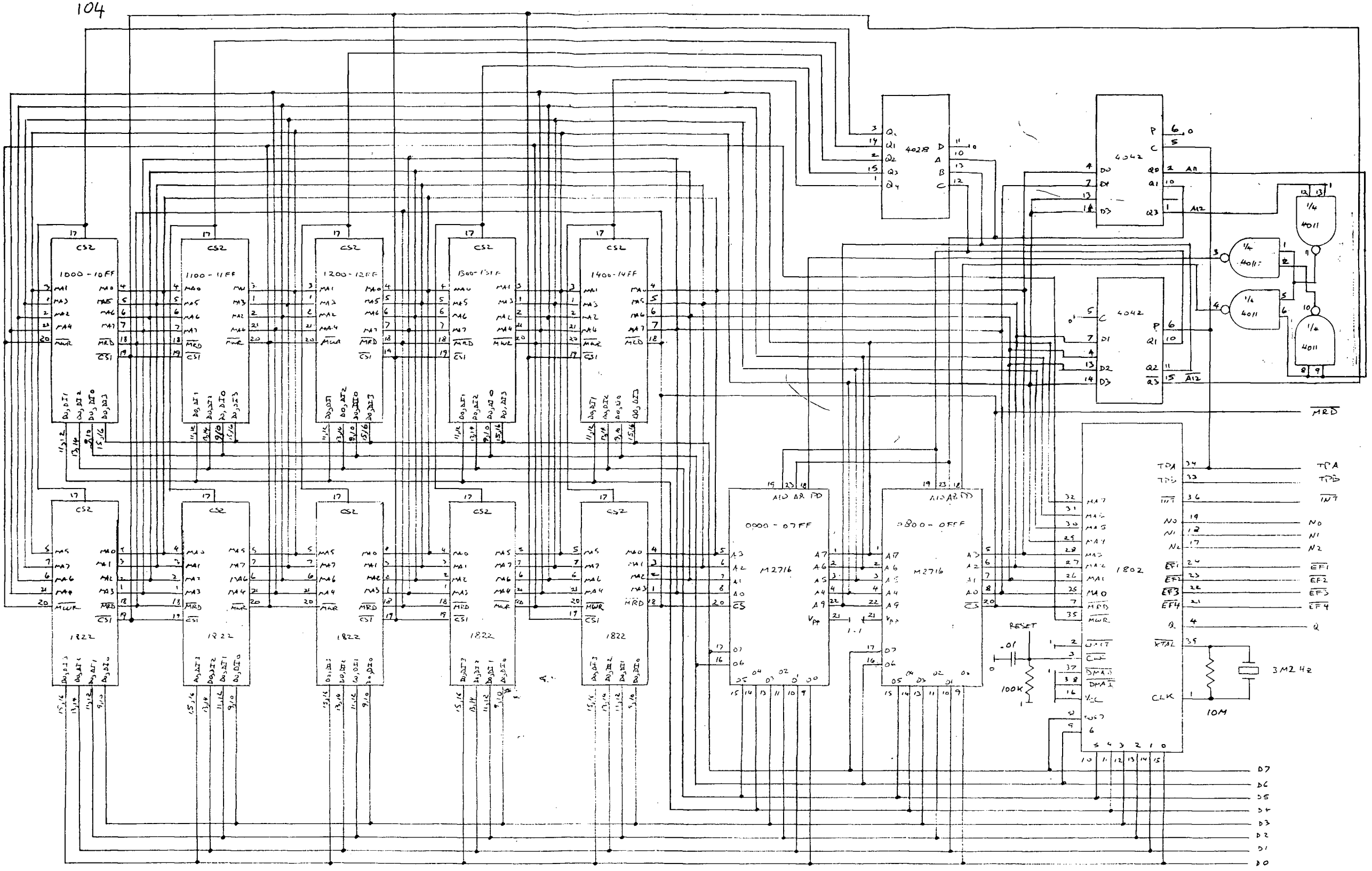

CASSETTE RADAR

SHEET 1 OF 4	(COMPUTER)
SCHEMATIC -	CPU & MEMORY
DRAWN BY:	B. NAROD
DATE	NOV. 23, '79
DESIGNED BY:	B. NAROD

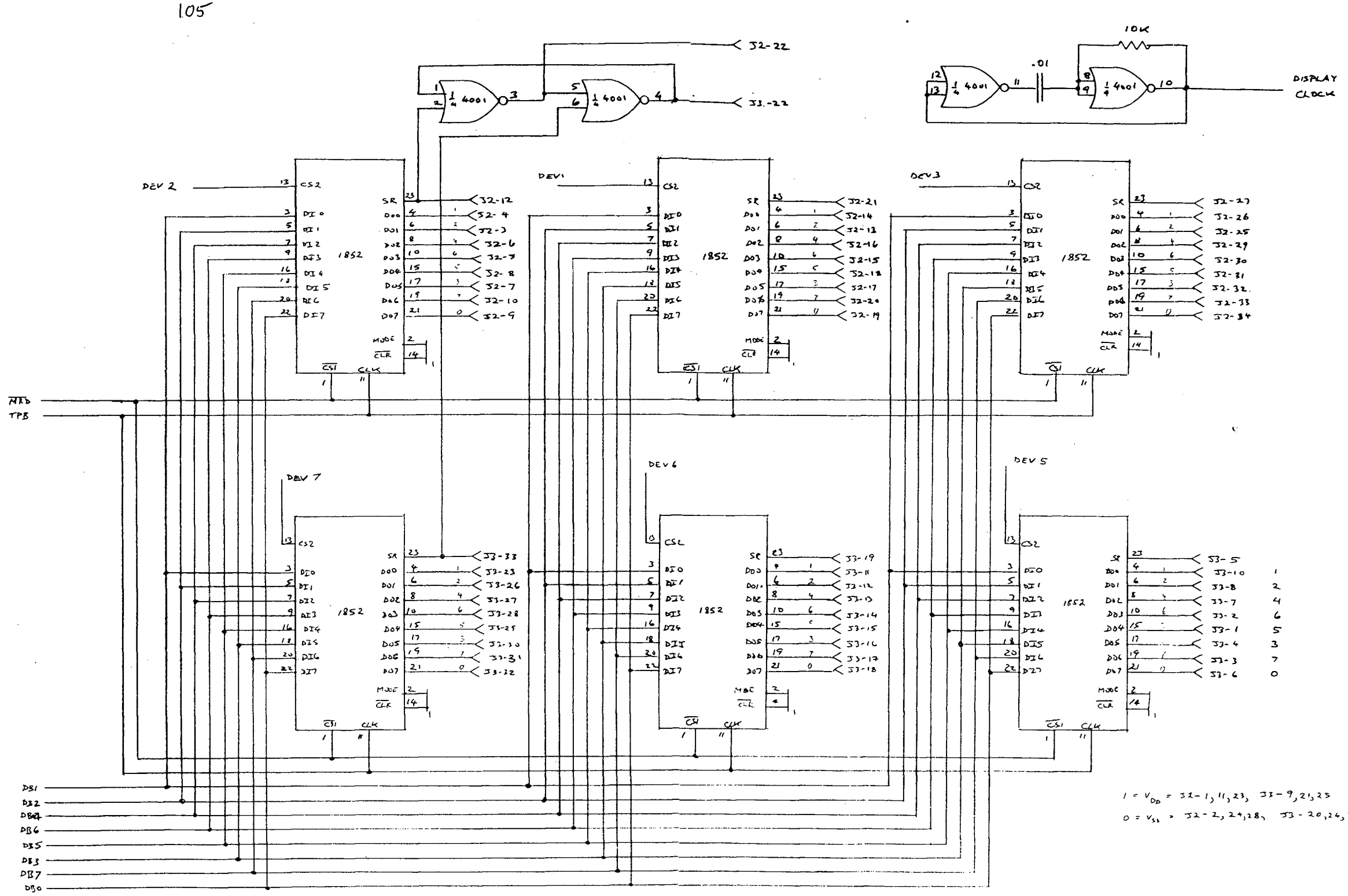

1 = V_{DD} = J2-1, 11, 23, J3-9, 21, 23

0 = V_{SS} = J2-2, 24, 28, J3-20, 24, 34

CASSETTE RADAR

SHEET 2 OF 4 (COMPUTER)	
SCHEMATIC - OUTPUT PORTS	
DRAWN BY:	B. NAROD
DATE:	NOV. 1979
DESIGN:	B. NAROD

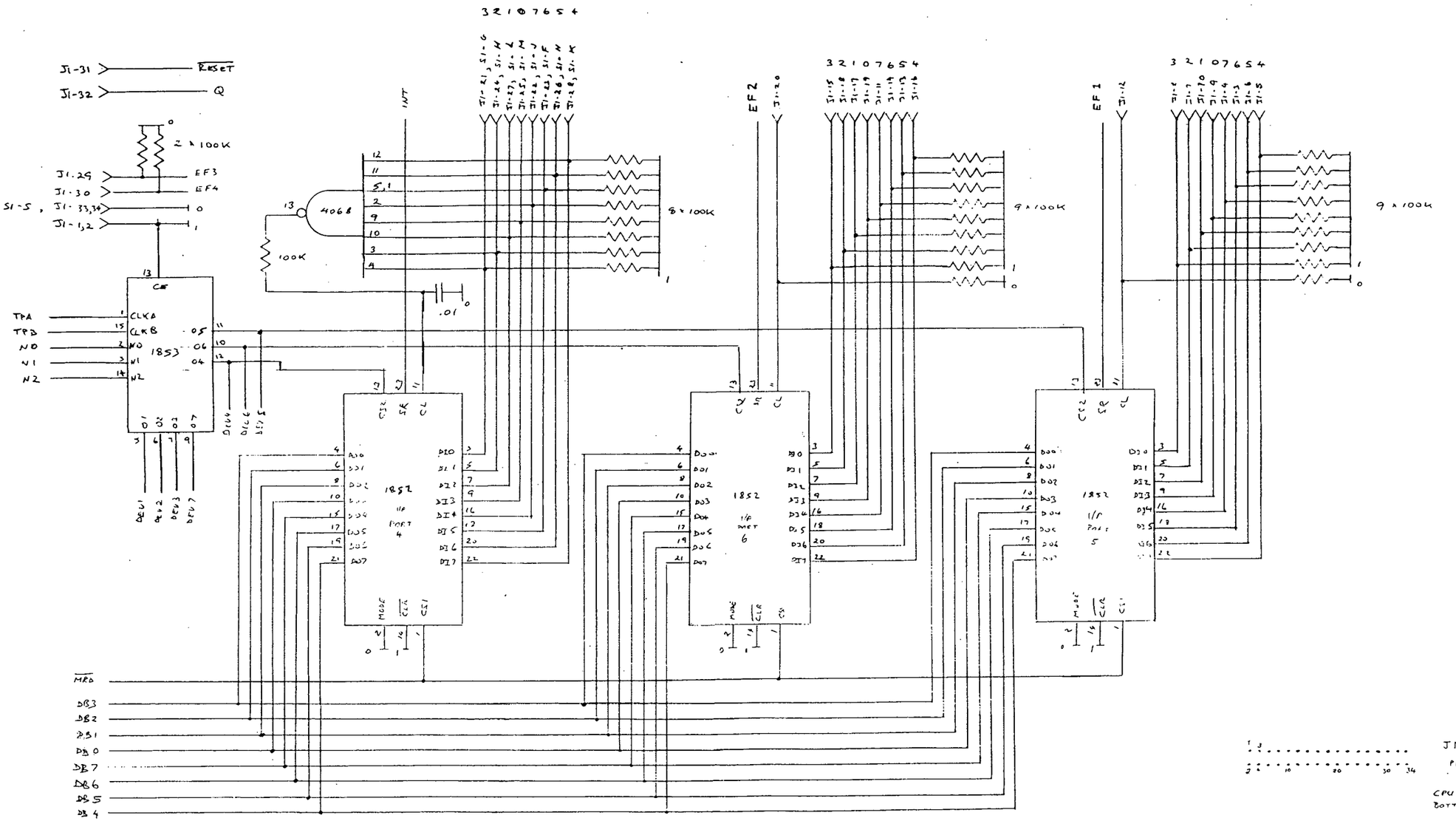

CASSETTE RADAR

	SHEET 3 of 4 (COMPUTER)
	SCHEMATIC – INPUT PORTS
	DRAWN: B. NAROD
	DATE: NOV. 1979
	DESIGN: B. NAROD

1067

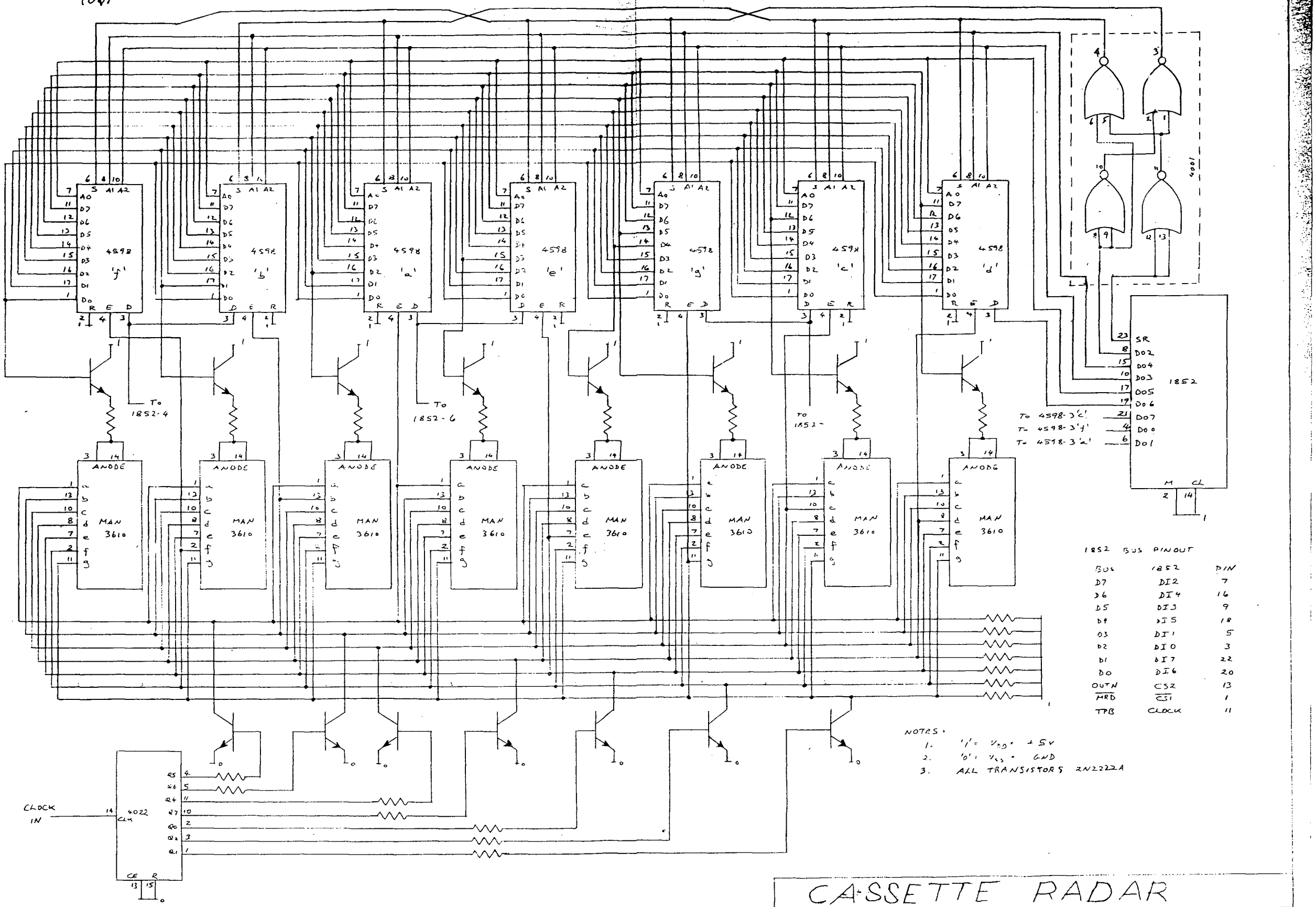

1852 BUS PINOUT

BUS	1852	PIN
D7	DI2	7
D6	DI4	16
D5	DI3	9
D4	DI5	18
D3	DI1	5
D2	DI0	3
D1	DI7	22
D0	DI6	20
OUTN	CS2	13
$\overline{MRD}$	$\overline{CS1}$	1
TPB	CLOCK	11

NOTES:
1. '1' = V_{DD} = +5V
2. '0' = V_{SS} = GND
3. ALL TRANSISTORS 2N2222A

CASSETTE RADAR

SHEET 4 OF 4 (COMPUTER)

SCHEMATIC - LED DRIVE

DRAWN BY: B. NAROD

DATE: NOV 23 79

DESIGNED BY: B. NAROD

1MHz
10 MΩ
10 pf
4069
÷4
÷10
÷10
AND 4081
4018B
4018A
4518
Q1
Q2
Q3
3 × IN914
MR-1000-15
3300 pf
POLYSTYRENE
OP 01
4050
T2
5K
T3
100K
+15
-15
68K
T1
20K
100 pf
4.7 K
4013C
FAST RAMP
CMP01
4001
SLOW RAMP
IN914
200K
T6
330 pf
NOR - 4001
15Ω
J4
2N4124
J3 pin 4
PORT 5 bit 3
4013
4069C
RS-232C
100K
J4-10
(CALIB. SIG.)
4013 B
J3 pin 1
PORT 5 bit 5
4040
4069
DAC -03
REF OUT
REF IN
SIGN
dP
T7 100K
0.1
74LS 122
1K
100 pf
S/H
J4-16
To PREAMP CARD
270 pf
6.8 K
4013 A
CONVERT

J1 - 33, 34
J2 - 2, 24, 28
J3 - 20, 24, 34

J2-21
J1-20
J1-12

CONVERT
4011A
4011
4013A
J1-30
"EF4"
47 µf
0.1 µf
2.2 µf
NA
STS
R/C
AD-41334
(AD574-ASE)
from the version of
AD574
MSB
LSB
CE
In
ref in
ref out
Bip out
2 - 50Ω 1.0%
A0
12/8
CS
J1
47 µf
0.1 µf
-15

J4-12
ANALOGUE IN FROM PRE-AMP

CASSETTE RADAR

NOTES: 1) ÷4 & ÷10 YEILDS 250 Hz TRIG. RATE.

SHEET 1 of 3 (RCVR - SAMPLER)
SCHEMATIC: SAMPLING TIME BASE
DRAWN BY: F. JONES
DATE: AUG 1985
DESIGN: B. NABOD & F. JONES

1089

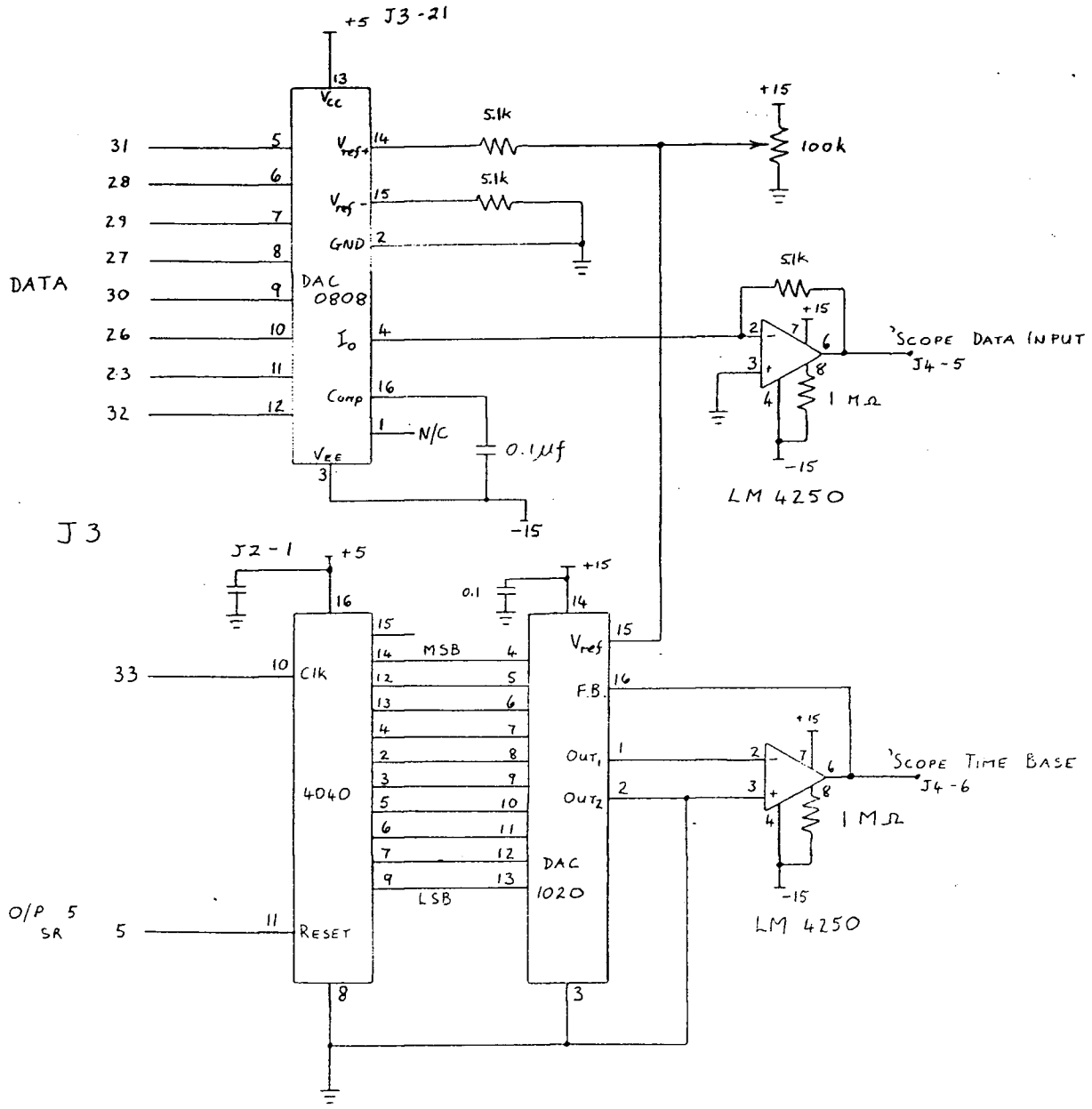

DISPLAY 'SCOPE DRIVER

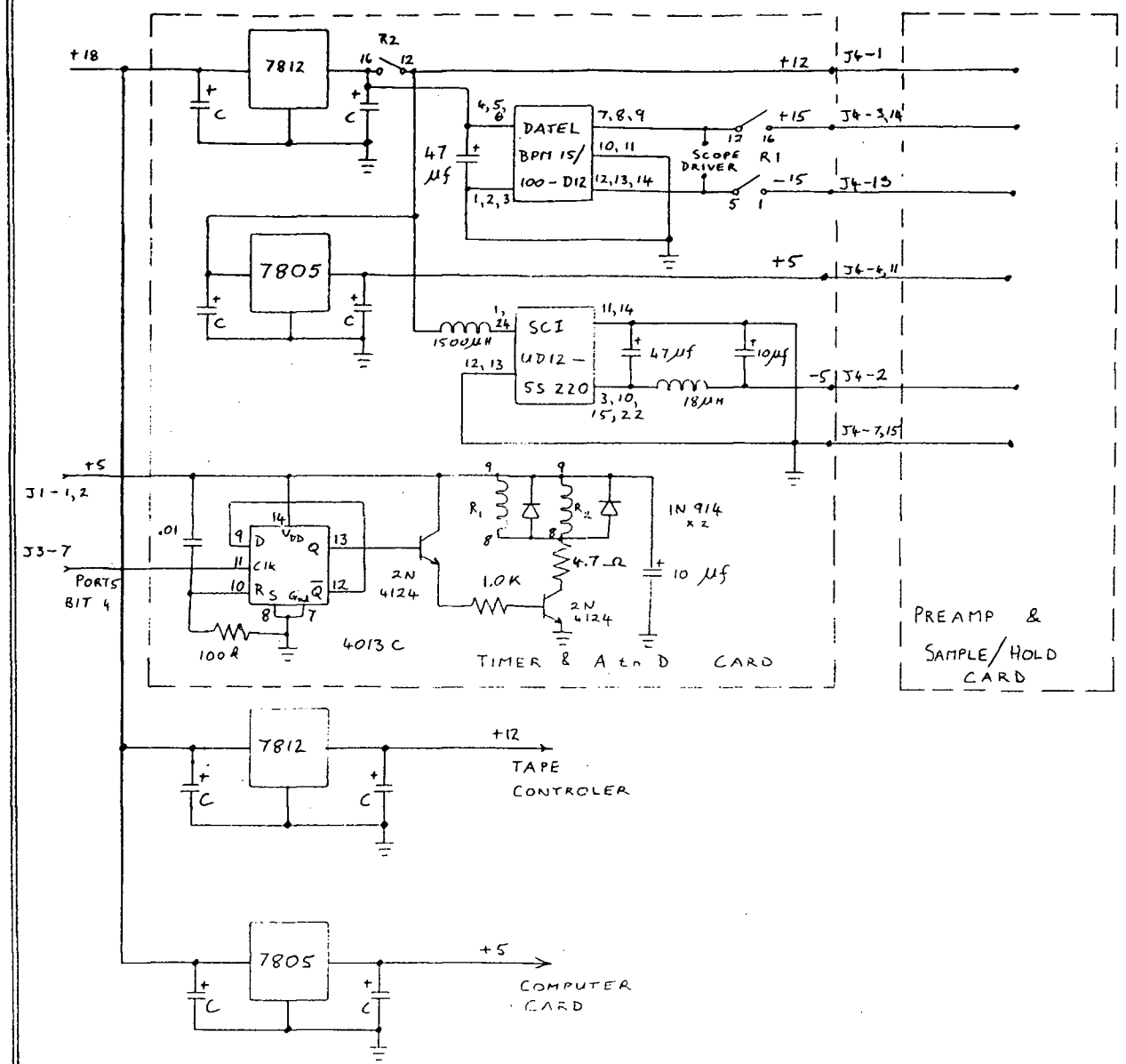

ALL CAPACITORS "C" ARE 0.1 DISK CERAMIC PARALLEL WITH 47 µf TANTALUM

POWER DISTRIBUTION

CASSETTE RADAR

SHEET 2 of 3 (RCVR - SAMPLER)
SCHEMATIC: PSU & DISPLAY
DRAWN BY; F. JONES
DATE; SEPT 1985
DESIGN; F. JONES

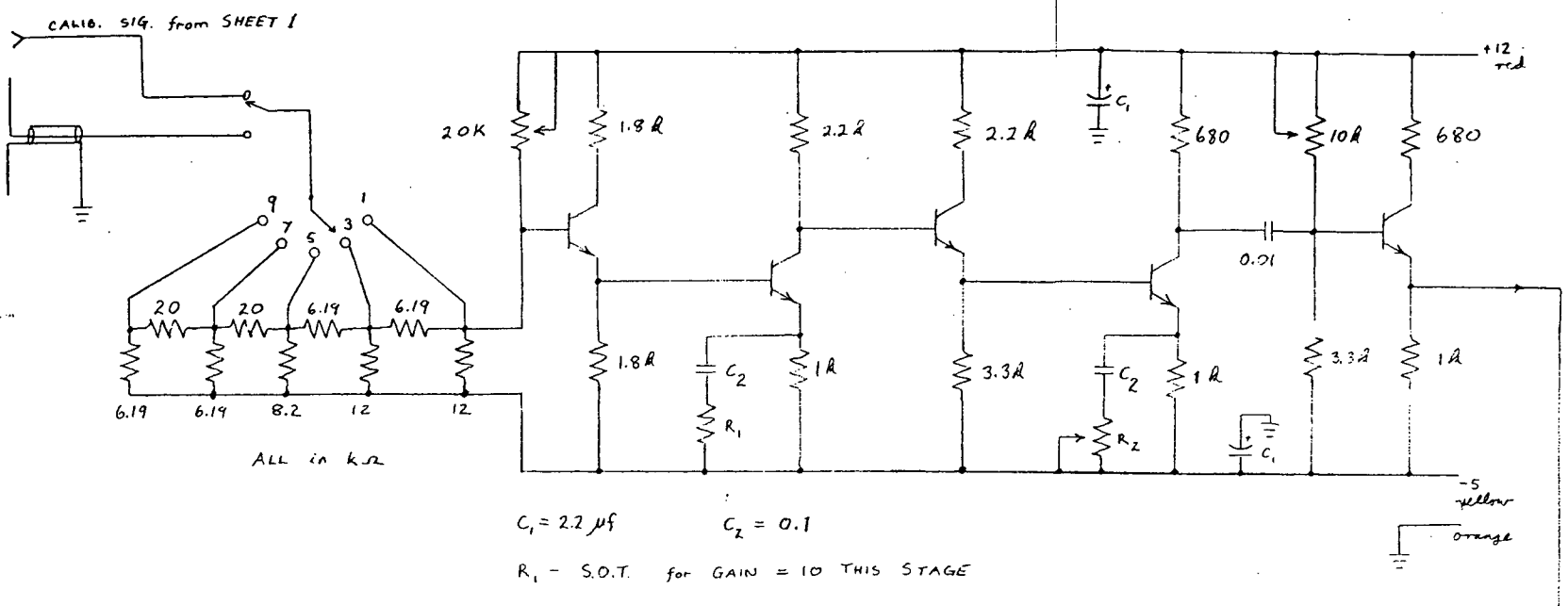

C_1 = 2.2 μf C_2 = 0.1

R_1 - S.O.T. for GAIN = 10 THIS STAGE

R_2 - 1K TRIM ; OVERALL GAIN ADJ. 10 to 100

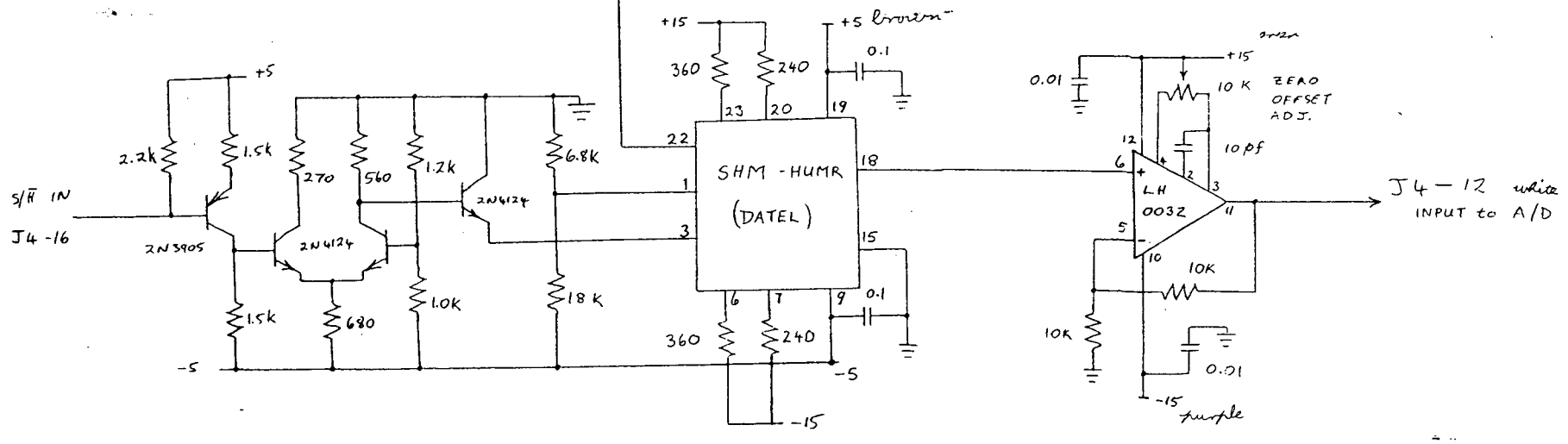

CASSETTE RADAR

SHEET	3 of 3 (RCVR - SAMPLER)
SCHEMATIC:	RECEIVER & SAMPLE/HOLD
DRAWN:	F. JONES
DATE:	SEPT 1985
DESIGN:	F. JONES